METHANE AND CARBON DIOXIDE EXCHANGE PRODUCTION STUDIES FROM EXPOSED NATURAL GAS HYDRATE

Master of Science Thesis in Process Technology

By

Alusine Jalloh

Department of Physics and Technology

University of Bergen, Norway

2010

Abstract

Two laboratory experimental setups have been designed in collaboration with the Reservoir Physics Group at the Department of Physics and Technology. The equipments have been completed and tested. The first experiment was conducted using the four electrode resistivity measurement method on porous media. The equipment has been used to study the influence of resistance with core samples saturated with salinity concentration at 1 kHz, 1200 psig pressure and temperatures down to 3^{o}C during stages of hydrate formation. The experiment was conducted to measure the resistance in Bentheim sandstones in order to correlate resistivity in porous media as function of different filling (gas, aqueous mixture, hydrate). The results showed that resistivity decreases before hydrate formation and then increased to a higher value after hydrate formation. The resistivity increment was observed when the system was cooled down for hydrate formation. The temperature was also observed to decrease with lower conductivity of the brine water in the pores. Finally, the resistivity of the system was higher than corresponding value before hydrate formation when free gas was present. The reason for this was interpreted to be that solid hydrates are filling the pores of the matrix formed by sand grains and change their cementation condition. This is expected to have a great impact on the resistivity of the sample.

The production of CH_4 from its hydrates in porous media during CO_2 sequestration was investigated in a second experiment. The results showed that when CH_4 hydrate was exposed to CO_2 an exchange of gas molecules occurred spontaneously. The reason for this is that, CO2-hydrate is the thermodynamically favored hydrate in terms of free energy under the conditions of temperature and pressure used in these experiments. In view of the huge amounts of hydrate worldwide there is a corresponding great potential of these CH_4 hydrates to store CO_2 on long terms while at the releasing natural gas. This win win situation for environment and energy supply makes this process attractive.

To complement the experimental work, Phase Field Theory models have been used to study the dynamics of CH_4 exchange in CH_4 hydrate with liquid CO_2 at temperatures 273.15 – 284.17K and pressures in the range from 100 - 113.24 bars. The results from the quantitative analysis showed CH_4 in the hydrate gradually moved to the liquid CO_2 phase while CO_2 in the liquid phase penetrated into the hydrate. MatLab was used as a post processor for the sampled data for detailed analysis of the decomposition process of the CH_4 hydrate during the

exchange. This was needed in order to distinguish the mass transfer behavior of the CH_4 and CO_2 liquid but was also a useful tool in organizing the data for more detailed illustrations the microscopic aspects of the exchange process in the hydrate. The observed decomposition process of CH_4 was found to proceed faster than the reformation of CO_2 due to CH_4 presence in both the small and large cages, whereas the guest molecule exchange of CH_4 with CO_2 could occur only in the large cages. Based on the simulation data presented, the results indicated that while the driving force is difference in chemical potential for the two components between the liquid phase and the hydrate phase for the exchange process is essentially dominated by mass transport limitation.

Keywords: Phase Field Theory; CH_4 hydrate; CO_2 hydrate; decomposition; reformation; salinity; exchange; resistivity

Acknowledgements

First, I would like to thank my supervisor Professor Bjørn Kvamme for conducting a good and excellent supervision to enable me fulfill this thesis. Through this period he has been both attentive and supportive about my work, and his comments and good ideas were of great importance. Thanks to Prof. Tatiana for corrections and providing structural order assistance done in this thesis.

Special thanks to my laboratory supervisor at the Reservoir Physics Department, Geir Eslend for his knowledge and guidance through my experimental work. His assessment of this thesis has been of great help. My sincere acknowledgement goes to PhD students, Mohammad Taghi Vafaei (Eman), Mohammed Qassim and especially Khuram Baig for their great assistance and comments to make this thesis a reality.

The efforts of my colleagues at the Reservoir Physics Department Jonas Odland and Knut Birkedal and those in my class Archana Parmar, Bjørnar Jensen, Amir Farmahini for always responding to my question and giving additional advices are also greatly appreciated. You created a study environment with great social network. Thanks to my friend Abdul Rahaman Diallo for inviting me for dinner during the entire preparation of this work.

Finally, it would have been difficult to complete this thesis without the enduring support, love and patience of Kristina Tufte and my baby Sarah Tufte Jalloh.

Bergen, February 2010

Alusine Jalloh

Table of Contents

Acknowledgements III
Bergen, February 2010 III
Nomenclature VI
1 Introduction 1
2 Background 4
2.1 Hydrate 4
2.1.1 Hydrate structures 5
2.1.2 Hydrate as a climate problem 7
2.1.3 Hydrate as a potential resource 8
2.2 Gas Production from Hydrate Reservoirs 8
2.2.1 Gas production studies based on destabilization of hydrate 8
2.2.2 Gas production through replacement of guest molecule 11
3 Thermodynamics 13
3.1 Gibbs free energy 13
3.2 Gibbs phase rule 14
3.3 Hydrate thermodynamics 15
3.3.1 Thermodynamic stability of hydrate 15
3.3.2 Fractional occupancy of small and large cavities of CO_2 and CH_4 hydrate 16
3.3.3 Fluid thermodynamics 19
4 Hydrate formation kinetics 20
4.1.1 Hypotheses on hydrate nucleation 26
4.1.2 Analysis of equilibrium relations of CO_2 and methane hydrates 29
4.1.3 Phase Field Theory 29
4.1.4 Hydrate formation and dissociation in nature 31
4.1.5 Porosity 32
4.1.6 Saturation 33
4.1.7 Using resistivity measurements 33
5 Experimental 37
5.1.1 Experimental layout description for experiment I and II 38
5.1.2 Filling fraction for experiment I and II 39
5.2 Experiment I: Resistivity measurement in porous media 39
5.2.1 Material used to measure resistivity 40
5.2.2 Procedure and problems encountered to measure resistivity 41
5.2.3 Experimental design I 43
5.2.4 Results and Discussion 46
5.2.5 Uncertainties 50
5.2.6 Conclusions – Resistivity measurements 51
5.2.7 Future perspectives 51
5.3 Experiment II: Methane production during carbon dioxide injection 53
5.3.1 Experimental design II 53
5.3.2 Procedure for methane hydrate formation and production during carbon dioxide injection in porous media 55
5.3.3 Results and Discussion 58
6 Simulations 64
6.1 Study area 64

6.2 Simulation basis 64
6.3 Simulation setup 66
7 Results and discussion 71
7.1 Concentration of CO_2 in hydrate and liquid phase 71
7.2 Extrapolation for CO2 77
7.3 Methane concentration in hydrate and liquid phase 78
7.4 Extrapolation for CH_4 83
7.5 Relationship between methane and CO_2 concentrations 84
7.6 Summary 87
7.7 Conclusion 88
7.8 Future perspectives 88
References 92
Appendix A: Experimental I 95
Appendix B: Experimental II 99
Appendix C: Simulation 102

Nomenclature

Symbol	Description	units
A	Crystal surface area , equation (4-5)	m^2
A_s, B_s	Constants of structure I small cavities (Appendix C- 4)	-
A_L, B_L	Constants of structure I large cavities, (Appendix C- 4)	-
C	Number of components in hydrate phase, equation (3-11)	-
$C_{J,i}$	Langmuir` constant for component *J* in cavity *i*	-
PFT	Phase Field Theory	-
MD	Molecular Dynamics	
n	Number of components	
N	No. of particles	moles
dU	Change in internal energy	J
dS	Change in entropy	$\frac{J}{K}$
V	Volume	m^3
dV	Change in volume	m^3
dG	Change in Gibbs free energy	J
dp	Change in pressure	bars
v_m	molar volume, equation (3-13)	(m^3/mol)
x	Mole fraction, equation (3-13)	
x	Distance, equations (4-11) and (4-12)	m
c	Concentration	$\frac{moles}{m^3}$
I_1, I_2	Distances, equation (7-1)	
c^{eq}	Equilibrium concentration, equation (4-5)	$\frac{moles}{m^3}$
v	Velocity	m/s
D	Diffusion coefficient	$\frac{m^2}{s}$
dm	Change in mass, equation (4-5)	g
dt	Change in time, equation (4-5)	s

F	Free energy functional, equation (4-7)	
f	Free energy density	$\frac{J}{m^2}$
f_L	Diffusivity coefficient for liquid	$\frac{m^2}{s}$
f_S	Diffusivity coefficient for solid	$\frac{m^2}{s}$
G	Local geothermal gradient	$\frac{^oC}{m}$
sI	Structure I	
g	Gravitational acceleration	$\frac{m}{s^2}$
ΔG^{tot}	Change in total Gibbs free energy, equation (4-1)	J
ΔG_s	Change in surface free energy, equation (4-1)	$\frac{J}{m^2}$
ΔG_v	Change in volumetric free energy	$\frac{J}{m^3}$
$P_{(z)}$	Hydrostatic pressure at depth *z,* equation (6-1)	bar
P_o	Initial pressure, equation (6-1)	bar
Z	Depth below the seafloor	m
Z_o	Water depth	m
$\mathring{A}$	Angstrom	m
$T_{(z)}$	Temperature at depth *z*	K/^{o}C
$\rho_{\ /}$	Sea water density	$\frac{kg}{m^3}$
R	Resistivity, equation (4-15)	ohms*m
A	Cross section area, equation (4-15)	m^2
V	Volt , equation (4-15)	volts
L	Length between electrode rings inside the sleeve, equation (4-15)	m
I	Current, equation (4-15)	Ampere (A)
$\rho_{\_I}$	Hydrate density	$\frac{kg}{m^3}$
$\rho_{\_I\,mix}$	Hydrate density	$\frac{kg}{m^3}$

T_o	Seafloor temperature	K/^{o}C
N_w	Number of water molecules per unit cell, (Table 2-1)	-
N_{Ava}	Avogadro`s number, equation (3-11)	$\frac{\text{molecules}}{\text{mol}}$
MW_J	molecular weight of component J, equation (3-11)	$\frac{\text{grams}}{\text{mol}}$
M_w	Molecular weight	(g/moles)
M_G	Molecular weight of guest	g/moles
h_{ij}	Cavity partition function of component j in cavity type i	
V_{cell}	Volume of unit cell (dimensions in Table 2-1)	
N	Number of cavity types in unit cells, equation (3-11)	-
$\theta_{\_}$	Filling of the small cavities	-
$\theta_{\_}$	Filling of the large cavities	-
HN	Hydrate number	
P_J	Partial pressure of component J	bars
K	Overall transfer coefficient	$\frac{\text{mole}}{\text{m}^2\text{s}}$
k_d, k_r	Reaction coefficients	$\frac{\text{mole}}{\text{m}^2\text{s}}$
r	Radius	m
r	Resistance , equation (4-15)	ohms
M_ϕ, M_c	Mobility coefficients	$\frac{\text{m}^2}{\text{s}}$
T	Temperature	K
R	Gas constant	$\frac{\text{J}}{\text{mol}*\text{K}}$
J	Flux (heterogenous) , equation (4-4)	$\frac{\text{mol}}{\text{m}^2*\text{s}}$
V_p, V_m, V_t, V_w and V_g	Pore, matrix, total, water and gas volumes, equation (4-13) and (4-14)	m^3
S_w, S_g	Water and gas saturation	
ϕ	Porosity , equation (4-13)	

Δg_{ji}^{inc}	Free energy of inclusion	J

Super & Subscripts

o	initial	-
w	water	-
z	depth	-
i	Cavity, phase	-
j	component	-
s	system	-
inc	inclusion	
eq	equilibrium	

Greek letters

θ_{iJ}	fractional occupation of cavity *i* by component *J*	
ρ	Density	Kg/m^3
v_i	Number of type *i* cavities per water molecule in unit cell (Table 2-1)	
θ_{ij}	Fractional occupancy of cavity *i* by component *j*	
μ_w^H	Chemical potential of water in hydrate	(J/moles)
μ_w^o	Chemical potential of water in an empty hydrate structure	(J/moles)
Δ	Change	
π	Number of phases	
τ	Degrees of freedom	
φ	Fugacity coeficient	

ω,ε	Model parameter	(J/mK)
β	beta	(moles/KJ)
γ	Interfacial free energy equation (4-1)	(J/m^2)
μ	Chemical potential	(J/moles)
ϕ	Structural order parameter	

Preface

The main focus of this work is exploitation of methane from hydrate, a solid like structure where water hydrogen bond creates cavities which traps the methane. Special emphasis is put on an exchange process in which carbon dioxide molecules exchange with methane in the occupation of the large cavities in hydrate structure I. A brief overview of the history and fundamentals of hydrate is given in sections 1 to 4 of the thesis. The rest of the thesis is divided into two parts which comprises my individual contributions. Experimental work, including design and testing of new experimental equipment, is described in section 5. Theoretical modeling is discussed in section 6.

1 Introduction

Gas hydrates are solid structures in which water molecules (host) under certain temperature and pressure conditions hydrogen bond to form cages that traps small non polar or slightly (eg CO_2, CH_4) polar molecules (eg H_2S) denoted as guest molecules. The structure is dominated by the water molecules and appears ice like. When the guest is a methane molecule, you have methane hydrate. Other gas hydrates being evaluated are ethane, propane, butane, hydrogen sulphide, nitrogen and the gas responsible for the most global warming CO_2.

Following Sir Humphry Davy discovery in 1810, these compounds basically remained as a laboratory curiosity until their formation was identified as responsible for plugging natural gas pipelines by Hammerschmidt, 1934 (Makogon 1981). This led to an intense study of the thermodynamics of hydrates formation which resulted in the establishment of reliable models for phase equilibria calculations which enabled the development of the so-called thermodynamic inhibitors of hydrate formation, such as methanol and glycols (Anderson and Prausnitz 1986; Ballard and Sloan 2002).

Gas hydrates are now regarded as a promising alternative in the solution of some important global issues like energy supply and reducing impact of CO_2 emissions on climate change through safe storage of CO_2. On account of gas hydrates great capacity to store gases, they may provide a means not only to recover, transport and store natural gas for energy use but also to store CO_2 and safely dispose it in the ocean (Saji, Yoshida et al. 1992; Yamasaki, Teng et al. 2000; Lee, Chun et al. 2002).

The success of these potential applications is mainly hindered by technological problems associated with hydrate formation, including slow formation rates and the economics. In order to overcome such challenges, a better understanding of hydrate formation kinetics is required. Compared to hydrate thermodynamics, hydrate kinetics is still poorly understood (Englezos and Ngan 1993; Sloan 2003; Sloan 2005). Little work was done on the subject before the 1980s, when an increasing number of studies related to hydrate kinetics started to appear in the literature, most of which concerned with hydrocarbons and CO_2, obviously driven by gas storage applications.

Interest in natural methane hydrate is rapidly expanding around the globe. Many nations and many areas offshore including the US, Alaska, Canada, Japan, Norway, and Australia etc have been appraised to various extents on the investigation of methane hydrate deposit (Figure 2-1). Information on these areas becomes available on specific pages elsewhere on their webpage. Before attempts of methane extraction from hydrates can begin, much more needs to be known. Fundamental questions such as quantities, distributions, modes of occurrence, physical and chemical properties, and many others, must be answered. Such information is necessary to develop computer models which can accurately predict the behavior of hydrates systems under changing conditions. As information is gained and analytical tools are developed, broad natural methane hydrates topics are approached such as climate problems, resource potential etc (Figure 2-3).

The present thesis introduces some basic concepts and major issues concerning gas hydrates. Chapter 2 describes the background of hydrates, what they are, where they are found and also their structures. Gas production from hydrate reservoir was also included in Chapter 2. Chapter 3 outlines the thermodynamics and hydrate thermodynamics followed by hydrate formation kinetics in Chapter 4. Following chapters addresses each stage of hydrate formation, namely crystals nucleation and growth, a brief summary of the equilibrium analysis and Phase Field Theory model applied to CH_4 and CO_2 hydrate is also given.

My contribution in this work is as illustrated in section 5 and 6. Section 5 describes two laboratory experiments designed to monitor hydrate formation in porous media. The primary aim of these experiments in collaboration with the Reservoir Physics Department University of Bergen is to design, complete and test experimental setups to run laboratory experiments. The first setup could be used in resistivity measurements during hydrate formation while the second can be used for production studies of methane from its hydrate during CO_2 sequestration in porous media.

The secondary goal of the first experiment was to study electrical resistivity during hydrate formation in porous medium (core plug). Electrical properties of the matrix such as resistivity may have a great impact on gas hydrate and these may be considered as the most effective parameter for characterizing hydrate bearing matrix (Yongjun, Weidong et al. 2008). Therefore, it is important to study resistivity in natural gas hydrates in the development of gas hydrate resources.

Followed was exchange of methane by the use of liquid CO_2 in porous media. The main objective was to form methane hydrates in porous medium and then produce methane from its hydrates during CO_2 sequestration. In particular, these experiments are the first to be conducted at the University of Bergen Norway.

The primary goal of section 6 is a non- gas hydrate problem to test the basic mass and heat transfer capabilities in the Phase Field Theory code. The secondary goal specifically focuses on molecular dynamics (MD) simulation to study methane hydrate dissociation and the subsequent reformation of CO_2 hydrate at ambient temperatures and high pressures. It is in the interest of getting an overview of the potential recovery of methane gas from its hydrates as CO_2 is stored as CO_2 hydrate. Since CO_2 is a greenhouse gas, the process is a favorable way as long time storage of CO_2 and enables the ocean floor to remain stabilized even after recovering the methane gas (Caldeira and Wickett 2005). Methane hydrate has the same structure as CO_2 hydrate of which the unit cells consists of two small cages and six large cages. Sloan et al (1998) determined the size of structure I depending on the diameter of the guest molecule and cavity size of the water cage. Therefore, the limiting range for sI formers is between 4.1 to 6.0 Å which signifies methane to enter both small and large cages whereas CO_2 molecules may only occupy the large cages.

2 Background

Hammerschmidt in the 1930s discovered problems often experienced by gas pipelines during the winter months were caused not by the freezing of water in the pipeline, an assumption very common until then, but by formation of gas hydrates (Makogon 1981). A lot of research has been developed on gas producing industries to find methods of preventing gas hydrates formation and accumulation in wells drilled for gas and in pipelines. Hydrate plugging is still a big problem for the oil and gas companies and there is still a major effort to find out more about hydrates. His discovery drew concern to different research to find a way to solve the problem. In the gas and oil industry, different techniques are today used to prevent hydrate formation such as thermodynamic and kinetic inhibitors.

2.1 Hydrate

Methane hydrate is not a familiar term to many, but it is gaining popularity in the energy sector. It is being evaluated as a potential future fuel. Methane hydrates are crystals with well defined structures that form under low temperatures and high pressures, huge amounts of which underlie our oceans and polar permafrost (Sloan 1998).

Figure 2-1: World map showing occurrences of natural gas hydrate or their indirect evidences (Program)

Figure 2-1 shows the widespread presence of methane hydrates around the world which has given promises to international balance of energy supply, and to provide energy self-sufficiency to many nations which are dependent on others.

2.1.1 Hydrate structures

Depending upon the size of the guest molecule (gas), water molecules arrange themselves in different ways around it (host) in natural gas hydrates, resulting in hydrates with three different crystalline structures known as sI, sII and sH (Figure 2-2). Together, these structures are formed by five polyhedra in which the vertices are the oxygen atoms of the water molecules and the edges represent hydrogen bonds. Following Jeffrey's nomenclature (Jeffrey 1984) the polyhedral $n_i^{m_i}$ has m_i faces of kind i containing n_i edges. Hence, the pentagon dodecahedron, for instance, is called 5^{12} because it has 12- sided polyhedron where each face is a regular pentagon; the tetrakaidecahedron, for example, is named $5^{12}6^2$ because it has 12 pentagonal and 2 hexagonal faces. The dodecahedral cages are smaller than the tetrakaidecahedral cages; thus the dodecahedron cages are often referred to as small cages, whereas the tetrakaidecahedra are referred to as large cages (Table 2-1). Small cages comprises of 2 cavities while the large cages consist of 6 cavities together they form structure I hydrate. For the purpose of this study, only the main differences between the small and large cages of sI hydrate are studied. More details about sII and sH are given elsewhere (Sloan and Koh 2008).

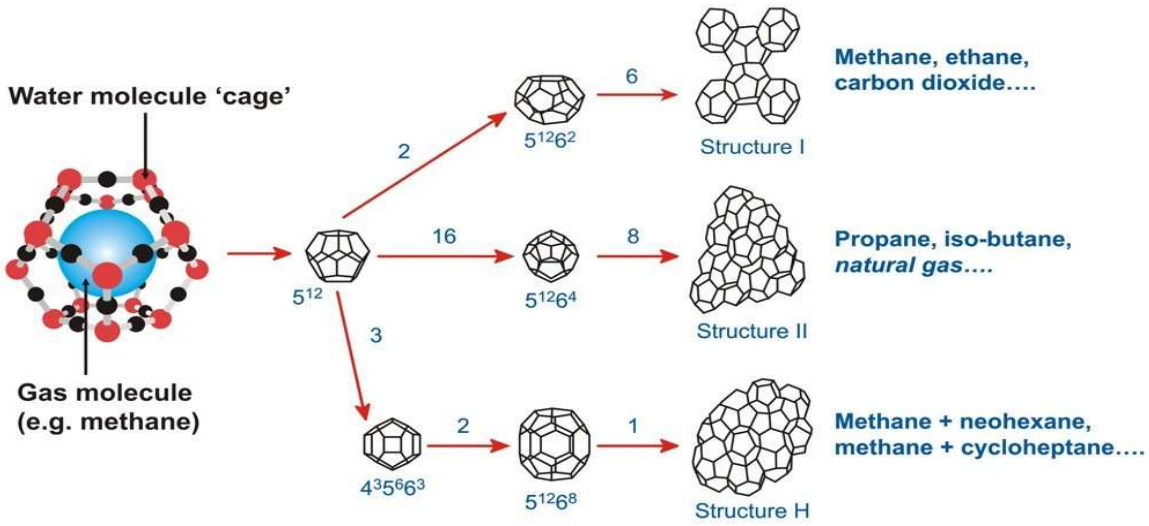

Figure 2-2: Three hydrate unit crystals and constituent cavities modified by (Sloan Jr).

Figure 2-2 shows hydrates with three different crystalline structures known as sI, sII and sH. The fundamental hydrate building unit found in all structures is the small cavity also called the polyhedron 5^{12}. Since the polyhedral share faces in the crystalline structure, only 20 out

of the 60 theoretically needed water molecules are required to form this cavity. Eight polyhedrons are held together by 46 water molecules in sI crystal cell (Sloan and Koh 2008).

Table 2-1: Cavities in gas hydrates adapted from (Sloan and Koh 2008)

Hydrate crystal structure	I		II		H		
Cavity	Small	Large	Small	Large	Small	Medium	Large
Description	5^{12}	$5^{12}6^2$	5^{12}	$5^{12}6^4$	5^{12}	$4^35^66^3$	$5^{12}6^8$
Number of cavities per unit cell	2	6	16	8	3	2	1
Average cavity radius (Å)	3.95	4.33	3.91	4.73	3.91†	4.06†	5.71†
Coordination number*	20	24	20	28	20	20	36
Number of waters per unit cell	46		136		34		

*Number of oxygens at the periphery of each cavity.
†Estimates of structure H cavities from geometric models.

Table 2-1 shows small cages and large cages in natural gas hydrates. Regardless of the type of crystalline structure, each hydrate cavity contains at most one guest molecule.

Molecules smaller than 3.95 Å in diameter are too small to stabilize the small cavity, while molecules with a diameter greater than 4.33 Å are too large to enter the small cavities of sI hydrates. Therefore, the average diameter of the sI cages ranges from 4.1-6 Å, which signifies the limiting ranges for the molecular diameter of sI hydrate formers. For pure systems, the size ratio of the guest molecules to cavity is a guide to determining crystal structure. For mixtures, the hydrate structure is usually dictated by the larger guest molecule. For sI hydrates, there is a possibility for double occupancy by hydrates. Consequently, all hydrates do contain more water than predicted by the ideal composition (Sloan 1990). According to Sloan (Sloan 1998), typical occupancies of large and small cavities are 50% and 95%, respectively. Detailed descriptions of gas hydrates structures are given elsewhere (Makogon 1997; Sloan 1998). Broad natural methane hydrates topics are approached such as climate problems, resource potential etc (Figure 2-3).

2.1.2 Hydrate as a climate problem

Figure 2-3 (Left) Earthquakes trigger gas-hydrate instability that in turn triggers massive slumping of sea-floor sediments and tsunamis. Installing large structures on the sea bed might result in rapid release of gas and instability of their foundations. Any release of methane promotes global warming. (Right) The huge potential for developing gas hydrates as resources – they are readily discovered by their distinct 'signatures' on seismic sections (openlearn). Global warming has drawn increasing concern over the years leading to agreement that CO_2 emissions need to be reduced in order to limit climate change and global warming effects. In the work of research around the world to record a progressive increase in global air temperatures, methane is a key greenhouse gas, along with CO_2 and water vapor. By this, one of the primary goals of some research is to investigate the possible connection between natural methane hydrate and global climate processes.

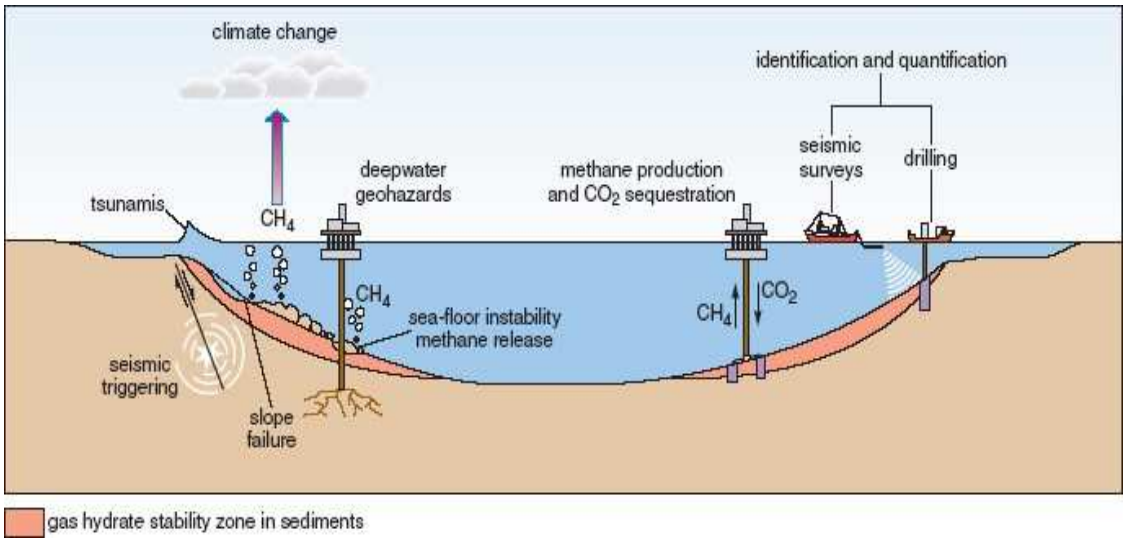

Figure 2-3: Illustration of the major issues concerning gas hydrates in sea- floor sediments (openlearn)

Figure 2-3 (Left) Earthquakes trigger gas-hydrate instability that in turn triggers massive sliding of sea-floor sediments and tsunamis.

On the negative side of Figure 2-3 (left), it is now recognized that gas hydrates are a potential geohazard. Dissociation of hydrates at the base of the gas hydrate stability zone can cause increased potential sea-floor failure. Slope failure can threaten underwater installations and, in extreme cases, generate tsunamis. It has even been suggested that during periods of climatic warming such as we are experiencing at present, onshore hydrates become destabilized, liberate methane to the atmosphere and thus accelerate global warming.

2.1.3 Hydrate as a potential resource

On the positive side of Figure 2-3 (right), the potential of methane hydrates as a major strategic energy reserve is obvious and much research is being conducted to develop appropriate extraction techniques. This extends to considering whether methane production could be combined with CO_2 disposal, thus addressing the twin challenges of this century – reducing the emissions of greenhouse gases and providing a low-carbon fuel to replace oil and coal.

In addition to environmental concerns and energy potential (Figure 2-3), the improved understanding of the basic nature of natural gas hydrate will allow for more accurate assessment of the resource potential of methane hydrate. Exploration tools that better define the location of good spots, sampling tools which allow detailed characterization of the resource, and production testing to analyze the extraction of the resource; these are all important areas of research and development that will lead us closer to production of methane from hydrate as a potential energy source. The promising production results of recent well tests in Canada and Japan are starting to look toward hydrate as a possible source of energy for the future (Kurihara 2008).

2.2 Gas Production from Hydrate Reservoirs

2.2.1 Gas production studies based on destabilization of hydrate

The energy potential in natural gas hydrates is vast, and several different production schemes are referred to as possible production schemes in the literature. Currently, literature refers to two different groups of gas production schemes, where the first group is based on dissociation of hydrates by changing the reservoir conditions so that the gas hydrate is moved outside the stability region shown in Figure 2-4 and Figure 2-5. In the context of this thesis only three different production methods are considered:

- Hydrate dissociation through depressurization
- Hydrate dissociation through thermal injection
- Hydrate dissociation through inhibitor injection

Hydrate dissociation through depressurization is a method used when the reservoir pressure is decreased into the unstable hydrate region, which is below or to the right of the phase

diagrams illustrated in Figure 2-4 and Figure 2-5, the gas hydrate will start dissociating. Depressurization is by many considered the most cost efficient production method, because the added energy during production is kept at a minimum.

Thermal stimulation is another production method, where steam or hot water is supplied to the reservoir in order to move it outside its stability region. This production method requires a lot of energy, because liquid must be heated and then transported into the hydrate reservoir. In addition, hydrates do not conduct heat very well, and subsequently this method will not be very efficient.

Injection of different inhibitors has also been considered, where the phase diagrams shown in Figure 2-4 and Figure 2-5 will be shifted to the left, thereby reducing the hydrate stability region.

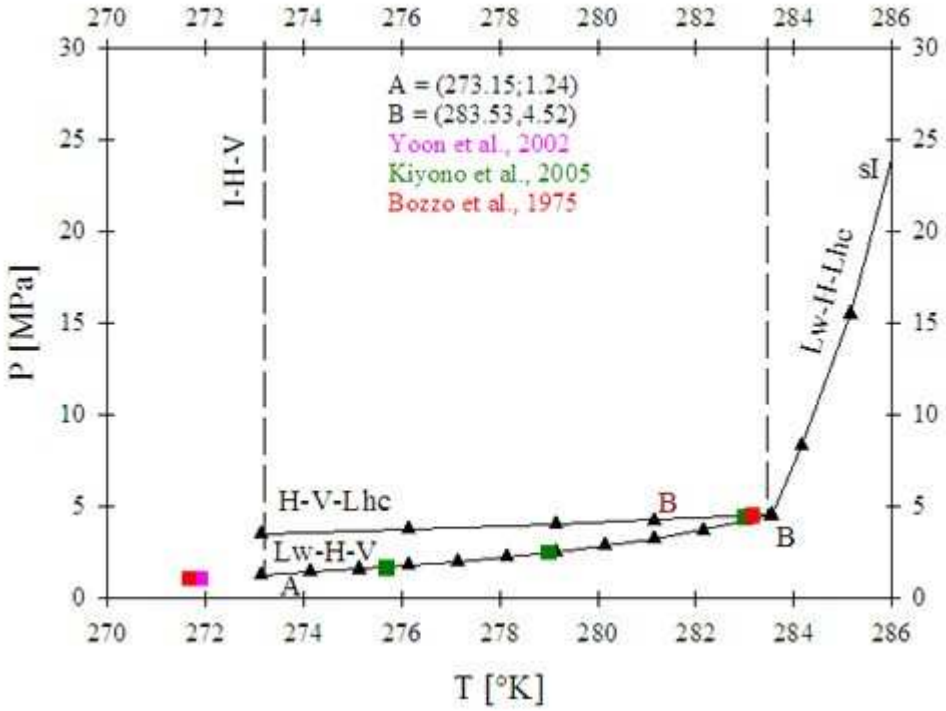

Figure 2-4: P-T thermodynamic equilibrium for CO_2 hydrate. The different phases are detailed as follows: I = ice, Lw = liquid water, V = vapor or gas, and Lhc = liquid hydrocarbon (Garcia June 30, 2008).

Figure 2-4 shows the different phases involved in the thermodynamic equilibrium of CO_2 hydrates. The abbreviations represent phase transitions within hydrate stability conditions.

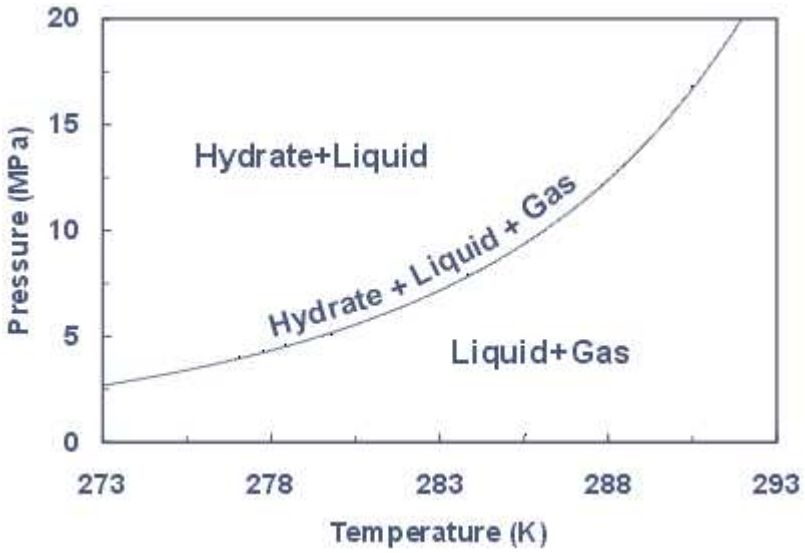

Figure 2-5: Pressure versus temperature phase diagram for simple methane hydrates (Tohid 2005)

Figure 2-5 phase diagram for simple methane hydrates was shown. On the left indicates the three phase lines $I - \mathrm{H} - \mathrm{V}$; $L_w - \mathrm{H} - \mathrm{V}$ and to the right phases exist for liquid water or ice and the guest component as vapor or liquid.

Sloan et. al (2008) have recently measured equilibrium pressures of hydrates formed from CO_2 and various hydrocarbons. Similar diagram was generated using CSMHYD (Sloan 1998) as illustrated in Appendix C- 3. Equilibrium pressures and simulation zones of the methane – CO_2 sI hydrate are shown in Appendix C- 3 .

2.2.2 Gas production through replacement of guest molecule

The second group of production schemes is based on injection of a gas that provides thermodynamically more stable gas hydrates than the existing guest molecule does. CO_2 is one such gas and extensive experimental work supports possibility of replacing CH_4 with CO_2 (Ohgaki, Takano et al. 1996). CO_2 provides increased stability of the gas hydrate and the extent of the exchange is dependent upon the state of the CO_2, where gaseous CO_2 is more effective than liquid (Hester and Brewer 2009). Several experiments have shown that exposing CH_4 hydrates to CO_2 will lead to an exchange process where the hydrates prefers occupation by CO_2, thus an exchange process takes place (Lee, Seo et al. 2003; Ota, Morohashi et al. 2005; Jadhawar, Mohammadi et al. 2006). This is also supported by simulations (Phale, Zhu et al. 2006). Reasons for the exchange process is the mentioned difference in thermodynamic stability, but also due to the exothermic nature of CO_2-hydrate formation, which induces heat that may accelerate the exchange rate through rapid CH_4 hydrate micro scale dissociation. In fact, the released heat through CO_2 hydrate formation (-57.98kJ/mol) is higher than the heat required for CH_4 hydrate dissociation (54.49kJ/mol), which will accelerate the exchange process (Goel 2006). In addition to provide increased support and stability, sequestration of CO_2 into hydrate stable regions also offers a favorable approach when looking at long-term storage of CO_2, which may reduce the possible global warming problem.

3 Thermodynamics

While it is possible to adjust the number of controlled variables in the design of experiments so that the system is able to reach an equilibrium state given sufficient time Nature is more complex since local conditions of temperature, pressure and fluid concentrations are fixed by local conditions. very often in natural systems it is not possible to reach an equilibrium state because the local systems of components and phases with given conditions may be over determined with respect to Gibbs Phase rule. In this case the combination of first and second laws of thermodynamics dictates the progress of the system under constraints of mass- and energy-transport. Practically this means that with pressure, temperature and masses as variables the system dynamically will progress towards local free energy minimum at any time. A brief overview of basic thermodynamics involved is given here and it also links to the theoretical approach used in this work, Phase Field Theory, which basically is a free energy minimization.

3.1 Gibbs free energy

The starting point for most thermodynamic considerations is the laws of thermodynamics. The first law states the change in the internal energy of a closed thermodynamic system is equal to the sum of the amount of heat energy supplied to the system and the work done on the system. The second law state a quantity named entropy, the total entropy of any isolated thermodynamic system tends to increase over time. These two laws can be mathematically put together to calculate variables such as temperature and pressure of a system. Combining the two laws gives for the changes in internal energy for phase *i*:

$$dU^{(i)} \leq T^{(i)}dS^{(i)} - p^{(i)}dV^{(i)} + \sum_{l=1}^{n} \mu_l^{(i)} dN_l^{(i)} \tag{3-1}$$

The summation is done over all present components $l = 1, 2\ldots$ n. S is the entropy; μ in this equation is the chemical potential and N the number of moles of a specific compound. The equality is for reversible changes, which is only a theoretical possibility. So, for all real and irreversible changes we will have the "less than" situation. Transformation of the natural variables is accomplished through Legendre transforms by subtracting $d\left(T^{(s)}S^{(i)}\right)$ on both

sides and adding $d\left(P^{(i)}V^{(i)}\right)$ on both sides. The resulting function is termed Gibbs free energy:

$$dG^{(i)} \leq -S^{(i)}dT^{(i)} + V^{(i)}dp^{(i)} + \sum_{l=1}^{n} \mu_l^{(i)} dN_l^{(i)} \tag{3-2}$$

Gibbs free energy can, in a simplified sense, be considered as the "available" energy level under the constraints of losses associated to entropy generation. $V^{(i)}dp^{(i)}$ is termed technical work, or shaft work, since the work involved in pushing fluids internally in the systems is subtracted. The last term on the right hand side is called chemical work and is the work related to extracting or inserting particles.

Removing a molecule from the system involves releasing the molecule from the interaction energy of the surroundings and also involves an entropy contribution related to reorganization of the system.

3.2 Gibbs phase rule

In the work on heterogeneous equilibria published in 1870's, J.Willard Gibbs (Gibbs 1870) derived a simple rule which determines the number of degrees of freedom for a heterogeneous system in equilibrium. The number of degrees of freedom for a system is the number of intensive variables (often taken as the pressure *P*, temperature *T*, and composition fraction) which may be arbitrarily specified without changing the number of phases.

If a system in equilibrium contains π phases and *n* components then the phase rule states that the number of degrees of freedom τ is given by:

$$\tau = n - \pi + 2 \tag{3-3}$$

Typical phases are solids, liquids and gases. A system involving one pure chemical is an example of a one-component system. Two-component systems, such as mixtures of water and ethanol, have two chemically independent components.

3.3 Hydrate thermodynamics

This chapter treats the development of the thermodynamic functions needed for the Phase Field Theory presented in chapter 4.1.3. Much of the theory in section 3.1 and 3.2 was found in a book on classical theoretical physics(Greiner, Neise et al. 1995). Most of the data in section 3.3.1 and 3.3.3 were taken from (Svandal, Kvamme et al. 2006). Section 3.3.2 was taken from Sloan and Makogon (Makogon 1981; Sloan and Koh 2008).

3.3.1 Thermodynamic stability of hydrate

Based on their analysis on the treatment of thermodynamic stability of hydrates, van der Waal and Platteew (Vanderwaals and Platteeuw 1959), considered fixed water molecules. He suggested that there is no guest – water interaction and he also neglected the interactions with surrounding guest molecules. This may be adequate for small guest molecules with weak interactions. On the other hand, molecules like CO_2 are large enough to have a significant impact on the librational modes of the water molecules in the lattice. Kvamme and Tanaka (Kvamme and Tanaka 1995) suggested an alternative approach to consider the guest movements from the minimum energy position in the cavity as a spring, and evaluate the free energy changes through samplings of frequencies for different displacements in the cavity. A molecule like methane will, as expected, not have significant impact on the water movements (Kvamme and Tanaka 1995). CO_2 on the other hand, will change water chemical potential when compared to the assumption of undisturbed fixed water molecules. Their theory is based on the extended adsorption theory with respect to the minimum free energy of the water molecules in the cavity for simplified models of some larger molecules filling the large cavity of structure I.

The expression for chemical potential of water in hydrate is derived from the macro canonical under the constraints of constant amount of water, corresponding to an empty lattice of the actual structure.

$$\mu_w^H = \mu_w^{O,H} - \sum_i RT\nu_i ln\left(1 + \sum_j h_{ij}\right) \tag{3-4}$$

Details of the derivation are given elsewhere (Kvamme and Tanaka 1995) and will not be repeated here. $\mu_w^{O,H}$ is the chemical potential for water in an empty hydrate structure and h_{ij} is the cavity partition function of component j in cavity type i. The first sum is over cavity types, and the second sum is over components j going into cavity type i. Here ν_i is the

number of type i cavities per water molecule. For sI hydrate, the small cage contains 2 cavities and 46 water molecules while the large cage comprises of 6 cavities and 46 water molecules which represents $\nu_{small} = \frac{1}{23}\ and\ \nu_{large} = \frac{3}{23}$ respectively. Similarly for sII hydrate $\nu_{small} = \frac{16}{136} = \frac{2}{17}\ and\ \nu_{large} = \frac{8}{136} = \frac{1}{17}$.

The cavity partition function suggested by Kvamme and Tanaka may thus be written as:

$$h_{ij} = e^{\beta\left(\mu_j^H - \Delta g_{ji}^{incl}\right)} \tag{3-5}$$

Where Δg_{ji}^{incl} now is the effect of the inclusion of the guest molecule j in the cavity of type i, which as indicated above is the minimum interaction energy plus the free energy of the oscillatory movements from the minimum position. At hydrate equilibrium the chemical potential is equal to that of the chemical potential of the guest molecule in its original phase (chemical potential of dissolved CO_2 or CH_4 for the case of hydrate formation from aqueous solution). Equation (3-5) can be solved to give the chemical potential for the guest as a function of the cavity partition function:

$$\mu_j^H = \Delta g_{ij}^{incl} + RTlnh_{ij} \tag{3-6}$$

Equation (3-5) is basically derived from an equilibrium consideration but may be used as an approximation for relating chemical potential to composition dependency.

3.3.2 Fractional occupancy of small and large cavities of CO_2 and CH_4 hydrate

Fractional occupation (θ_{ij}) for small and large cavities by a molecule of type J is one of the most useful equation in the method of hydrate prediction and it contains the Langmuir constant $\left(C_{j,i}\right)$ for one guest component J and cavities i filled. Knowing the partial pressures of the components in the gas phase and Langmuir`s constant, the degree of filling of the small cavities (θ_s) and of the large cavities (θ_L) of the hydrate by the separate hydrate forming components is determined by Sloan (Sloan and Koh 2008) as follows:

$$\theta_{ij} = \frac{C_i P}{1 + C_i P} \tag{3-7}$$

where $C_{j,i}$ is the Langmuir`s constant for component in cavity i, P is the partial pressure of component J.

By setting $h_{ij} = C_{j,i}P$ the relation between the filling fraction, the mole fractions and the cavity partition function will also result:

$$\theta_{ij} = \frac{h_{ij}}{1 + \sum_j h_{ij}} \tag{3-8}$$

Because of the size of CO_2, it can only fit into the larger cavities, and unless some other guest molecule is present, the small cavities will then all be empty. For a system with only one component occupying the large cavities, the chemical potential of the guest molecule would be reduced to:

$$\mu_j^H = \Delta g_{ij}^{incl} + RTln\left(\frac{\theta_{ij}}{1 - \theta_{ij}}\right) \tag{3-9}$$

For methane, which can occupy both large and small cavities, a more appropriate approach is needed. We start out by assuming the chemical potential of methane in the two cavities is the same. This gives a proportional relation between the two partition functions independent on composition.

Makogon (Makogon 1981) determined Langmuir`s constant for individual components depending on temperature from:

$$\lg C_{j,i} = 0.43429(A - BT) \tag{3-10}$$

where A and B are constants, the values of which are shown in Appendix C- 4; and T is temperature of the system being examined, K.

By finding the degree of filling of the small and large cavities of hydrate by individual hydrate forming components, their relative contents in the hydrate are calculated.

To calculate hydrate density for CH_4 and CO_2, dissociation pressure was calculated. In their work Sloan et.al (2008), hydrate density may be determined based upon a unit crystal. Additional required input data are the dimensions of a unit crystal, the number of water molecules per crystal and the number of small and large cavities per unit crystal as specified in Table 2-1. Based upon a single unit cavity, the hydrate density (ρ_H) may be calculated by:

$$\rho_H = \frac{N_W M_{W_{H_2O}} + \sum_{j=1}^{C} \sum_{i=1}^{N} \theta_{ij} \upsilon_{ij} M_{W_j}}{N_{ava} V_{cell}} \quad (3\text{-}11)$$

where

N_W= number of water molecules per unit cell (Table 2-1)

N_{ava}= Avogadro`s number, $6.023*10^{23} \frac{\text{molecules}}{\text{mol}}$

M_{W_j}= molecular weight of component *J*

θ_{ij}= fractional occupation of cavity *i* by component *J*

v_i = number of type *i* cavities per water molecule in unit cell (Table 2-1)

V_{cell}= volume of unit cell (dimensions in Table 2-1)

N = number of cavity types in unit cells

C = number of components in hydrate phase

The hydration number is then calculated as:

$$HN = \frac{46}{2\theta_S + 6\theta_L} \quad (3\text{-}12)$$

where,
HN is the hydration number, 46 is the member of water molecules in sI hydrate, $2\theta_s$ represents 2 cavities in the small cage and $6\theta_L$ denotes 6 cavities in large cage. By definition hydration number is the number of molecules of water with which an ion can combine in an aqueous solution of a given concentration.

3.3.3 Fluid thermodynamics

The following form is assumed for the volumetric Gibbs free energy of the fluid phase, f_l:

$$v_m f_l = c\mu_g(T, P_o) + (1 - c)\mu_w \tag{3-13}$$

Here v_m is the molar volume c is the concentration in mole fraction μ_g and μ_w are the chemical potentials of the guest molecule and water, respectively. In general the chemical potential for a quest of type i, dissolved in water can be expressed by the following equation:

$$\mu_i = \mu_i^{\infty}(T, P_o) + RTln(c_i\gamma_i) + v_i(P - P_o) \tag{3-14}$$

Here $\mu_i^{\infty}(T, P_o)$ is the chemical potential in water of component i, at infinite dilution. R is the universal gas constant and γ_i is the activity coefficient of the hydrate guest in an aqueous solution in the asymmetric convention (γ_i approaches unity in the limit of x becoming infinitely small). The chemical potentials at infinite dilution as a function of temperature are found by assuming equilibrium between fluid and aqueous phases $\mu_i^L = \mu_i^{aq}$ at low pressures where the solubility is very low. The chemical potential for water can be described as:

$$\mu_w = \mu_w^{pure}(T, P_o) + RTln(c_w\gamma_w) \tag{3-15}$$

Here $\mu_w^{pure}(T, P_o)$ is the chemical potential of pure water.

A system that can reach equilibrium has one and only one basic equation for the final equilibrium condition. The thermodynamic properties can be estimated by considering the equilibrium between liquid and aqueous carbon dioxide or methane, $\mu_i^{pure}(T, P_o) = \mu_i^{aq}(T, P_o)$.

4 Hydrate formation kinetics

The process of hydrate formation is similar to crystallization (Makogon 1981; Sloan 1990) and can be divided into two steps: nucleation and growth. The phenomena which affect the gas (guest) – water (host) cluster formation are of interest to understand the nucleation process. The gas – water cluster play an important role in the hydrate nucleation process. This is a random micro scale process, and cannot be detected macroscopically.

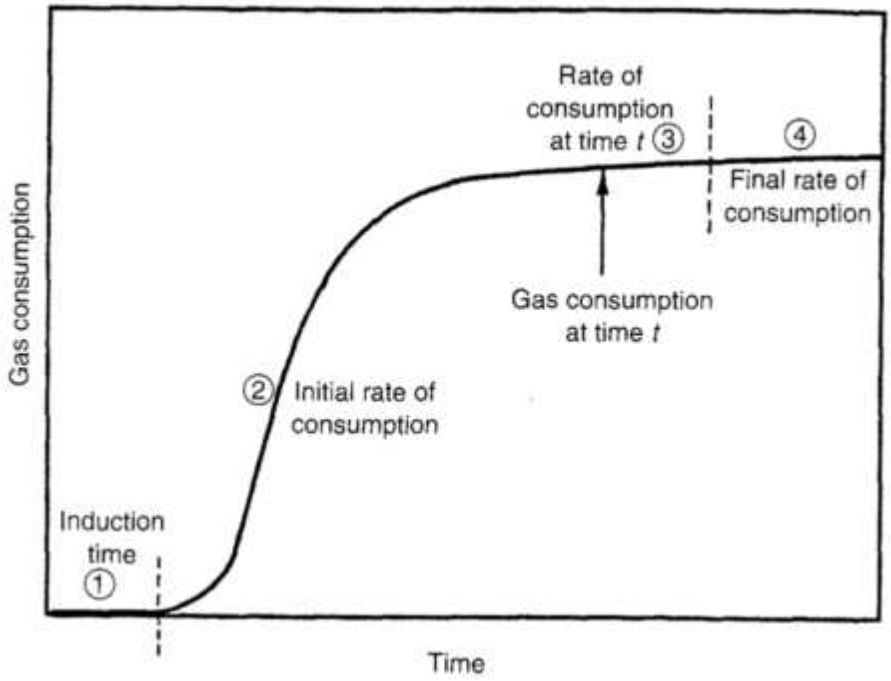

Figure 4-1: Typical Gas Consumption Plot versus time for hydrate formation (Sloan and Koh 2008).

Figure 4-1 illustrates an experiment performed by mixing a hydrate former and water, measured the rate of gas consumption (Sloan and Koh 2008). Several points of interest are marked on Figure 4-1. It shows the cumulative moles of gas consumed due to its dissolution or hydrate formation with time during an experiment. The moles of gas consumed at point 1 represents the amount of gas dissolved corresponding to the three phase hydrate equilibrium pressure at the experimental temperature. Things start at point 1. Induction period starts when a hydrate crystal starts to form (left of Figure 4-1). This is a random microscopic process and cannot be detected macroscopic. With the same unstable cluster that was formed with water and gas molecules, they will start to form, dissociate and sharing surfaces until a critical mass is reached. The metastable region between point 1 and 3 is characterized by the hydrate nucleation processes. The point 3 represents the point at which stable critical sized hydrate nuclei appear. Hence, the formation and dissociation occur at random until the hydrate growth

process begins at point 3 and proceeds along at point 4 were the critical size has been reached then the hydrate will grow steadily (right of Figure 4-1 point 4).

Hydrate formation is a phase transition which requires a new phase to form from one or more original phases. On account of the phase transition between for example gas and liquid, the separation of a new phase from an original phase requires the formation of an interface, which is associated with a positive variation of the Gibbs free energy. The molecules in the interfacial region in (Figure 4-2) are here referred to as $\Delta G_{surface}$. At the beginning of the process, the term related to the interfacial area (ΔG_s), always have the lowest free energy than those in the bulk phase referred to ΔG_{volume} which grows with the cluster radius and thus dominates so that the formed clusters are more likely to decompose than to grow. These two components form the total Gibbs free energy of the system ΔG^{tot}, with opposite signs, depending on the size of the formed cluster. Since the magnitude of the term associated with the bulk phase (ΔG_v) increases with the cluster radius, a minimum radius is eventually reached, known as the critical radius r_c at which ΔG^{tot} reaches its maximum value. At this point, as $\frac{d(\Delta G^{tot})}{dr} = 0$, the probabilities of cluster growth and decomposition are equal. The individual particles compete and the strongest with the lowest free-energy always dominate and this is always associated with the new phase (ΔG_v) dominating the old phase (ΔG_s), with a steadily decrease in the Gibbs free energy in favor of the new phase and the particle will grow for clusters with $> r_c$. Growth is always associated with a reduction in the Gibbs free energy of the system, being, thus, spontaneous.

Once the clusters have formed they will start to agglomerate by sharing faces, until the crystal reaches a critical size, r_c (Figure 4-2), formation and dissociation occurs randomly. After critical size has been reached steady hydrate growth period has initiated. If the critical sized crystal is not competing with other crystal on mass access the crystal will grow without decay after this stage.

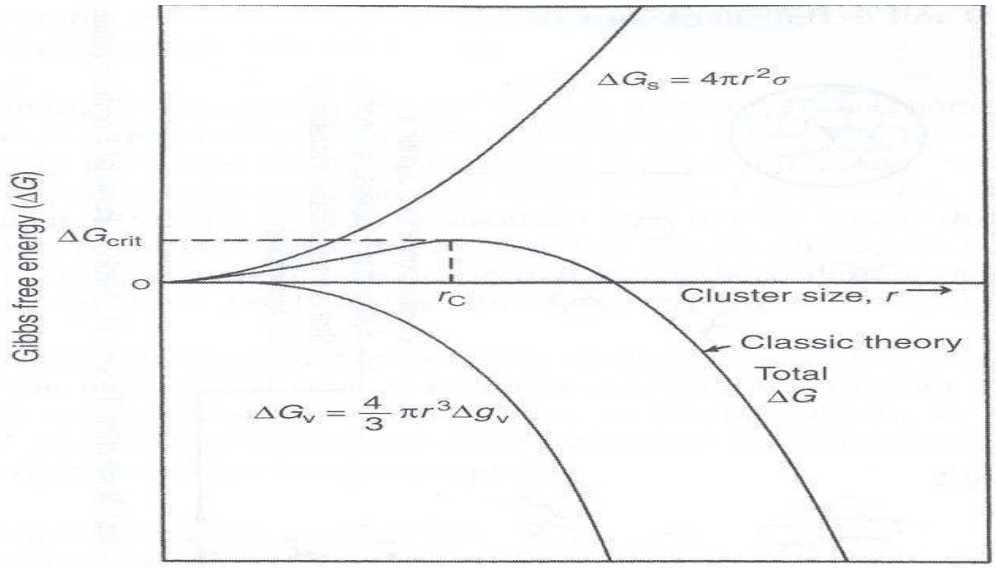

Figure 4-2: Comparison of the surface/interfacial free energy (ΔG_s) and the volume free energy (ΔG_v) as functions of cluster size (r) modified by (Sloan and Koh 2008)

Figure 4-2 shows the Gibbs free energy changes in a phase transition process during hydrate formation. According to classical nucleation theory, if we assume a spherical particle and homogenous nucleation, the total energy of the particle is the sum of the surface free energy and the volume free energy given by:

$$\Delta G^{tot} = \Delta G_s + \Delta G_v = 4\pi r^2\gamma + \frac{4}{3}\pi r^3 \Delta g_v \tag{4-1}$$

where γ is the interfacial free energy per unit area which is the sum of free energy of all the molecules present at the interface between different materials and Δg_v is the free energy change per unit volume *r* is the radius of the nucleus.

At a critical point, the free energy of formation obeys the condition $\frac{d(\Delta G^{tot})}{dr} = 0$. Hence the radius of the critical nucleus r_c and the maximum value of ΔG are obtained by differentiating Equation (4-1 and setting the result to zero to obtain:

$$r_c = -\frac{2\gamma}{\Delta g_v} \tag{4-2}$$

where

$$\Delta g_v = -\rho_c kt \ln S \qquad S = supersaturation\ ratio$$

The critical free energy is given by:

$$\Delta G^{crit} = \frac{4\pi r_c^2 \gamma}{3} \tag{4-3}$$

The nucleation rate $\vec{J}$ which is vector can be calculated from classical nucleation theory using the equation:

$$\vec{J} = J_o \times e^{-\frac{\Delta G^{tot}}{RT}} \tag{4-4}$$

where $\vec{J}$ is the flux calculated for homogenous formation $\left(\frac{moles}{m^3 s}\right)$ and for heterogeneous formation, $\left(\frac{moles}{m^2 s}\right)$ J_o is the kinetic mass transfer term and the exponential term as the thermodynamic term.

The heat transport term since pressure reduction method may be rate limited by heat transport released heat transport module is given as:

$$\Delta H = H^H - H_w^{liq} \times X_w^H - \sum H_j^H \times X_j^H$$

$$dQ = K_{structure} \times A \times \Delta T = n_H^{formation} \times \Delta H^{formation}$$

where ΔH is the released heat per mole of hydrate formed in Joules, $H^H - H_w^{liq} \times X_w^H$ donates hydrate, liquid and mole fraction, dQ is the released heat in Joules, $K_{structure}$ is the heat conductivity in $\frac{J}{s \times m \times K}$ where subscript structure denotes soil, hydrate and fluid. $A,\ \Delta T$ are the cross sectional surface area in meter square and the temperature difference between the ends in Kelvin while $n_H^{formation}$ is the formation rate. The exact form of this is whether heat is dominating.

Two different types of nucleation are referred to in the literature, depending on the condition of the phases present. Homogeneous nucleation (HON) is a solidification process occurring in the absence of impurities. It involves many more molecules that could collide simultaneously, thus a sequence of bimolecular collision in which at least one of the products is also a reactant that is more likely to occur. Homogeneous from aqueous solution extracts both water and former from solution and might not be delayed much but is slow for other reasons (low concentrations of hydrate formers) and the free energy change can result to be negative.

Heterogeneous nucleation (HEN), on the other hand, occurs at the interface between two different phases, where impurities or surfaces are likely to be involved. The induction time starts by the formation of the first crystal nuclei, and concludes by the appearance of a detectable hydrate volume. Nucleation is a stochastic process, and may take only a few nanoseconds or up to several months, depending on the system. This time delay is caused by:

- Rearrangement of hydrate interfaces
- Rearrangement throughout the hydrate
- Effects of the solid surface
- For the HEN case presence of a hydrate film at the interface between the two phases will also increase the (macroscopic) induction time.

Considering free energy it is less likely to grow a hydrate nucleus in a free volume of gas and water than in the presence of micro-particles or a surface. The complete removal of micro particles from a solution is a rather difficult task, in practice, heterogeneous nucleation is more commonly observed.

Experimental results (Long 1996) appear to indicate that hydrate growth is initiated most frequently at the water-gas interface shown in Figure 4-3. This makes sense when considering the fact that the concentration of both constituents is higher here than elsewhere. According to Chaplin (Chaplin 2008) nano-sized clusters of water will occur within about 250 nm of the interface where small gas molecules will bond to these surface clusters because of several van der Waals interactions. In a CH_4 and water system the nucleation usually occurs on the gas side of the interface because of the high amount of gas that is needed (15%). Such high concentrations are usually not found dissolved in water. Additionally, Gibbs free energy of nucleation is lower here.

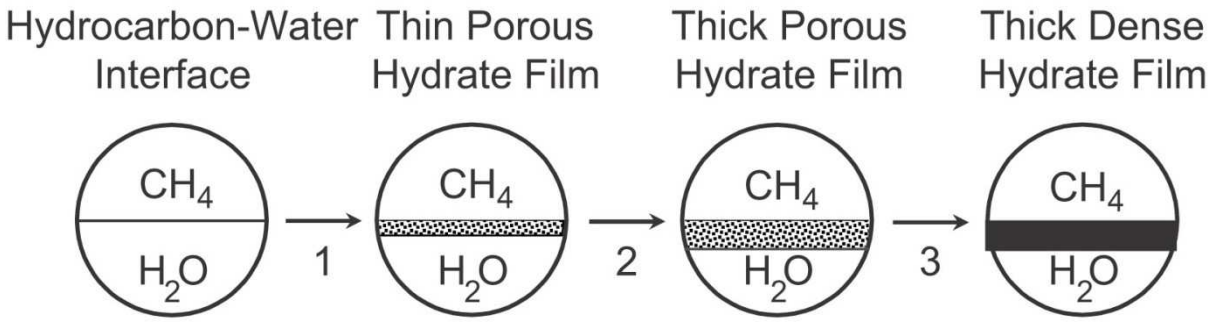

Figure 4-3: ***Hydrate growth is more likely to occur at the interface between gas and water, where both constituents can easily be accessed (Taylor, Miller et al. 2007).***

Figure 4-3 illustrates the phenomena of hydrate growth to most likely occur at the interface between gas and water. Point 1 in the figure shows a thin and porous film that forms and grows into the water phase in point 2. The end result is a thick and dense hydrate film.

Results from simulations on molecular level support this as well, and it is often explained by the significant concentration gradient at the interface with subsequent decrease in Gibbs free energy of nucleation. Once the growth period has initiated hydrate growth occurs very rapidly, and gas is being concentrated in hydrate cavities where the density of gas molecules actually is higher than in the gas phase. With time the consumption rate will decrease, as shown in Figure 4-1, and eventually the consumption rate may stop, due to lack of either gas or water molecules as in the case of experiments. In industrial perspective, there might be situations where new gas and new water is constantly supplied, like in a pipeline transporting water plus hydrocarbon from a reservoir to platform.

4.1.1 Hypotheses on hydrate nucleation

Several different hypotheses have been presented on nucleation, whereas three different theories are mainly considered in state-of-the-art literature. The only way to verify either one of these theories is through experimental work, stochastic and microscopic nature of nucleation makes it a very challenging task.

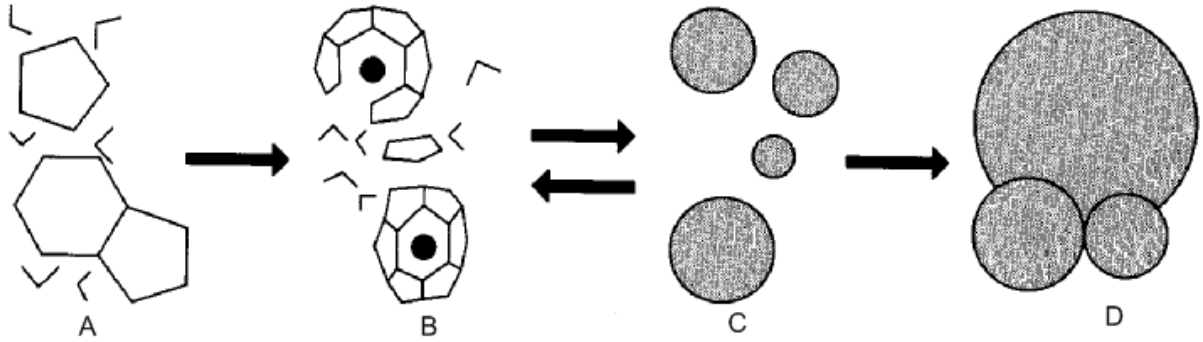

Figure 4-4: ***Labile cluster nucleation hypothesis (Sloan and Koh 2008). A) Clustered structures of water with no guest molecules encapsulated in the clusters. B) Guest molecules are surrounded by labile clusters of water forming different unit cells. C) Agglomeration of labile clusters. D) Critical radius has been reached and steady growth commenced.***

Figure 4-4 illustrates the labile cluster nucleation hypothesis by (Sloan and Koh 2008) where pure water occurs in clustered structures but without guest molecules occupying the cavities (A). Dissolved guest molecules will be surrounded by labile clusters of water which combine to form different unit cells (B). Depending on the amount of water molecules available, different polyhedra will form. Some labile clusters will agglomerate by sharing faces and thereby increasing the disorder (C). Once the critical radius has been reached steady growth will commence (D).

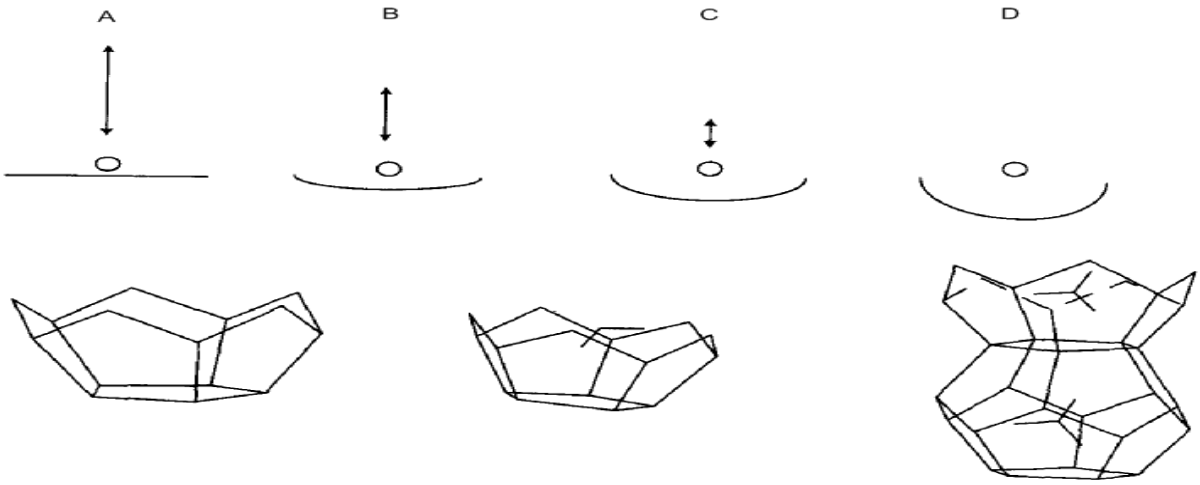

Figure 4-5: ***Visualization of nucleation at the interface hypothesis (Long 1994). A) Gas molecule is transported to the gas/water interface. B) The gas molecule migrates to suitable adsorption location. C) The gas molecule will be encaged in first partial then complete cages. D) Labile clusters agglomerate and start growing on the vapor side.***

Figure 4-5 illustrates nucleation at the interface hypothesis suggested by both Long and Kvamme (Long 1996; Kvamme 2000). Another theory is the nucleation at the interface hypothesis suggested by both Long and Kvamme (Long 1996; Kvamme 2000). This hypothesis has been slightly modified in later publications (Kvamme *2002 b*), and is illustrated by Figure 4-5. According to this theory, gas molecules are transported to the interface between water and gas (A), where the gas adsorbs on the aqueous surface. The gas will then migrate to a suitable location for adsorption through surface diffusion (B), whereby the water molecules will form first partial and then complete cages around the adsorbed gas molecules (C). Labile clusters will start agglomerating and growing on the vapor side of the interface (D) until a critical size has been reached. The hydrate growth on the gas side of the interface has been estimated to be two magnitudes higher than on the water side (Kvamme 2002a) and the gas side of the interface will thus dominate the hydrate growth.

The third theory often referred to is the local structuring nucleation hypothesis, in which thermal fluctuations causes a group of guest molecules to be arranged locally in a configuration similar to the clathrate hydrate phase. Both large and small clusters are formed which reassembles the hydrate cages. These clusters may grow to form hydrate unit cells or agglomerations of such, or they may shrink and dissipate. Once critical size of the hydrate cluster has been reached secondary nucleation and rapid hydrate crystal growth may occur. Nucleation is a stochastic process and considered unpredictable, which is illustrated by the fact that three slightly different hypothesis exist. During nucleation there are many unknown

mechanisms involved in the hydrate formation process, and without experimental studies it is hard to verify these theoretical models. This applies for hydrate growth also, where several different hypotheses exist.

In order to enable the growth of the nuclei, a continuous supply of water and gas molecules must reach the crystal surface, where these undergo a phase change, liberating a certain amount of energy, the heat of hydrate formation. If this energy is not effectively removed from the vicinity of the crystal, a local temperature rise will occur, reducing the driving force for further growth and favoring hydrate decomposition. Similarly, if the liquid is not saturated with the gas and/or the transport rate of gas molecules to the vicinity of the crystal is not sufficiently large, a local drop in the gas concentration will develop, which poses an unfavorable environment for further growth (Makogon 1997; Sloan 1998).

Hydrate formation kinetics is complex and poorly understood, partly because the crystal growth process is random. The hydrate crystal growth rate is controlled by diffusion from the bulk concentration to the crystal (equilibrium) interface and by the reaction rate at the crystal interface itself. Two major work for hydrate growth exits, the work by Englezos et. al. (Englezos, Kalogerakis et al. 1987) and the modified Englezos model by Skovborg and Rasmussen (Skovborg and Rasmussen 1994). According to this model, the change in the rate of crystal growth is given by:

$$\frac{dm}{dt} = KA\left(c - c_{eq}\right) \tag{4-5}$$

A is the crystal surface area, c and c_{eq} the concentration and equilibrium concentration respectively. K is an overall transfer coefficient expressed in terms of diffusion and reaction coefficients k_d and k_r as:

$$\frac{1}{k} = \frac{1}{k_d} + \frac{1}{k_r} \tag{4-6}$$

The concentrations in Equation (4-5) are sometimes replaced by fugacities as in the Englezos model. The replacement is made by assuming ideal liquid solutions, conservation of mass and constant temperature and pressure.

4.1.2 Analysis of equilibrium relations of CO_2 and methane hydrates

In natural gas mixtures, the small amounts of CO_2 present in CH_4 can cause hydrate sI to form; an example shown in Appendix C- 3 (result have been estimated using CSMHYD(Sloan 1998). This software is here used to predict the equilibrium pressure of CO_2 and CH_4 gas mixture. The phenomenon can be explained by comparing the sizes of both CH_4 and CO_2 that form sI hydrates. Their difference is CH_4 can occupy both the small and large cages, while CO_2 molecules occupy only the large cage $5^{12}6^2$. When sI is formed with a mixed gas of CH_4 and CO_2 the two gases compete with each other for better occupancy. With low temperatures and high pressures both CH_4 and CO_2 hydrates can be stable, nevertheless Sloan and Co-workers (Sloan 1998) in their experimental studies suggest that CH_4 hydrates have a higher equilibrium pressure than that of CO_2 hydrates for different temperatures. Good agreement of the equilibrium conditions for CH_4 and CO_2 hydrate in a P-T diagram is shown in Figure 2-4 and Figure 2-5.

4.1.3 Phase Field Theory

The objective of this work was to gain understanding of gas hydrate formation, and provide information to help evaluate hydrate related processes, such as CO_2 hydrate formation in methane hydrates in deep sea sediments. The composition and dissociation behavior of methane + carbon dioxide structure I binary gas hydrates were determined using Phase Field Theory. In their work (Svandal, Kvamme et al. 2006) describe two-component growth and dissociation of CO_2 and methane hydrates and the formation of carbon dioxide hydrate in aqueous solutions using Phase Field Theory. A similar approach has been applied here to model the growth of carbon dioxide and methane hydrate and the exchange process. Given the complexity of these models and the corresponding long simulations involved in integration of the governing differential equations only a limited only an example of how the Phase Field Theory can be used in a two-component simulation is given in the context of this MSc thesis.
. Only a short review of the model will be given here. Full details of the derivation and numerical methods can be found elsewhere (Svandal, Kvamme et al. 2006). The solidification of hydrate is described in terms of the scalar phase field φ and the local solute concentration c. The field φ is a structural order parameter assuming values $\varphi = 0$ and 1 for solid and liquid

respectively. Intermediate values correspond to the interface between the two phases. The starting point for the Phase Field Theory is a free energy functional:

$$F = \int dr^3 \left[\frac{1}{2}\varepsilon^2 T|\nabla\phi|^2 + f(\phi, c)\right] \tag{4-7}$$

where the integration is over the system volume, ε a constant parameter, T is the temperature. The gradient term ∇ is a correction to the local free energy density $f(\phi, c)$ assumed to have the form:

$$f(\phi, c) = \omega T_g(\phi) + [1 - p(\phi)]f_s(c) + p(\phi)f_l\,(c) \tag{4-8}$$

where the "double well" and "interpolation" functions are taken to be the following polynomials: $g(\phi) = 0.25\phi^2(1-\phi)^2$ and $p(\phi) = \phi^3(10 - 15\phi + 6\phi^2)$ required for thermodynamically consistent formulation of the theory. It was noted that $p(0) = 0\ and\ p(1) = 1$. This function was derived from density functional theory studies of binary alloys and has been adopted also for this system of hydrate phase transitions. Model parameters ω and ε can be related to measurable quantities.

The equilibrium conditions can be expressed in terms of the interfacial Gibbs free energy γ and the interface thickness d. The actual relationships are derived and discussed in detail elsewhere (Cahn and Hilliard 1958). To ensure minimization of the Gibbs free energy and conservation of mass, the governing differential equations following from equations (4-7) can be written as:

$$\dot{\phi} = -M_\phi \frac{\delta F}{\delta \phi} \tag{4-9}$$

$$\dot{c} = \nabla.\left(M_c \nabla \frac{\delta F}{\delta c}\right) \tag{4-10}$$

where M_c and M_ϕ are mobilities associated with coarse-grained equation of motion, which are related to their microscopic counterparts. Equation (4-10) can be viewed as a rigorous form of Fick's law and the mobility is expected to be close to the diffusivity coeffisient. Similar for the Phase Field mobility although this can be more complex since hydrate phase transitions involves coupled molecular rearrangements of water molecules. as such more detailed

investigations of this using molecular simulations might be advisable. In the simulations presented here the two mobilities are set equal.

The process by which matter moves from an area of high concentration to an area of low concentration is called diffusion. Diffusion can be represented for one dimensional flow by the classical Fick's first law:

$$\vec{J} = -D\frac{\partial c}{\partial x} \tag{4-11}$$

The Fick's second law is used to predict how diffusion causes the concentration to change with time as:

$$\frac{\partial c}{\partial t} = D\frac{\partial^2 c}{\partial x^2} \tag{4-12}$$

Where,

$\vec{J}$ = Flux is the rate of mass transfer over a unit area in a given time$\left(\frac{moles}{m^2 s}\right)$. The flux is what we are measuring when studying diffusion.

D = Diffusivity is the constant which describes how fast or slow an object diffuses$\left(\frac{m^2}{s}\right)$.

c = Concentration is the amount of mass in a given volume $\left(\frac{moles}{m^3}\right)$.

x = Refers to the distance that the object is diffusing (m)

t = time (s)

The symbol ∂ describes the distance between where the object starts and where it ended up after it diffused. Equation (4-11) is relevant for this work since the solution of this equation gives a proportionality of mass transport proportional to the square root of time. Practically this means that a plot of the phase transition front progress shows a linear tendency when plotted against square root of time the phase transition is likely be kinetically mass transport limited

4.1.4 Hydrate formation and dissociation in nature

Processes always take place in porous media, sedimentary rock structures. Understanding porous phenomenon is extremely difficult.

4.1.5 Porosity

Porosity is one of the most important rock properties in reservoir engineering. It determines the amount of fluid that a particular reservoir rock can hold. Since oil, water and gas occupy pore space in a reservoir rock, if one knows the porosity and the fluid saturations, the reserves of hydrocarbons can be calculated.

Porosity ϕ is defined as the ratio of the void space or the pore volume V_p in a rock divided by the bulk or total volume V_t of the rock.

$$\emptyset = \frac{V_p}{V_t} = \frac{V_t - V_m}{V_t} = 1 - \frac{V_m}{V_t} \times 100\% \tag{4-13}$$

The pore volume V_p is the difference of total volume V_t and volume of matrix or grain volume V_m. Porosity is a fraction and has dimension-less parameter but it can also be measured in percentage as in equation (4-13). Cementing materials may seal off some part of the pore volume in reservoir rocks (Figure 4-6) thus two different types of porosities results: effective porosity and total porosity. Effective porosity is the ratio of the interconnected void space in the rock to the bulk volume of the rock.

Total porosity is the ratio of the total void space in the rock to the bulk volume of the rock.

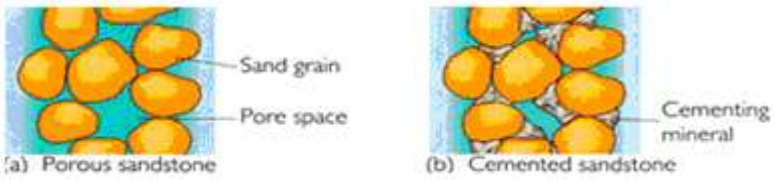

Figure 4-6: Basic porosity in sediment (www.beg.utexas.edu)

Porosity is factor that determines the fluid storage capacity in a reservoir. In petroleum reservoirs porosity, the reservoir size, and the fluid saturations (water/oil/gas) determines the reserves. The porosity of the Bentheim sample used in the experiments reported here was 22-24%

4.1.6 Saturation

A reservoir or core plug usually contains several fluids for example oil, water and gas. In these experiments no oil was present or in the pores. Saturation is fraction of the total pore volume V_p which contains the fluid.

Saturation can be written as:

$$S_w = \frac{V_w}{V_p},\ S_g = \frac{V_g}{V_p}\ and\ S_h = \frac{V_h}{V_p} \tag{4-14}$$

Where,

S_w, S_g and S_h is water, gas and hydrate saturation V_w, $V_g\ and\ V_h$ are water, gas and hydrate volumes respectively. A normal condition where the entire pore volume is filled with water, gas and hydrate is given:

$S_w + S_g + S_h = 1$. The experiments reported here had initial water saturations between 30-50%

4.1.7 Using resistivity measurements

Porous rocks are composed of an aggregate of mineral grains with between-lying cavities or pores. The solid (matrix) with the exception of some clay minerals are not electrically conductive. The electrical properties of rocks depend on the cavity geometry and the liquids that these are filled with. Oil and gas are not electrically conductive as compared to water with dissolved salts see for example (Lien 2004). Resistivity of a substance with length l and cross section A is defined as:

$$R = r\frac{A}{L} \tag{4-15}$$

where r is the total electric resistance measured in ohms (Ω). In terms of Ohms law, $r = V/I$.

where

R = resistivity (measured in ohm-meters, Ω m);

A = cross-sectional area (calculated in square meters, m²).

V = volts measured in volts

L = the length between electrode rings inside the sleeve (measured in meters, m).

I = current measured in Ampere (A).

The most fundamental size to describe the electrical properties of a porous rock is the so-called formation factor. This indicates the resistivity relationship between R_o of the rock when it is 100% filled with saline formation water (pore water), relative to resistivity of partially saturated rock with saline formation water R_w. Formation factor is defined as:

$$F = \frac{R_o}{R_w} \tag{4-16}$$

Where R_o and R_w are respectively, the resistivities of 100% saline formation saturated rock and partially saturated rock with the saline.

Archie's first law expresses the relationship between formation factor and porosity as:

$$\mathrm{F} = \frac{\mathrm{R_o}}{\mathrm{R_w}} = \mathrm{a}\emptyset^{-\mathrm{m}} \tag{4-17}$$

where a is a function of the turtuosity, and m is the cementation factor that reflects the relationship between the pores and pore neck, as well as the number of closed channels. The cementation factor can be determined empirically and varies from 1.3 for unconsolidated sand to 2.6 for compact limestone (Lien 2004).

Archie's second law uses water saturation for thus finding the resistivity index I for the sample as:

$$I = \frac{R_t}{R_o} = bS_w^{-n} \tag{4-18}$$

where I is called the saturation index, R_t is the formation resistivity and b is a function of the turtuosity. S_w is the saline saturation, and the exponent n, is Archie's saturation exponent usually close to 2. According to Archie (Archie 1947), resistivity is a function of the turtuosity and saturation of the fluid in place. Hydrate formation will increase the turtuosity and reduce the water saturation in the medium. This is why it is possible to acquire information about gas hydrate concentration through resistivity data. Figure 4-7 shows a logarithmic plot of a large amount of resistivity index measurement data. The best customization to the data was obtained with n = 2.7

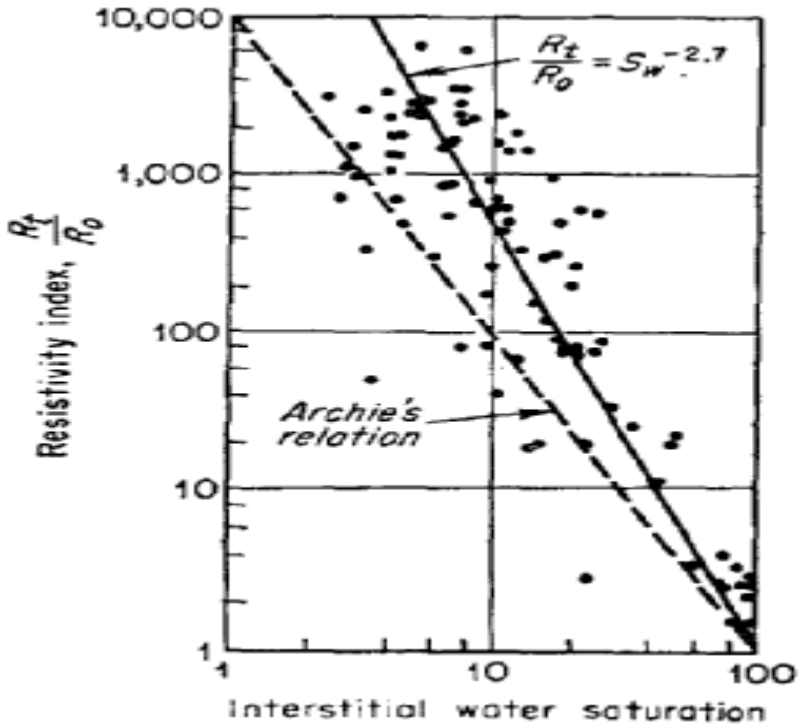

Figure 4-7: Resistivity index I as a function of water S_w (Lien 2004)

In the work of Yongjun and co-workers (Yongjun, Weidong et al. 2008), resistivity of their system rapidly decreased when hydrate was formed, and then increased to a higher value after hydrate formation. The resistivity increment was observed when sand stones were cooled down for hydrate formation, (lower temperature, and lower conductivity of the brine water in the pores). Finally, the resistivity of the system is higher than that before hydrate formation when free gas was present. This may be explained by the "blocking" mechanism of gas and hydrate as shown in Figure 4-8.

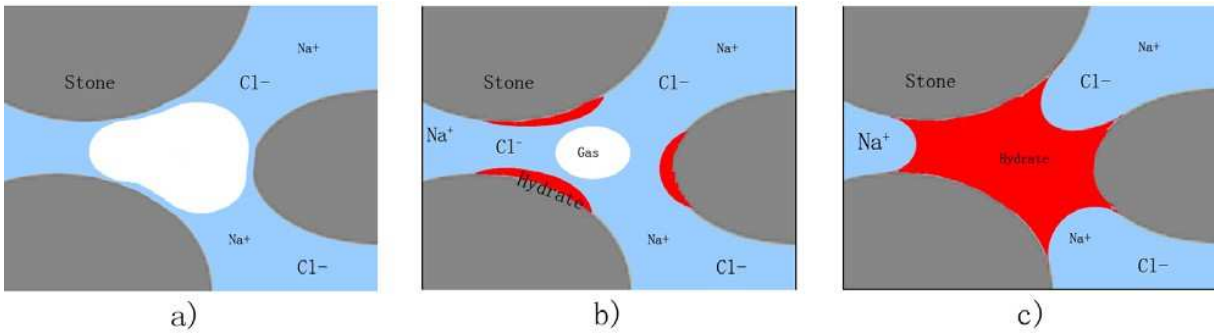

Figure 4-8: **Schematic diagram for the hydrate "blocking" mechanism during hydrate formation on affecting the resistivity of porous media saturated with brine water (Yongjun, Weidong et al. 2008).**

Before hydrate formation (Fig 4-8a), large bubbles of free gas are present in the pores, which may block the conductive water to a certain extent, but for water wetted sands there could be a thin adsorbed water layer around the sand surface connecting the brine water in the pores.

During hydrate formation, gas bubbles became smaller and smaller and may disappear completely (Fig 4-8b), and hydrate crystals formed and accumulated on sand surfaces. To some extent, the blockage of pore water may be released due to smaller gas bubbles before large hydrate crystals were formed, therefore the resistivity of the system was decreased as observed in Figure 5-5, Figure 5-6 and Figure 5-7. After massive hydrate formation, the throats of the porous media could be completed blocked by hydrates, which can be strongly bonded on the sand surface as shown in Fig 4-8c. Consequently, the presence of hydrates will increase the resistivity of porous media, and the higher of the hydrate saturation, the higher of the resistivity.

5 Experimental

This chapter outlines two experimental studies. The primary aim of these efforts, done in collaboration with the Reservoir Physics Department of the University of Bergen, was to design, complete and test experimental setups to run laboratory-scale experiments. Resistivity measurements were used to detect relative amounts of different phases in the system. Among important applications for these setups hydrate formation in porous media and production studies of methane from methane hydrate using carbon dioxide injection. A great deal of time is required to design and complete an experimental setup, it is time consuming to order parts, fit them, complete the setup and run a test.

The secondary goal of the first experiment was to study the variation of electrical resistivity during hydrate formation in porous media. This experiment emphasized characterization of hydrate induction and growth by methane consumption data and measurements of electrical resistivity during hydrate formation. Another set of experiments was related to studies of methane release from methane hydrate through injection of liquid carbon dioxide in porous media. The main objective was to form methane hydrates in porous medium and then produce methane from its hydrates during carbon dioxide injection.

As part of this thesis, two experimental setups have tested and completed under the guidance of postdoc Geir Esland who designed the apparatus. MSc Jonas Odland and I were responsible for cutting, filing, bending and screwing up of pipes fittings to their exact form. Different types of valves from T-valves to bent valves were used in the connections which enabled us to shut off or open the system's connections in the different labels marked in Figure 5-2 and Figure 5-9. The equipment was tested for gas and water leakage prior to commencing the experiments (main responsible I and Jonas Odland). Several of the connections and valves appeared to have substantial leakage and had to be replaced and repaired. The setup connections and testing took a lot of time in the completion of these experiments. Another delay to complete the setup was to order parts from companies and fixing of equipment errors at the University workshop. The whole process for the designing, completing and testing of the two experimental setups in this thesis lasted for about 8 months.

5.1.1 Experimental layout description for experiment I and II

Figure 5-2 shows the schematics of the cylindrical cooling jacket apparatus used to measure resistance inside a core plug during and after hydrate formation. Figure 5-9 shows basic design of the apparatus used for the study of methane production during carbon dioxide injection in porous media. The main difference between the two experimental setups is the first setup has only one methane Isco pump and a methane cylinder while the second setup has two methane Isco pumps and two cylinder pumps. The two cylinders and Isco pumps were used in delivery of methane and carbon dioxide to the Isco pumps. On the other hand, the first setup has a sleeve that was fixed in the core holder as shown in Figure 5-3. The Isco pumps were then used in these experiments to deliver gas into the system by regulating pressure and by accurately controlling gas volumes and flow rates. The computer shown in both setups was used for logging that is, the flow rates; pressure, time and volume of methane gas accumulated were recorded from the Isco pumps. Following is safety/relief valve used in case of gas choke. The refrigirated bath contained anti-freezing water that circulates through the entire system. One bath was connected to the two setups. Two "Hozelock Dual Tap Connector" was used to control water flow. The layout pours cool water between the core holder and a "cooling jacket. Refrigerated liquid circulates around the bar of the confining fluid, cooling the rock and the system.

The confining pressure pumps illustrated in the two setups were used to seal the system and hold all the flow of the fluids in place inside the rock pore species. This is why the confining pressure should be higher than the pore pressure. The pumps of the type Haskel MS-188 and Haskel MS-188 were used in these experiments. High viscous oil was used as confining fluid to prevent leakage into the core sample due to pressure differences. Installing Haskel pumps are very delicate since constant pressure would be hard to keep. As with these experiments, there has always been a pressure difference. This was discovered to be due to a leak in the intake air instead of oil by the pump. The temperature of the surface of the core plug was manually controlled by thermal links and Multi Logs thermometers. The experimental pore pressure was set to 83.7 bars and the system was left for days before it was cooled to $4^{o}C$ which was expected within the thermodynamic conditions for the formation of methane hydrate.

5.1.2 Filling fraction for experiment I and II

Small cages comprises of 2 cavities while the large cages consist of 6 cavities together they held 46 water molecules to form structure I hydrate (Sloan and Koh 2008). This is equivalent to 5.75 water molecule per gas molecule. According to Sloan (Sloan 1998), typical occupancies of large and small cavities are 50% and 95%, respectively (Section 2.1.1.).

Considering cage filling, the relationship of how many moles of water that was present in the beginning and how many moles of methane that was consumed was calculated based on gas densities found by UniSim Design R380 (Honeywell). There will always be some free water again after the end of hydrate formation (depending on salinity and a few other factors). This may to some extent monitored with the MRI in the U.S., but here in Bergen, we have no opportunity to observe this. So we may assume full conversion. Table 5-1 shows the filling fractions for some of the experiments done in this thesis.

Table 5-1: Filling fraction for experiment I and II

	Methane in hydrate (mol)	Water in hydrate (mol)	Estimated filling fraction
Experiment I: 1 wt% NaCl	0.17	1.84	0.52
Experiment I: 3 wt% NaCl	0.21	1.54	0.78
Experiment II: 5 wt% NaCl	0.13	0.87	0.83

5.2 Experiment I: Resistivity measurement in porous media

In the oil and gas industry, many well-logging methods are today used for the exploration of hydrate resources; these include acoustics, resistivity, NMR, Gamma ray and density neutron, which have been used in logging while drilling (LWD) for hydrate exploration. For the purpose of this thesis, resistivity has been studied in Bentheim sandstones. Yongjun et al 2008 (Yongjun, Weidong et al. 2008), gas hydrate can have a great impact on electrical properties of the matrix, such as resistivity, which has been considered as the most effective parameter for characterizing hydrate bearing matrix. Therefore, resistivity studies in natural gas hydrates are important in the development of gas hydrate resources. The reason according to Youngjun

is solid hydrates will fill the voids of the matrix formed by sand grains and change their cementation condition, which have a great impact on the resistance of the sand matrix (see Figure 4-8). In this study, experiments have been conducted to study the resistance in Bentheim sandstones in order to correlate resistivity in porous media. The effects of hydrate on the resistivity of hydrate bearing sand matrix has been reported. The data generated is preliminary but promising and the experiments can be repeated. If the results were not preliminary, the data could be used in well logging to determine hydrate saturation and other properties of hydrate bearing formations.

5.2.1 Material used to measure resistivity

A confining pressure pump 9 was used to measure the system confining pressure. The flow rates, pressure, time and volume of methane gas accumulated were recorded by a series D Teledyne Isco Syringe pump 2 (100 DM and 260 D) (Figure 5-2). The Teledyne Isco Syringe Pump was used in these experiments to deliver gas into the system by regulating pressure and by accurately controlling gas volumes and flow rates. Methane gas (99.99%) was obtained from HYDRO Gas Company Norway. The distilled water was used to prepare brine solutions. Winter Ban anti freezing water up to -73.3 ^{o}C was used in the bath as it circulates through the entire system. A liquid leak detector, a Swagelok product was used to detect leakage from tubes, fittings and valves. Aceton was used to clean up pumps and valves. The LCR-meter of type Hewlett Packard 4262A apparatus was used in this experimental work to measure resistance. Lots of efforts were taken in designing completing and testing of the experimental apparatus. The apparatus setup is located at the University of Bergen. Figure 5-1 illustrates an overview of the components used for the setup while the schematic is shown in Figure 5-2. Figure 5-3 and Figure 5-4 shows the core holder schematics.

5.2.2 Procedure and problems encountered to measure resistivity

Laboratory experimental setup shown in Figure 5-2 was designed and used to measure resistance and study the kinetics of resistivity during hydrate formation in porous media. This experiment set-up was built at the University's work shop, and the first test results are reported in this thesis. The results are promising but preliminary. A lot of care has been taken to prepare the sample and procedure described below.

Prior to the experiments, the resistivity cell was washed with distilled water and dried. The core sample length, weight and diameter were measured. Lengths and diameters of the samples were kept constant and salinity content was the only varying parameter. The brine was prepared using sodium chloride (NaCl). With the brine in a beaker, the core samples were saturated by spontaneous imbibitions where the saturation was kept around 50%. The saturation was found based on mass balance. Appendix A- 1 essentially illustrates core sample parameters for the three cases finally measured for resistivity studies.

Significant challenges were met in the installation of the core holder as some modifications to design were conducted. The setup was installed as part of this task and has brought challenges in the form of leaks and lack of equipments. The core holder was provided with an adjustable end piece which was proven to be a weak joint where leakage was easily encountered. The adjustable end piece pipe was connected to a tube with a length too short to press the core into the sleeve and this was therefore replaced with a longer one (see Figure 5-4). The wires from the socket to measure the outlets in the core holder were also extended. A LCR-meter of type Hewlett Packard 4262A was connected to measure the outlet. Although this was an older model, no software was available for logging. Logging was therefore done manually. This required personal presence especially during hydrate formation. The core holder was wrapped in insulating material to reduce supply of heat to the system.

The core sample was then placed in the holster. The adjustable end piece was drawn through core holder and into the sleeve (Figure 5-4). End pieces were affected when the core sample on both sides and sleeve was pressed into the core holder, before the pieces were assembled. The different electrodes were then connected to measure the current flow, voltage and resistance through the system (Figure 5-3). This was done as shown in Figure 5-3 by connecting electrodes via low current (A) and high current (B') from the LCR-meter through A and B' on the opposite sides of the core holder. A' and B electrodes from the LCR-meter

were also connected to A' and B on the core holder to measure the voltage of the plug inside the rubber sleeve. Figure 5-3 was specially designed for four electrical electrode resistivity measurements. Because of the current routing, gas was not injected on both sides of the core plug. This would have led to contact between the positive and negative terminals through the pipelines, and resistivity measurements would not have been possible. Current was discharged through the end pieces in order to measure the resistance between the metal rings as a result of hydrate formation. In order to prevent the flow between the rings and the core, the rings were designed with a plastic tape which isolated the outer diameter of the core. The surfaces consisted of end pieces of silver to improve the conductivity.

The following steps were then conducted to pressurize and cool the system:

- The confinement pressure set to 400 psig. Methane gas introduced into the system at about 100 psig (confining pressure must be greater than core pressure to seal the system). The methane gas cylinder was further used to increase the core pressure.
- The core and confinement pressure was simultaneously increased to 1200 psig and 1500 psig, respectively.
- After hours or days with no sign of leakage, the system was cooled to experimental temperature ($4^{o}C$) allowing hydrates to form.

Due to lack of computer programs to record the resistance measurements, the data such as time, temperature and resistance were manually sampled. This required personal presence throughout the resistivity experiments, especially during hydrate formation where the trend of logging resistivity development was important. After the resistance had been manually recorded, the resistivity was calculated using equation (4-15). The manually collected data and automatically sampled data from the pump was then systemized and plotted. The resistivity curves generated from these sampled data indicated that there could be some weaknesses with the experimental setup and also potential problems of leakage.

5.2.3 Experimental design I

The experimental layout and description for experimental design I/ setup 1 is explained in section 5.1.1.

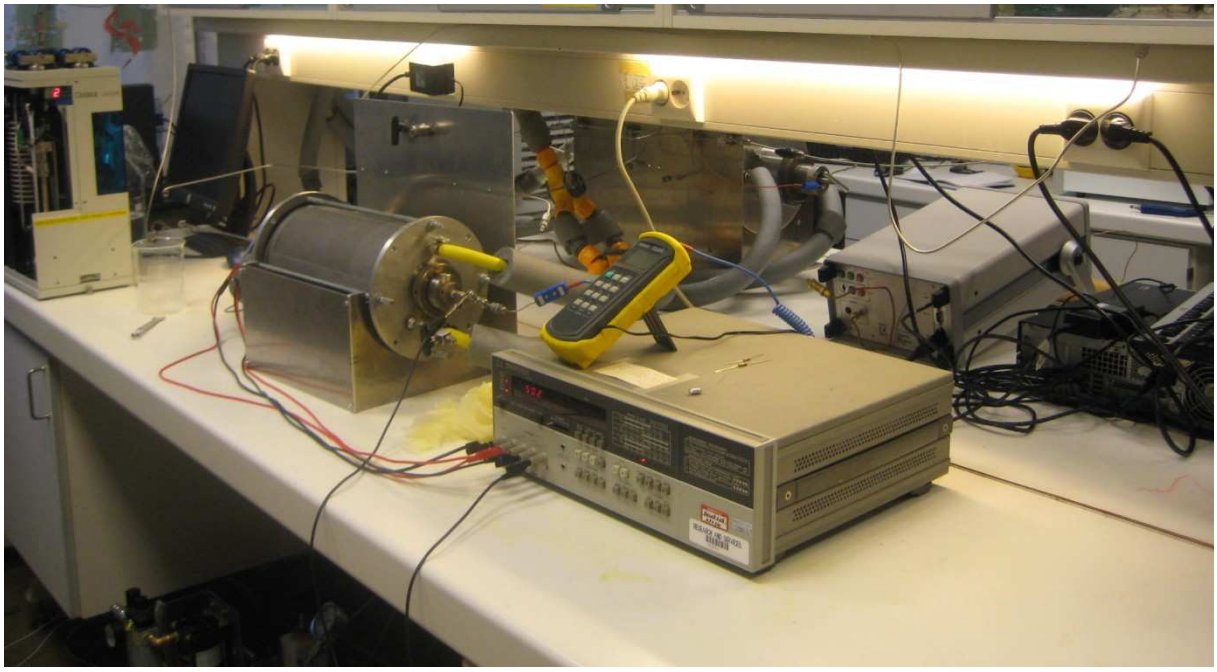

Figure 5-1: Apparatus used to study resistivity in porous media (Schematic shown in Figure 5-2)

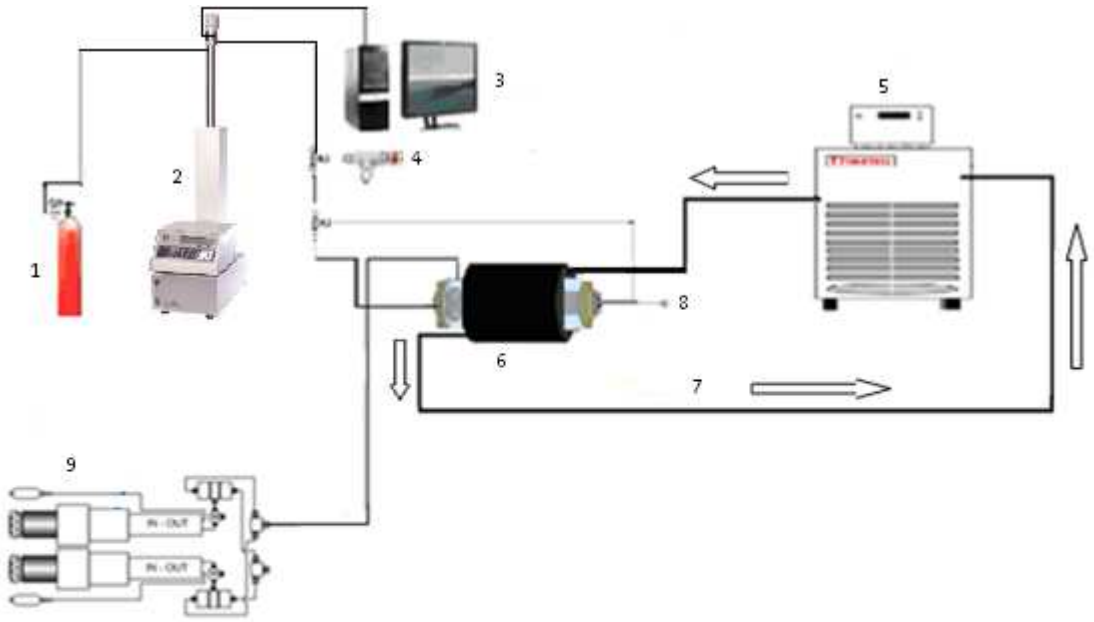

1	CH_4 cylinder	6	Cooling jacket
2	CH_4 pump	7	Circulating antifreezing liquid
3	Computer used for logging	8	Thermometer
4	Relief valve	9	Confining pressure pump
5	Refrigerated bath		

Figure 5-2: The schematics of the cylindrical cooling jacket apparatus used to measure resistance inside a core plug during and after hydrate formation.

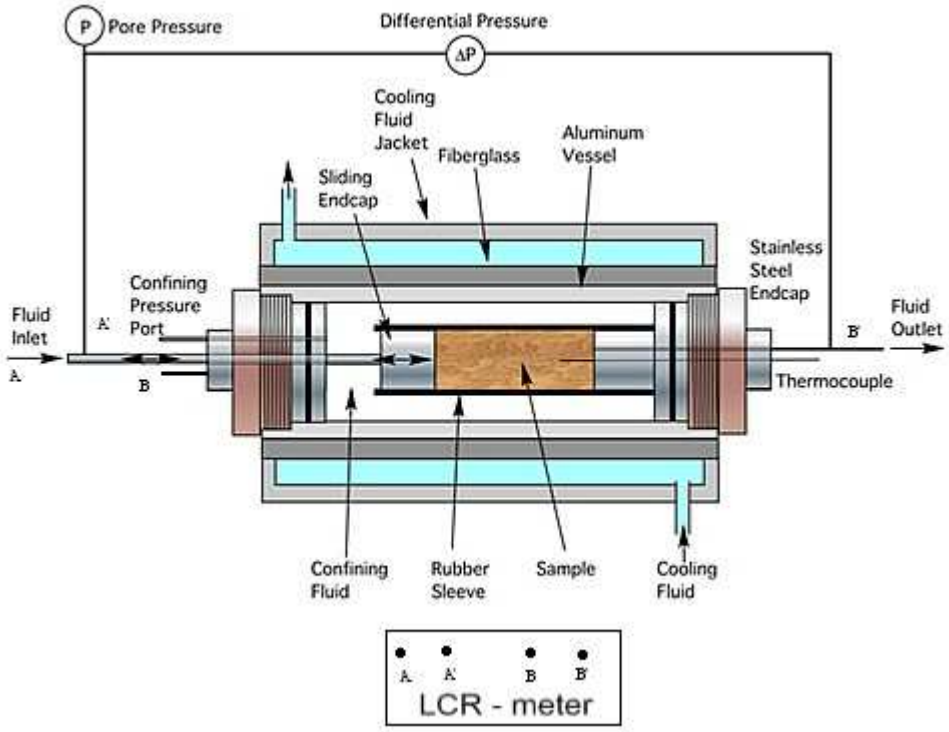

Figure 5-3: Cross section of high pressure core holder with an LCR - meter modified from (Seol, Kneafsey et al. 2006).

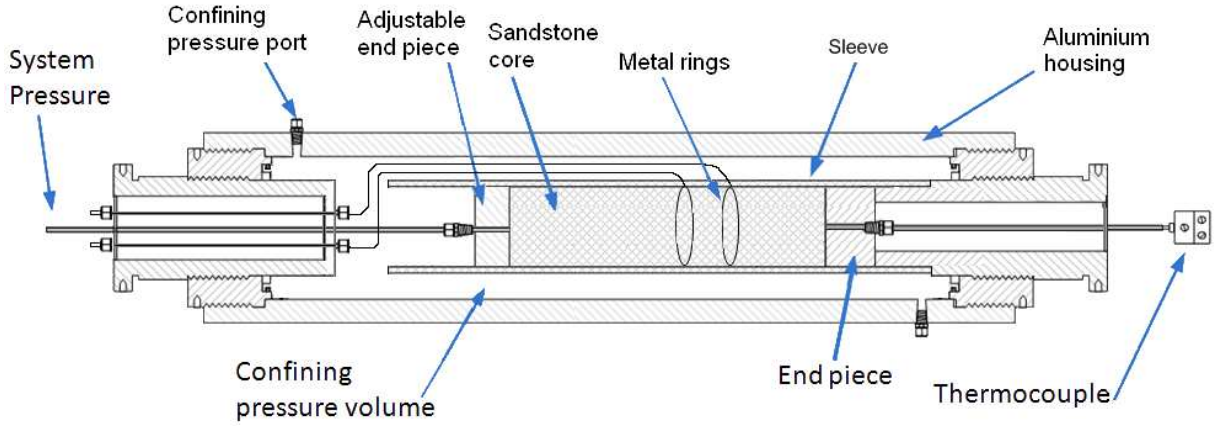

Figure 5-4: Illustration of the core holder used in the resistivity measurement (Odland 2009).

Figure 5-3 illustrates the 4 electrode technique used to measure resistance in fluid filled in porous media in laboratories. The main difference between the two experimental setups (Figure 5-2 and Figure 5-9) was a sleeve that was fixed in the core holder of Figure 5-2. Figure 5-4 shows the rubber sleeve which was built with two electrode rings inside the sleeve.

5.2.4 Results and Discussion

Resistivity with core samples saturated with NaCl brine solution has been studied at 1 kHz with 1200 psig pressure and temperatures down to 3°C. The salinity content was respectively 1, 3, and 5 wt% NaCl. All core samples exhibited a typical behavior shown in Figure 5-5, Figure 5-6 and Figure 5-7. The graphs does not follow the expected pattern according to the theory and previous work in the sense that lower salinity increases hydrate stability and increases formation rates. Lower salinity should also result in lower residual water saturation. Variation of methane consumed by at the end of hydrate formation in the core sample of Figure 5-6 was believed to be the result of the system's temperature sensitivity and variation in the confining pressure. Considering the development around this work for all three resistivity experiments the initiation of hydrate formation was verified. In general, the resistivities of the samples decreased sharply between 11°C to 4°C during cooling. The rate of decrease slows down considerably beyond this temperature and then an increase in resistivity was noticeable due to hydrate formation. Reason can be explained from solid hydrate formation blocking the pores of the sand stone resulting in low temperature and lower conductivity of the brine water in the pores. Note that resistivity was calculated using equation (4-15). The cross sectional area, length of electrode rings and resistance were the experimental measured parameters.

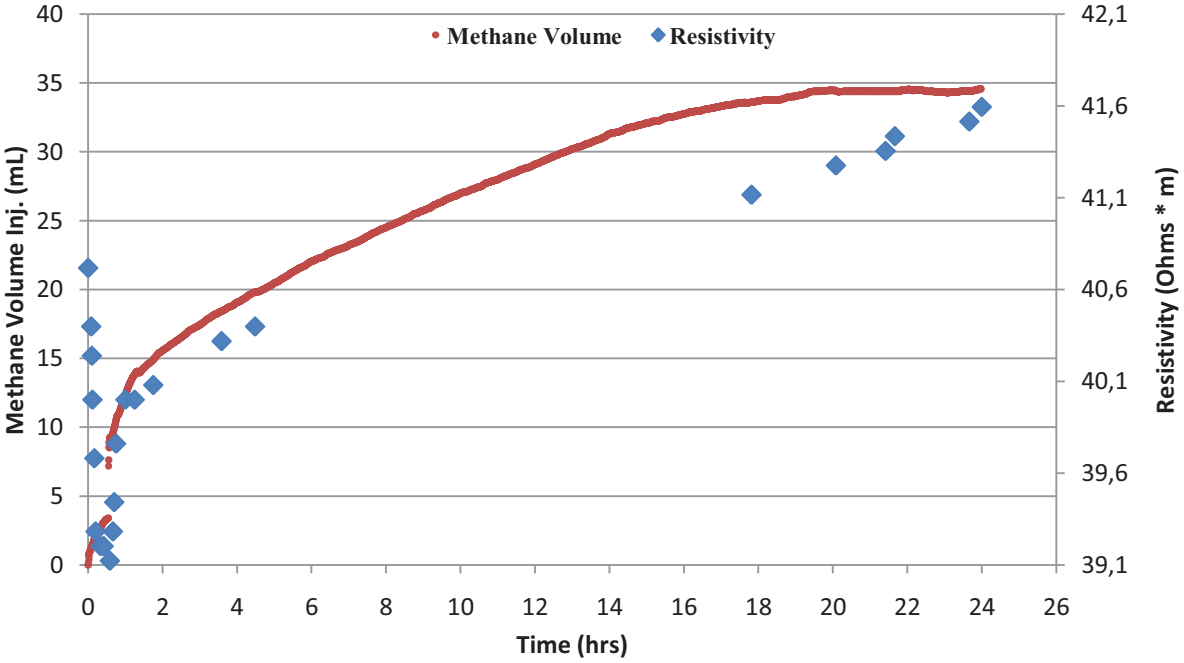

Figure 5-5: Methane and resistivity measurement with 1wt% NaCl

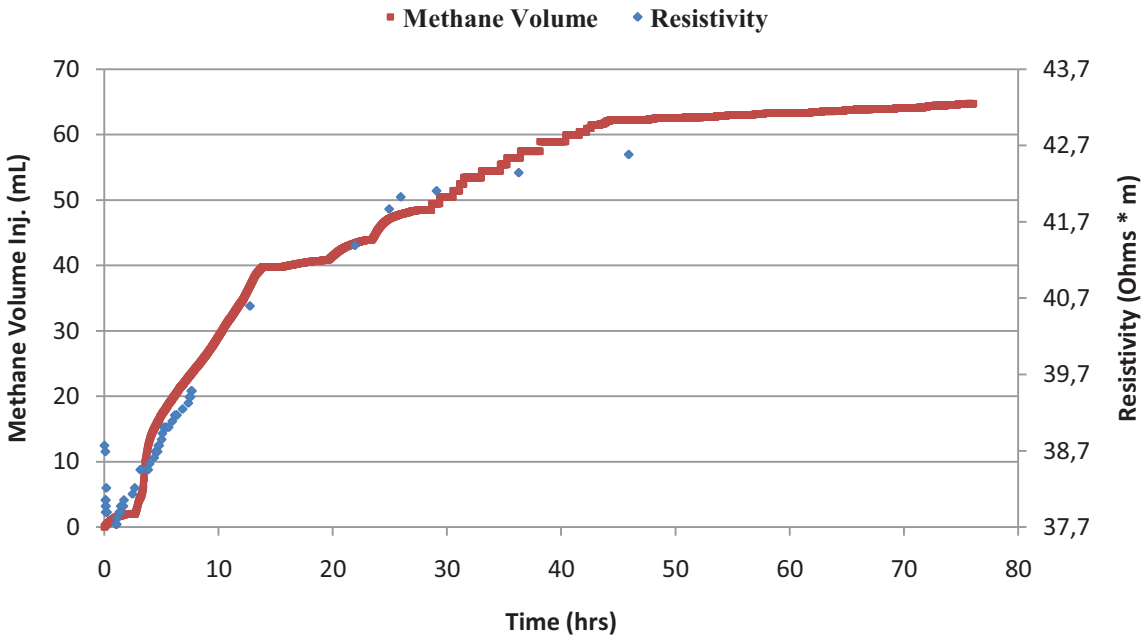

Figure 5-6: Methane resistivity measurement with 3wt% NaCl

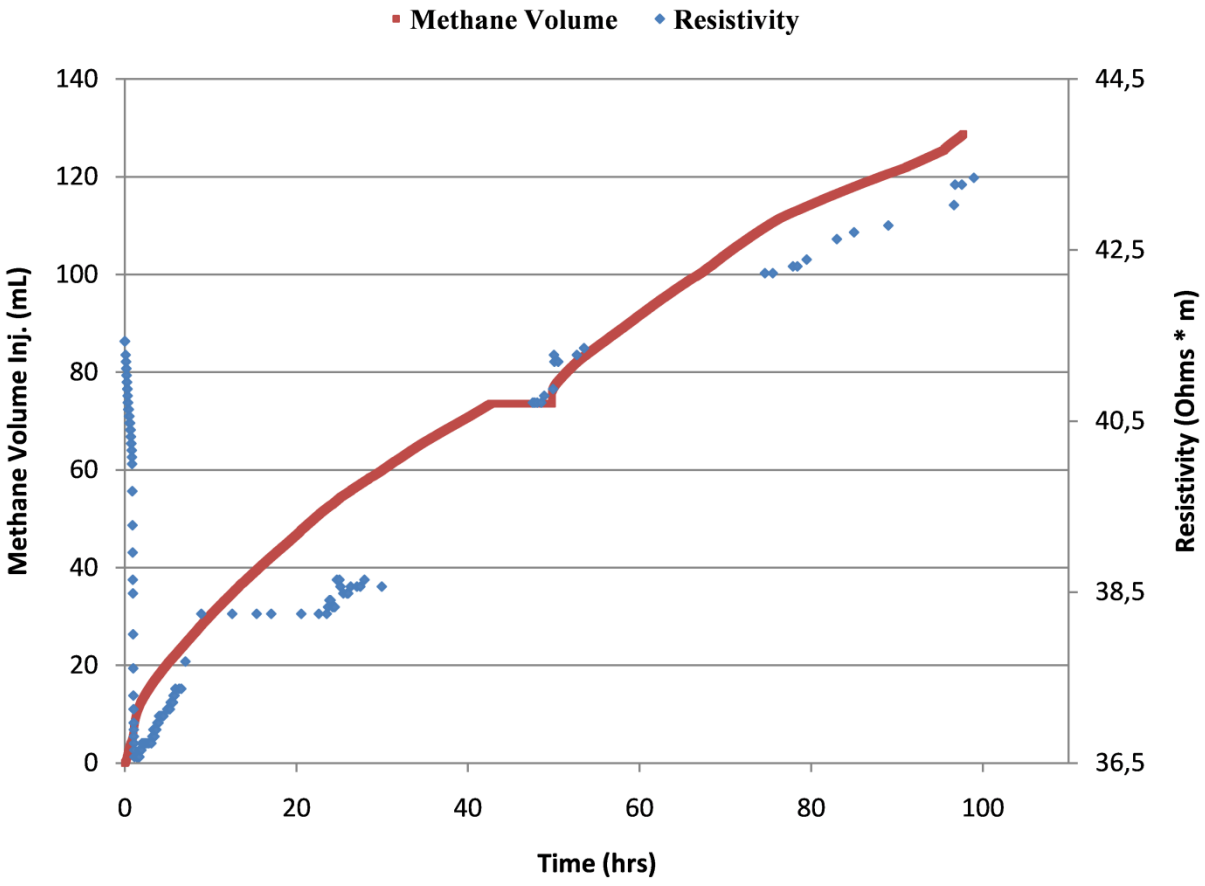

Figure 5-7: Methane and resistivity measurement with 5wt% NaCl

Figure 5-5 shows the simultaneous increase in resistivity with increasing cumulative amount of methane injected. The NaCl content was 1wt% during the methane consumption and resistivity studies. The increased resistivity of the formation is a result of hydrate formation. It shows resistivity development under depressurization, induction time, and the initiation of hydrate growth. Hydrate formation started at 10 ^{o}C. Most likely, the system was then in the metastable zone for hydrate growth where the driving forces is small. Shortly after the hydrate formation was initiated the resistivity increased. Hydrate was then in large quantities to block the roads for the current to flow through, and resistivity increased. In Figure 5-6, the NaCl content was 3wt% during the methane consumption and resistivity studies. The accumulated methane curve showed a formation curve at given time interval which indicates hydrate formation becoming more dominant for the current to pass through the pores of the core. Figure 5-7 corresponds to 5 wt% NaCl brine during methane consumption and resistivity studies. The resistivity curves showed some gaps due to manual registration.

From the three experiments, it was observed that formation of hydrates in rocks will fill/block the pores of the matrix of sand grains. This will have a substantial impact on the resistance of the sand matrix. Variations of hydrate formation from aqueous solutions of different salinities were another objective of the studies. This is important for two main reasons. Hydrate formation from aqueous solution in porous media will lead to increased salinity of the remaining aqueous solution. The different experimental runs showed a clear tendency of decreased resistivity during hydrate formation with increased salinity content. The induction times were proportionally shorter with decreased salinity. The measured resistivity during hydrate formation decreases with increasing salinity concentration, indicating that high content of salts affects the formation considerably. It can be clearly seen in Figure 5-5 that observable hydrate formation was recorded after about one hour when the system was cooled to experimental temperature, as compared to the graphs in Figure 5-6 and Figure 5-7.

The Figure 5-6 and Figure 5-7 showed observable hydrate formation at about 2.5hrs and 5hrs respectively. In contrast to the three resistivity experiments, only Figure 5-6 seems to stabilize the final hydrate formation. Figure 5-5 and Figure 5-7 were terminated before stability was reached. This can be regarded as premature terminated experiment. The resistivity in Figure 5-6 decreased simultaneously with increasing methane consumption after cooling. Just around 2hrs, the growth of hydrate initiated and resistivity increased as a result of increased hydrate saturation. Consumption curve in Figure 5-7 shows a discontinuation of methane consumption

between 41-45 hours due to the refilling of methane in the pump volume. About 74 ml methane was refilled in the system at 8.37 MPa and 20 ^{o}C.

Figure 5-7 shows that resistivity was still increasing even after the hydrate formation was assessed to be accomplished. One possible reason for the high methane consumption is an undetected leak in the piping system and in injection pump. When the leakage rate is sufficiently large, greater amounts of methane would be required for pressure maintenance than actually consumed by the methane hydrate formation. The increase in resistivity is decreasing and the maximum resistivity falls within the same area as Figure 5-5 and Figure 5-6. This supports the theory of leakage in the pipes and or pump system. The length of the induction period has previously described an apparently stochastic nature. When this period began in these three trials, it was difficult to determine. But initiation observable of hydrate formation occurred after only one hour in all resistivity experiments. This is somewhat unrealistic for a system containing only the components of water and gas. Theory suggests that the presence of alternative hydrocarbon components will accelerate the hydrate formation (Sloan and Koh 2008). Leakage of confining fluid into the core sample through the adjustable end piece was widely believed. If the induction time was longer the temperature dependence of resistivity and the influence of increased salinity in the pores would have been known. Results presented here therefore provide no information about the reduction in resistivity during the induction period as a result of increased salinity in the pores.

Table 5-2: Resistivity values at chosen time point during hydrate formation at 1kHz.

Resistivity ±0.2 (Ω.m)	Figure 5-5: 1wt%	Figure 5-6. 3wt%	Figure 5-7: 5wt%
Initial	40.7	38.6	41.5
minimum	39.1	37.8	36.5
maximum	41.6	42.6	43.0

The formation rate was reduced when the pores were filled with hydrate and the tortuosity of the water phase increased with increasing hydrate pore fills. The magnitude for current flow throw the filled pores became smaller and smaller. This corroborates the previous results of (Saner, Cagatay et al. 1997). Although hydrate formation theoretically leads to increased resistivity, this will be highly dependent on where in the formation hydrate was formed. The hydrate formation blocks the pore spaces which are conductive at low salinity while those with higher salinity would therefore be more conductive. Due to lack of parameters in Archie's equation hydrate saturation was not calculated in this task.

In comparison to the values in Table 5-2 with values obtained from the work of (Yongjun, Weidong et al. 2008), where the resistivity varied from 1.21 to 3.82 Ω.m, there is a clear difference in magnitude for the measured resistivity. Maximum resistivity varied due to the length of the experiment, when the stability of resistance was not achieved. Initial resistivity was higher at 5 wt% salt content than the lower. Reasons for this can be explained from the leaks and other mechanical contributions to uncertainty with variation in the saturation distribution.

5.2.5 Uncertainties

The uncertainties considered were smaller contributions to the errors observed in this part of the thesis. The uncertainties of the slide gauge used in the initial stage measurements of length and diameter are in the order of ±0.02mm. The balance uncertainty used for the weight measurement is about ±0.01grams. The temperature uncertainties were considered to be ±0.1^{o}C. The readings of the LCR-meter uncertainties could be taken with an accuracy of ±0.01 Ohms. In this way the errors which arises from manual readings and those in the equipments slightly disrupts the experiments. Application of this on a sample - and interpretation involves significant errors due to non-ideal conduction paths (non-linear as well and non-uniform medium of solid, liquid, gas and hydrate).

5.2.6 Conclusions – Resistivity measurements

From the experiments on the monitoring of resistivity during hydrate formation in the presence of salinity, an experimental setup for laboratory resistivity measurement has been installed and hydrate formation was confirmed through logging of consumed methane over time with development of resistivity. This setup is part of the work of this thesis and will be used for resistivity development during hydrate formation in porous media. The experiment was the first to be conducted at the University of Bergen and therefore needs improvement. Results observed during system cooling showed decrease in resistivity with increasing salinity during hydrate formation which may be attributed to changes in the pore size. Hydrate formation blocks the pore spaces of the rock which are conductive at low salinity and have significant impact on the resistance of the sand matrix. Resistivity development can be used as an indication of hydrate formation. The increasing hydrate formation measured by the consumed methane resulted in consistently higher resistivity.

5.2.7 Future perspectives

The results of this study may provide clues to improve resistivity measurement in laboratory and interpretation of hydrocarbon presence in gas sand reservoirs. Many challenges were faced during this preliminary experimental work, and the experience encouraged ideas for possible improvements. Some improvements were realized along the way, but the time was limited and much is left to be done. Consequently, the following recommendations are drawn from this study:

- Improve the experimental set up to avoid delay in running the experiments

- The same experimental procedure should be carried out with various P & T conditions and saturation.
- The LCR-meter of type Hewlett Packard 4262A used in this experiment was an old model and needs to be replaced.
- Software for logging should be installed to avoid personal presence.
- The core holder was wrapped in insulating material to reduce supply of heat to the system, this should be improved.

5.3 Experiment II: Methane production during carbon dioxide injection

Research is still been conducted all over the world to develop appropriate techniques to produce methane gas from methane hydrates as an energy source with simultaneous storage of carbon dioxide. In view of the increasing worldwide focus on reduction of greenhouse gas emissions this concept is clearly a win win situation. This part of the thesis is devoted to description of experiments on production of methane from methane hydrate through carbon dioxide injection.

5.3.1 Experimental design II

The main purpose with this experiment was to form methane hydrates in porous media and subsequently produce methane from its hydrate during carbon dioxide injection. The experimental layout and description for this setup was described in section 5.1.1. Additionally, the injection pumps were of the type ISCO 260 D which consists of two "towers". Major leaks were discovered in tower A during the injection and the system needed an overhaul in the form of new wires and pipes. These connections were not accessible and they had to be ordered. The core carrier was the type of Hassler, where the sleeve was the type of Buna N and CO_2 resistant. The core carrier was wrapped in insulation to reduce heat flow from environment. Four CO_2 flushes were carried out. The produced methane gas from the system was collected with known 60 milli-liter sample cylinders from Swagelok. The gas composition was analyzed with a gas chromatograph (GC analysis) of type Hewlett Packard 6890 GC at the Department of Chemistry, University of Bergen to determine the gas composition.

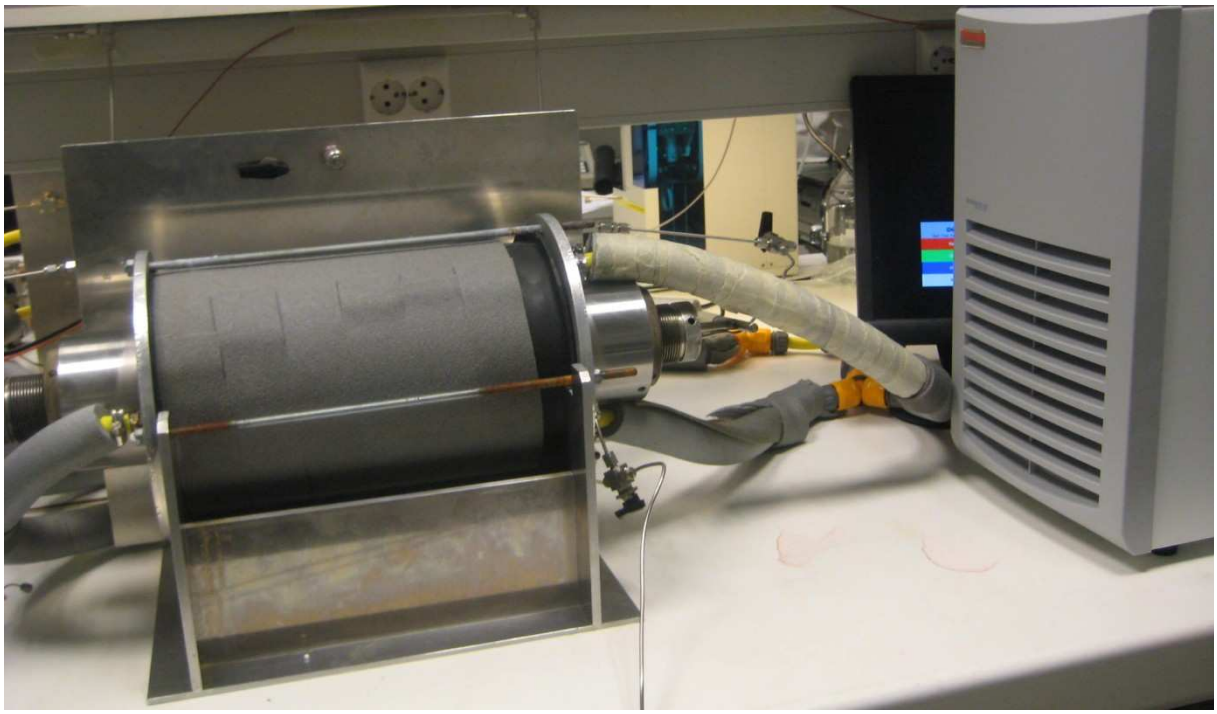

Figure 5-8: Apparatus used to study methane and carbon dioxide exchange in porous media (Schematics shown in Figure 5-9)

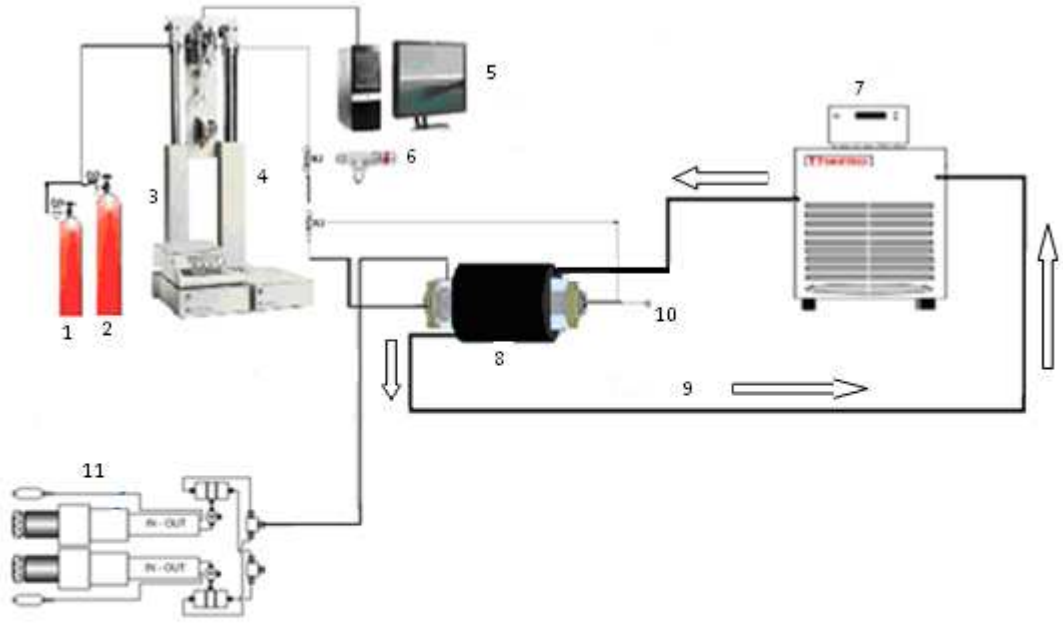

1	CH_4 cylinder	7	Refrigerated bath
2	CO_2 cylinder	8	Cooling jacket
3	CH_4 pump	9	Circulating antifreezing liquid
4	CO_2 pump	10	Thermometer
5	Computer used for logging	11	Confining pressure pump
6	Relief valve		

Figure 5-9: Basic design of the apparatus used for the study of methane production during carbon dioxide sequestration in porous media.

Figure 5-9 shows the basic design of this apparatus used for the study of methane production during carbon dioxide sequestration. This setup is different with setup 1 due to the use of two cylinders; two pumps and without a rubber sleeve.

5.3.2 Procedure for methane hydrate formation and production during carbon dioxide injection in porous media

The porous medium used and core sample preparation was similar to that described on resistivity studies in section 5.2.1. The core sample used in this experiment was saturated to 35% in water with salinity content of 5 wt%. This was done to maintain good permeability for hydrate formation. It is also beneficial to expose larger areas of the hydrate formation with CO_2. Experimental core sample parameters for experiment II is summarized in Appendix B-1. Experiment carried out for the determination of methane hydrate formation in the porous medium was conducted as follows:

- Evacuated the entire system using a vacuum pump.
- The confinement pressure was set to 400 psig. The system was filled with methane gas at 120 psig (confining pressure must be greater than core pressure to seal the system).
- The core and confinement pressure were increased in steps to 1200 psig and 1500 psi respectively.
- After hours or days with no sign of leakage, the system was cooled to experimental temperature (4^oC) to initiate hydrate formation.

At 20°C and 1bar (atmospheric pressure), CO_2 is a gas. At 20°C and 83.7 bars, CO_2 is a liquid. The full phase diagram of CO_2 (i.e. its phase at different T and P) is readily found in chemical thermodynamics (Figure 2-4). Liquid CO_2 was injected into the porous medium to replace methane from methane hydrates in which methane hydrate had been formed in advance. The apparatus included two gas cylinders and two pumps; one is for the addition of methane gas to form the methane hydrate and the other for CO_2 preparation as shown in Figure 5-9. Following the formation and stability of the methane hydrate, the injection pump was then filled with CO_2. The first CO_2 flush was carried out with free methane gas produced from the system. With an interval of a week for a flush, three other flushes were carried out and the methane produced was thought to come from the dissociating hydrate. The produced

gas was collected with known 60 milli-liter volume sample cylinder. The gas composition was analyzed by gas chromatography.

The mole fractions of methane and carbon dioxide were analyzed and the produced amount of methane was then calculated. The injection of CO_2 to replace methane from methane hydrates porous medium was done as follows:

- CO_2 was injected from the pump at 1200 psig to remove all methane gas in the lines and fracture.
- The CO_2 pump was set at constant rate (example 60 mL/min) and constant pressure (1200 psig)
- When the predetermined amount of CO_2 was injected, the pump was stopped.
- The valve on the right hand side near the thermo couple 10 of Figure 5-9 was closed to free some methane gas in the hydrate replaced with some CO_2 thus; the freed methane gas was produced. The methane in the gas phase expanded into a sample cylinder with known volume. The material balances before and after methane expansion was determined.
- The gas sample was analyzed with a gas chromatogram (GC analysis) to determine the composition.
- Four CO_2 flushes were done and analyzed.
- The CO_2 pump was used to regulate and monitor the changes in the core pressure.
- When there were no more changes in the core after these flushes, the experiment was stopped.

5.3.3 Results and Discussion

5.3.3.1 Methane injected volume during hydrate formation

Hydrate formation process by mixing a hydrate former and water and measure the rate of gas consumption was discussed in section 4. Figure 4-1 shows experiment performed for a typical gas consumption plot versus time during hydrate formation. Similarly, Figure 5-10 was generated by using data directly obtained from the computer logging via the pump during hydrate formation. The experimental thermodynamic conditions were set at 8.37 MPa and the system was cooled to 4 $\pm$ 0.5 ^{o}C. The amount of methane injected during hydrate formation was read from the logging data as 26.52 ml of methane gas (0.11mol) (Figure 5-10). There was about a total of 0.24 mol methane in the system including the initial methane saturation before the formation (0.13mol). The volume of methane injected by the pump to the core and that of the volume on the lines was simplified as two separate systems. The temperatures in the line volume outside the core and that of the methane volume before and after cooling are 20^{o}C and 4^{o}C respectively at constant pressure of 1200 psig.

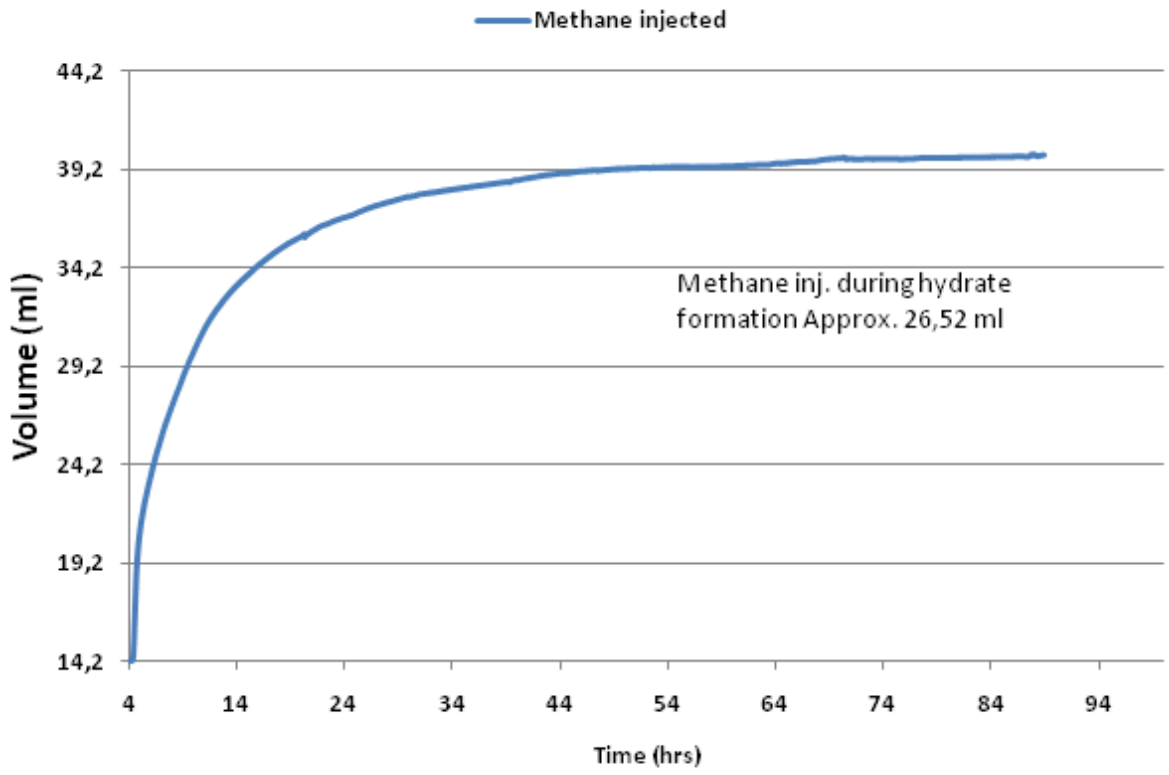

Figure 5-10: Methane injected during hydrate formation.

Figure 5-10 shows the total amount of methane injected during hydrate formation. The amount of methane injected into the system as a result of system cooling is illustrated in Figure 5-10 which corresponds to 26.52 ml. The flushes were done through the fracture were most likely all the methane in the lines outside the core and fractures was flushed. It is possible for some free methane from the pores to diffuse into the fracture and get sampled, therefore it is important to calculate the amount of free methane in the system.

5.3.3.2 Gas chromatography analysis

Methane production after series of CO_2 flushes lead to subsequent exchange between methane and CO_2 in the hydrate formation. The methane freed is drawn in small samples and analyzed with GC. The GC analysis was used to determine the composition in mole fractions which were further used in UniSim to obtain the densities of the components illustrated in Appendix B- 3. The values of other parameters such as pump, methane expansion and pore are summarized in Appendix B- 1. The volume of expansion was taken from Sloan (Sloan and Koh 2008).

The first flush removed excess methane and the rest removed methane in hydrates. Most likely all the flushes removed methane from lines, methane gas from pores, and methane gas from hydrates. In Table 5-3, the initially producible methane moles present in the core sample was 0.24 moles. The methane gas trapped in the hydrate after hydrate formation was calculated as 0.13 moles. The CO_2 pump set at rate of 60 ml / min and constant pressure of 1200 psig, CO_2 was introduced to the system and free methane was displaced from the core and the producible gas was collected into a known sample cylinder. Samples of the produced gas were taken for analysis by the gas chromatography (GC). The composition of methane and carbon dioxide in mole fractions were obtained. The mole of methane in the sample of the first flush was calculated as 0.052 mol, which is equivalent to 45% of the initial amount of free methane (0.11 mol), produced. Further calculations were performed for three flushes with the assumption that the remaining free methane was immobile and thus not produce significantly by subsequent flushes. After the first flush, the remaining producible methane gas trapped in the hydrate was still 0.13mol. In the second flush, a production of 32.5% was obtained. The third gave the production of 30.4%, and the fourth 0.8%. The total recovery resulted to 63.7% of the initial amount of methane trapped in hydrate assuming that the remaining free methane was not produced. The Production of methane by injection of CO_2

using this setup was experimentally verified. The ratio between the produced CH_4 and CO_2 from the gas chromatography and calculations are presented in Appendix B- 2.

The methane remaining after these flushes were also calculated. It can be seen from Table 5-3 that methane was decreasing in the hydrate phase with increasing CO_2 (see also Appendix B- 3 for CO_2). The close relationship between the methane percentages recovered and the CO_2 hydrate formed implies that methane was replaced in the hydrate.

Table 5-3: Calculated amount of methane during CO_2 flushes

Description	**1st CO_2**	**2nd CO_2**	**3rd CO_2**	**4th CO_2**
Flush	**1**	**2**	**3**	**4**
Moles of CH_4 in sample	0.0517	0.0411	0.0384	0.00103
CH_4 moles in hydrate within the pore space	0.2408	0.1264	0.0852	0.0468
Free moles CH_4	0.1144	-	-	-
CH_4 in hydrate (mol)	0.1264	0.1264	0.0852	0.0468
CH_4 recovered (%)		32.5	30.4	0.8
Total recovery (%)		63.7		
Remaining CH_4 in core(mol)		0.0852	0.0469	0.0458
Total remaining(mol)		0.1779		
Free CH_4 recovered		45.2%		
Remaning free CH_4 (mol)		0.0628		

	Temperature (^oC)	**Pressure (psig)**	**Density (g/mL)**	**Vol.(ml)**	**n(moles)**
Free CH_4 in Line	20	1200	0.0648	9.14	0.0369

Table 5-3 shows the conducted flushes and calculated amount of methane recovered.

Based on the work of Park (Park, Choi et al. 2008) yielding high recoveries 65-95% when methane hydrate is exposed to diatomic guest molecules such as CO_2, 64% recovery (Table 5-3) was observed in this work. Although this may reflect high recovery, significant aspects such as P and T conditions, uncertainties, scale and appropriate experimental method are taken into consideration. The technique of calculating recovery directly suffers from several problems concerning sample preparation and assumptions made in the analysis. Repetition of the experiment for CH_4 and CO_2 exchange should be further investigated to compare literature and previous results. Significant effort should be devote to more accurately determine the CH_4 recovery efficiency from hydrates during CO_2 sequestration.

5.3.3.3 Uncertainties

There are many sources of error in this experiment, arising from uncertainties of pressure, temperature, composition (GC analysis), leak, and the range of sample density. A number of further uncertainties with smaller contributions to the error are also considered. The uncertainties in temperature were considered to be $\pm 0.1^{o}C$. The compositional uncertainty (mole fraction) arises from reading the peak height in the chromatogram ±1% mole.

The remaining errors are also sources in comparison to those mentioned above. The uncertainty estimated for the leak was very had to estimate, it varied from ±0.0001 – ±0.05 ml/hr. The uncertainties of the slide gauge used in the initial stage measurements of length and diameter are in the order of ±0.02mm. The balance uncertainty used for the weight measurement is about ±0.01grams. Most equipment used in this work was made at the University of Bergen work shop and their uncertainties were written on them. But the impact of different sources of error on the overall experimental uncertainty is difficult to estimate due to different time lags between recording and actual impact on the process

5.3.3.4 Conclusion

Laboratory experiments with core samples to determine whether methane can be produced from natural gas hydrate deposit indicates relative preliminary producible results in this study. Although the methane recovery values calculated in this work may contribute to some difference with the most promising work of Park et al, the primary cause of the recovery difference is attributed to the nature of the appropriate experimental preparations. The results showed that when methane hydrate was exposed to carbon dioxide an exchange of gas molecules occurred. The results may as such be regarded as a promising alternative in the solution of some important global issues like energy supply and reducing impact of carbon dioxide emissions on climate change through safe storage of carbon dioxide. From the experiments in collaboration with the Reservoir Physics Department University of Bergen, an experimental setup to run laboratory scale experiments to test methane production studies from methane hydrate during carbon dioxide injection has been installed.

5.3.3.5 Future perspectives

The success and experience gained from this work gives a wide range of opportunities for further research. There is a need to improve the experimental set up in order to avoid delays; however, hydrate experiments could include a thorough investigation on the subsequent exchange rate. Repetition of the experiment for CH_4 and CO_2 exchange should be further investigated to compare literature and previous results. Significant effort should be included to more accurately determine the methane recovery efficiency from hydrates during CO_2 sequestration. Park et al 2008 has shown that exposing CH_4 hydrate to a mixture of CO_2 and N_2 increases the methane recovery since nitrogen may enter the small cavity instead of methane in some of the small cavities of the converted hydrate. This is practically interesting since it might open up for direct injection of flue gas without separation. On the negative side comes the issue of diluted CO_2 mixture, which reduces the thermodynamic driving force and slows down the conversion process. But experiments with diatomic guest molecules such as N_2 should be considered in mixtures with CO_2.

6 Simulations

This chapter provides information about the background of the simulations and references taken to run the simulations. In section (6.3), setup of the simulations was discussed

6.1 Study area

Figure 2-1 shows several known hydrate sites in the world; however this thesis focuses mainly on the fields at the Nankai Trough offshore wells in Japan that have either been part of hydrate production efforts or considered for hydrate production in the near future.

6.2 Simulation basis

Comparing theoretical results with experimental observations is not straight forward. Never the less, some good experimental results and a well studied natural gas reservoir were chosen as basis for simulation conditions in this work. Japanese scientist drilled wells with the objectives of characterizing the methane hydrate and investigating the petroleum potential of a deeper formation. The wells were drilled through Bottom Simulating Reflector (BSR) seismic program to decide the location of the hydrate at the Nankai Trough offshore in Japan.

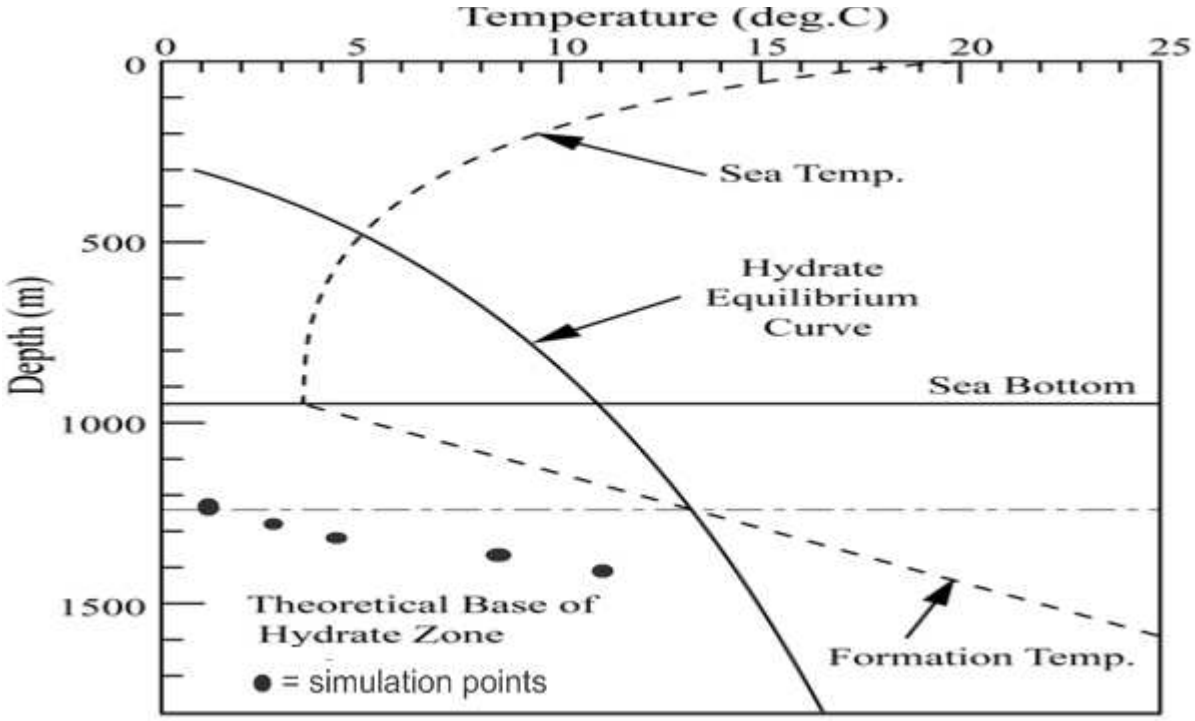

Figure 6-1: Estimated down hole temperature and methane-hydrate equilibrium curve in Nankai-Trough wells offshore Japan modified from (Takahashi, Yonezawa et al. 2001).

Figure 6-1 shows the equilibrium curve of methane hydrate and the estimated in-situ temperature of the well at 950 m water depth. The two curves in Figure 6-1 crosses at depth of

1240 m. Thus, the BSR at 1240 m on the seismic section was shown to be the base of the hydrate zone (Takahashi, Yonezawa et al. 2001). The thermodynamic conditions for these simulations were taken from Figure 6-1.
Based on the knowledge of increased thermodynamic stability it was hypothesized that CO_2 could replace and recover CH_4 molecules if exposed to CH_4 hydrate under the Nankai Trough offshore wells in Japan (Ohgaki, Takano et al. 1994).

Several early researchers investigated the CH_4-CO_2 exchange mechanism as a possible way to producing methane from hydrates (Ohgaki, Takano et al. 1996). These studies emphasized the thermodynamic driving forces that favors these exchange reactions, since many of these early studies dealt with bulk methane hydrate samples placed in contact with liquid or gaseous CO_2 were available surfaces for interaction were limited. Yoon et al, 2004 (Yoon, Kawamura et al. 2004) studied the CO_2-CH_4 exchange process in a high pressure cell using powdered CH_4 hydrate and then exposed it to CO_2. They observed a fairly rapid initial conversion during the first 200 minutes, which then slowed down significantly. Another interesting feature discovered from NMR measurements on these systems was that the conversion process was essentially a solid state conversion. This is also in accordance with recent modeling at UoB (György Tegze, LászlóGránásy et al. 2007; Tatiana Kuznetsova 2009).

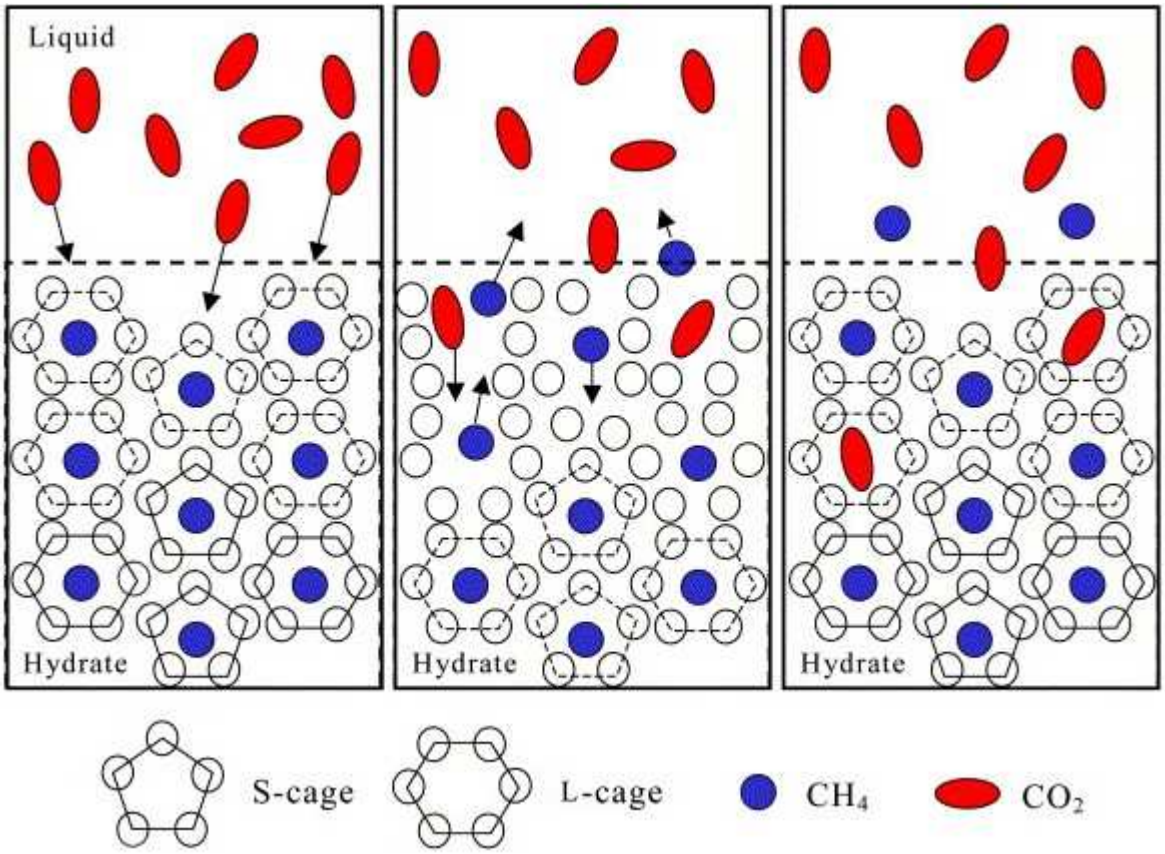

Figure 6-2: Schematic diagram of the CH4 and CO_2 molecule exchange in the large cavities modified from (Ota, Morohashi et al. 2005)

Figure 6-2 showed that when CH_4 hydrate was exposed to liquid CO_2 an exchange of gas molecules occurred spontaneously, as CO_2-hydrate is the thermodynamic preferred hydrate (Ota, Morohashi et al. 2005). *S* and *L* denote small and large cages respectively. The molecular exchange process release CH_4 which can be made accessible for production.

Significant remarkable recovery of methane by using diatomic guest molecules such as CO_2 and N_2 was found (Park, Choi et al. 2008). They found diatomic guest molecules may compete with methane for occupancy of the smaller sI cages, while CO_2 would occupy only the larger sI cage without any other challenge of other guests. They also found that sII and sH would convert to sI yielding high recoveries (65-95%) when exposed to CO_2 or CO_2-N_2 mixtures.

6.3 Simulation setup

Currently a wide variety of computers are available for simulation studies. In this study Linux clusters at the IFT building have been used to run the simulations. Some of the simulations have been conducted on hexagon, which is a CRAY YMP, and fimm, which is a

multiprocessor cluster mounted at UoB, both of them run by the BCCS (Bergen Center for Computational Science). The clusters used at the University of Bergen Norway are not enough or very slow due to processor speed, memory limitations and in some cases limitations in data transfer speed.

Solving all the differential equations by integration over space and time requires substantial computational efforts. The three component extension of equation (4-7) is described in detail in Tegze et.al. (2007) and will not be repeated in detail here.

In addition to the CPU time itself, which may range from a week to several months, it is very time consuming to locate the data in the code, modify the code to fit your grid system, enter the grid system and then eventually run the simulation. Due to the amount of data required, it is often good to consider data which had previously been accepted.

As the actual case study I have considered depths for a well defined project. Nankai Trough is the main focus of MH21, the Japan hydrate energy project. Analysis of published data on depths of hydrate zones have been the basis for establishing simulation conditions using temperature profiles constructed from reported geothermal gradient and pressures from surface pressure and overburden gravity induced pressure. More specifically pressure is calculated through the use of equation (6-1) and temperature conditions (Figure 6-1) at which hydrates were present. I started the thermodynamic code to calculate the free energies and their derivatives on given temperature and pressure conditions. These pressure and temperature conditions were inserted into the thermodynamic code programmed by Atle Svandal (Svandal, Kvamme et al. 2006) which calculates the Gibbs free energies for a system and also generate extension data files such as *m files*, *inc files* and *inp files*. The thermodynamic code and *tabulate.m* file was opened in MatLab and parameters such as temperature and pressure were edited as desired. The molar volume v_m was set as 18.02 $\frac{m^3}{mol}$. The step max *N* was set to 201 for all simulations. The tabulate script was executed to get the table of the solid and liquid free energies and the required derivatives. Solid files in the *x, y* and *z* directions were generated as *dfsperdx.inp, dfsperdy.inp* and *dfsperdz.inp* while *dflperdx.inp, dflperdy.inp* and *dflperdz.inp* were generated for liquid free energies as derivatives. Hence the tabulate script was executed, it saved all *inp* and *inc files*. These *inc files* were the result files that were copied in to the PFT code.

The Phase Field model programmed by László Gránásy for the hydrate system in collaboration with Kvamme, B (Gránásy, Pusztai et al. 2003) was written on C language in which several inputs like size of the hydrate, total size of the system and concentration in liquids and hydrate at time zero were changed to run the simulations. The simulation generates results for all grid points in the form of concentrations for all component and structural order ϕ at given time step intervals. The PFT code stores all the necessary data at various points in time. MatLab software enables this work to perform computationally tasks faster than manual or excel calculation. For very big simulation, it is not necessary to complete the simulation to check the intermediate results. Simulations were carried out at different depths, temperatures and pressures with the first simulation corresponding to the point at which methane hydrate was first noted. To make the PFT code run, I copied all input files such as *inc* into the PFT code. The *main.h* was dealt with to define dimensions such as 2D or 3D but 2D was chosen in this work as *x, y* directions. It was done as follows:

- *Vim main.h* to open the main.h files
- Set *innerstep max* and *step max* $1.0e^{4}$ and $1.0e^{2}$ respectively
- Set the *Langrange constant* as $1.0e^{-15}$
- Multiply step 1 and 2 to calculate simulation time in seconds.

The step max gives the number of steps and how often output files are written to the screen. Further the *main.c files* were opened. These files take care of all Multi Processors Interface (MPI) communication between the neighbor grid points. The concentrations of the sample are here changed to desire. These codes are copied in a CD and attached to this thesis.

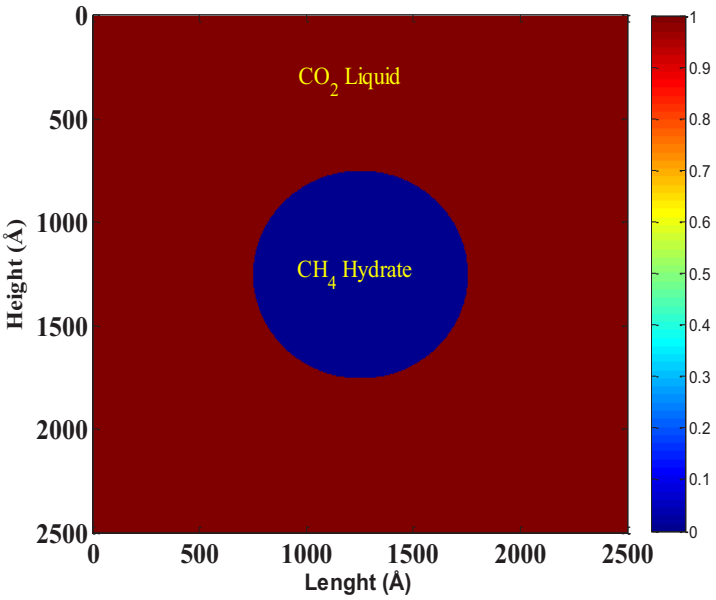

Figure 6-3: Simulation at time zero, showing the initial picture of CH4 hydrate and liquid CO2 with 2500x 2500 grid points and a hydrate radius of 500 grid points, color codes represent φ = 0 and 1 for methane hydrate and CO_2 liquid phases respectively.

Figure 6-3 shows square structure used to study CH_4 and CO_2 exchange when CH_4 hydrate was placed in the center surrounded by liquid CO_2. The field colors on the right hand side of the geometry represents the color code defined as φ which is a structural order parameter assuming the values φ = 0 and 1 in solid and liquid respectively. Intermediate values correspond to the interface between the two phases. The mole fraction of CH_4 in the hydrate and that of the CO_2 in the liquid phase were 0.14 and 1.0 respectively. The CH_4 concentration was initially 0.14 in the hydrate and that in the liquid was placed as negligible (1.00e-08). The concentration of methane in liquid was set to get the differences in concentration or more precisely the corresponding chemical potential differences which liberate the diffusion from hydrate towards liquid side. The CO_2 concentration was initially 1.0 in the liquid and that in the hydrate was placed as almost negligible (1.00e-08).

The size of the system (2500 × 2500) grid points was calculated using Lagrange Method which corresponds to area $6.25e^{-14}$ m^2. The total hydrate unit cell in the initial solid with radius of 500 grids cells shown in Figure 6-3 corresponds to circular area $7.854e^{-15}$ m^2. The

area of the surrounding fluid (CO_2) and the volume of the hydrate were thus 5.46 e^{-14} m^2 and 5.24e^{-22} m^3 respectively. The simulation time was calculated using Lagrange method which is innerstepmax (1.0e^4) × data files generated × the Lagrange constant (1.0e^{-15}). The Lagrange constant was defined in the PFT code. The simulations were run up to 100 ns.

Equation (6-1) was used to calculate pressure inside the hydrate zone from Figure 6-1.

$$P_z = P_o + \rho g(z - z_o) \tag{6-1}$$

where;

P_z is hydro static pressure at depth z, P_o is initial pressure ρ is density, g is gravity, z is the depth, z_o as the initial depth. Prior the simulation, a cross check was made with the hydrate stability curves in Figure 2-4 and Figure 2-5 to make sure the pressures calculated from equations (6-1) falls within the hydrate zone. Results of equation (6-1) are listed in Appendix C- 1.

Table 6-1: **Temperatures and pressures simulation zones.**

Name	Sim1	Sim2	Sim3	Sim4	Sim5
Temperature (K)	274.15	276.92	278.99	282.79	284.17
Pressure (bar)	100	102.94	105.89	111.28	113.24
Depth (bsf(m))	0	30	60	115	135

Table 6-1 shows the thermodynamic conditions used to run the different simulations.

7 Results and discussion

7.1 Concentration of CO_2 in hydrate and liquid phase

This section focuses on the amount of liquid CO_2 converted into CO_2 hydrate. Pressure and Temperature conditions (Table 6-1) were used to run the simulation in a 2500 X 2500 grid point geometry illustrated in Figure 6-3. The initial methane gas concentration and water in the hydrate was 14 and 86% respectively, surrounded by 99% mole fraction of CO_2 liquid. The radius of the methane hydrate was set to 500Å as discussed in section 6.3.

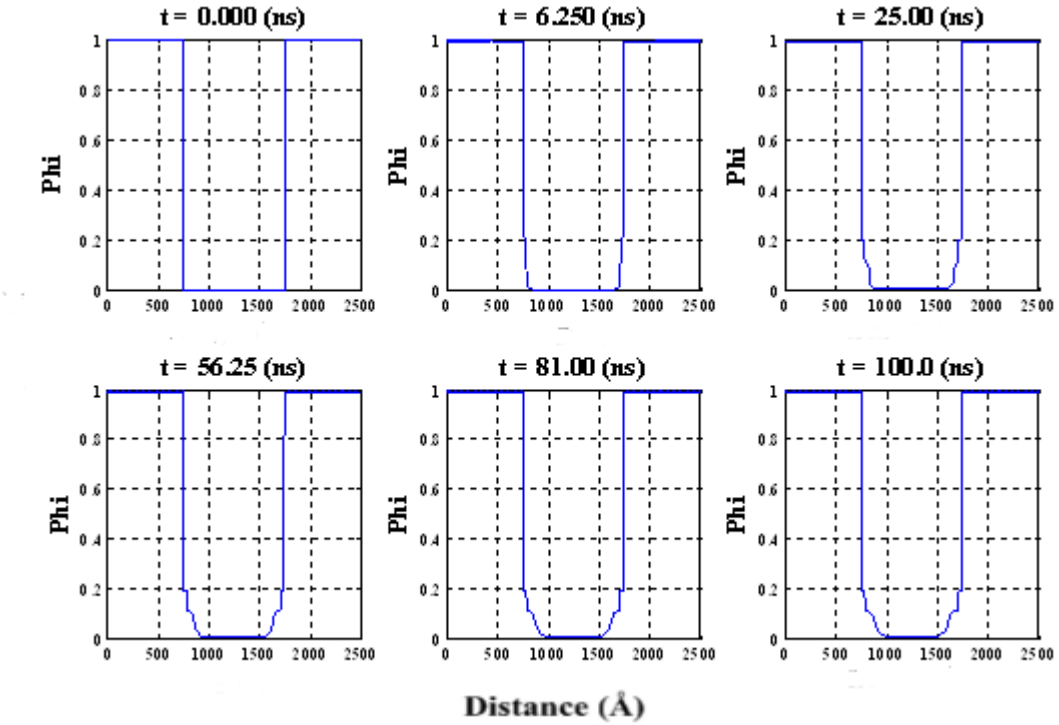

Figure 7-1: Structural phase parameter φ of the dissociating CH_4 hydrate and exchange of CO_2 at different pressures and temperatures. The wells above shows the distance between hydrate and liquid for φ = 0 and 1, solid and liquid respectively. Between phases φ = 0 and 1 are interface values.

Figure 7-1 shows the likely event of CO_2 starting to enter some parts of the methane hydrate at the moment when some methane gas has been released into the surrounded CO_2 at high pressures. The unit cell contains 46 H_2O molecules lattice structure which comprises 2 small cavities and 6 large cavities, only the large cavities may be occupied by the molecules of CO_2. Thus, the number of CO_2 molecules enclosed in this lattice may vary depending on the specific temperature and pressure conditions under which the hydrates are formed.

Most data indicated CO_2 cage occupancy depends primarily on its diameter and operating pressures, higher pressures increasing the number of molecules which become "trapped" in

the ice lattice structure. With the MatLab software used to generate Figure 7-1, changes in the size of the methane hydrate was observed as CO_2 enters the hydrate. The high concentration of methane gas released from the methane gave a good passage for CO_2 to enter the hydrate. Analysis on how the replacement occurred in Figure 7-1 is hardly seen so, it is therefore summarized in Appendix C-6.

The methane hydrate dissociates by releasing more methane gas thereby reducing it size. The hydrate size reduced from start of the simulation to 81.00 ns, the size then increased before 100 ns simulation time. Phenomenon behind the hydrate size increase is best explained by looking at the change in concentration values in liquid CO_2. Initially, there was no change in liquid CO_2 concentration until when some methane gas was released from the hydrate. Reason for the hydrate size increase after 81.00 ns was best explained by some amount of CO_2 that had entered the methane hydrate competing to replace the methane gas in the larger cavities. At this point, it was realistic to say the mass transfer phenomenon process had lead to reformation of CO_2 hydrates by means of sequestration of CO_2.

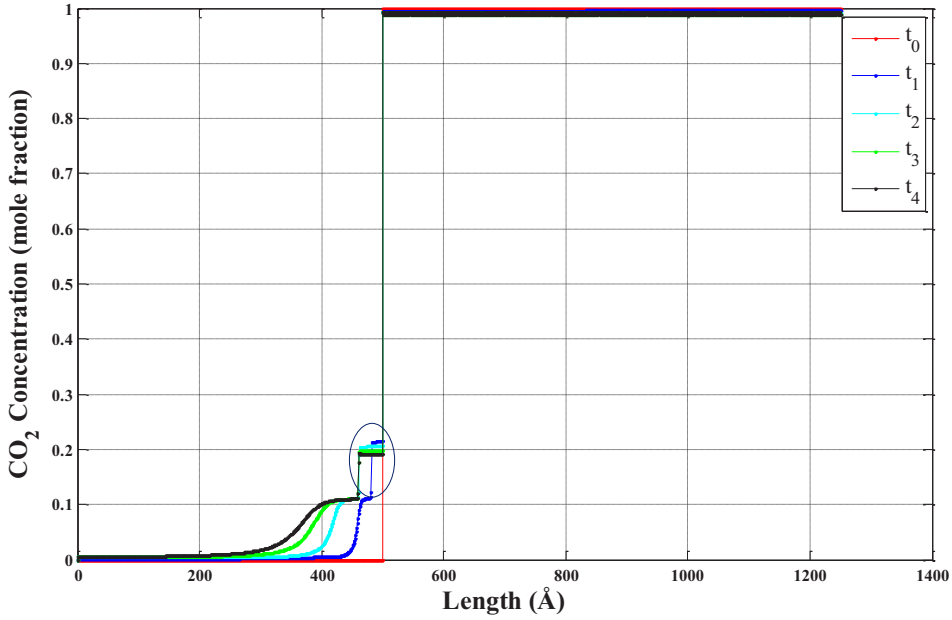

Figure 7-2: CO_2 concentration as a function of distance and times t_o, t_1, t_2 , t_3 and t_4 in liquid and hydrate center (0-1250Å see Figure 6-3).

Figure 7-2 presents the CO_2 hydrate reformation process. It individually addresses each stage of the kinetics of liquid CO_2 from its liquid phase transformation to solid phase.

The blue circle encloses a thick interface between liquid and solid phase. These interfaces are well explained in Figure 7-3 in the next paragraph.

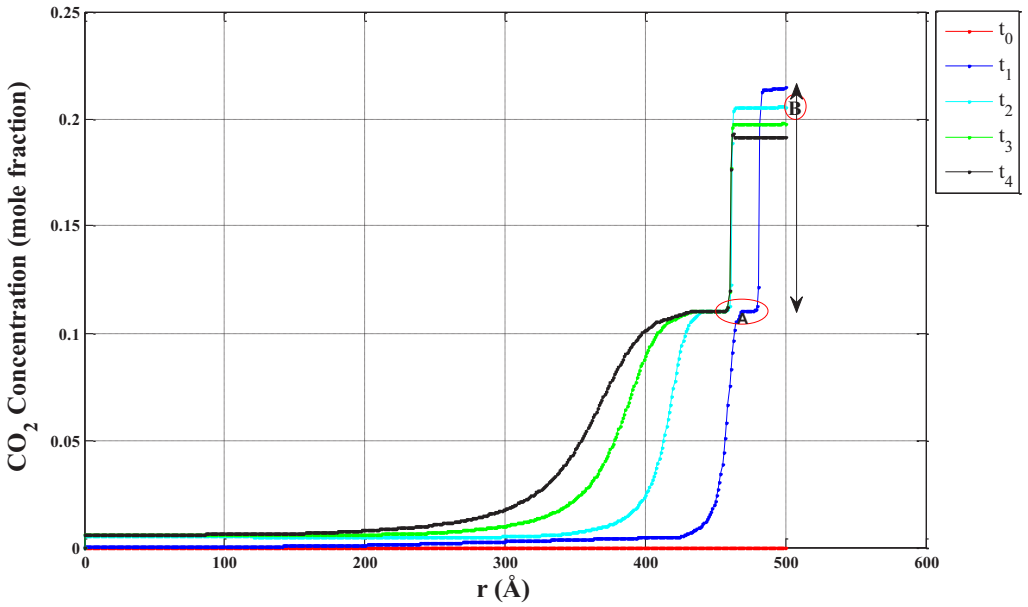

Figure 7-3: CO_2 concentration inside hydrate as a function of radial distance at different points. t_o, t_1, t_2 , t_3 and t_4 are different times at points 500Å, 480Å, 460Å, 420Å & 410Å respectively away from the original interface.

Figure 7-3 shows concentration of CO_2 in the hydrate as a function of radial distance. On the right of Figure 7-3, the CO_2 in the hydrate had already reached the front at the interface between the hydrate and liquid. Point A represents the front of totally converted liquid CO_2. This point was used to make an estimate of the total CO_2 converted which was approximated about 0.12 mole fraction. Between B to A the system formed an interface with the liquid phase resulting to an initial relaxation of the system into a physically realistic interface. The interface between points A and B also corresponds to the circle in Figure 7-2. The front in Figure 7-4 is observed at point A which corresponds to the interfaces between 440 to 500 Å. The different interfaces in Figure 7-2 and Figure 7-3 were noted at time t_o, t_1, t_2 , t_3 and t_4 as the interfaces increases from 0, 21, 42, 42 and 60 Å respectively. The interfaces became stable after t_2 .

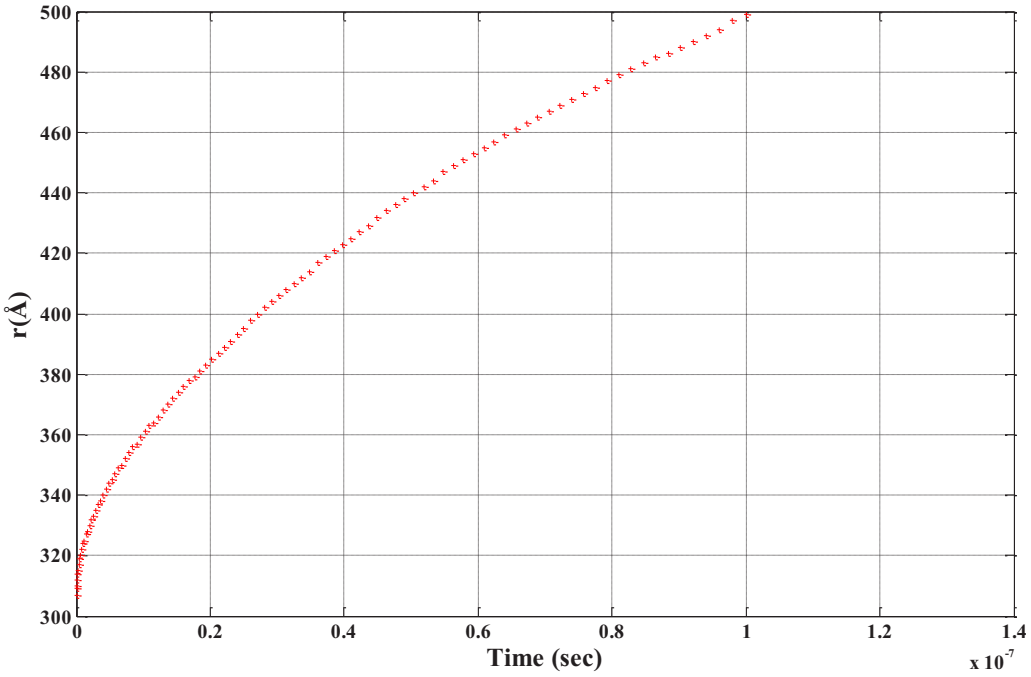

Figure 7-4: Thickness of the hydrate film as function of time showing totally converted CO_2 at the front

Figure 7-4 shows the thickness of the hydrate film as function of time. A growth is observed in Figure 7-4 which follows the mathematics behind diffusion. The rate of mass transport of material flow remains proportional to the concentration difference and inversely the distance between the opposing concentrations (Fick's second law). The transferring amounts of CO_2 from liquid to hydrate phase from high to low concentration area is called diffusion.

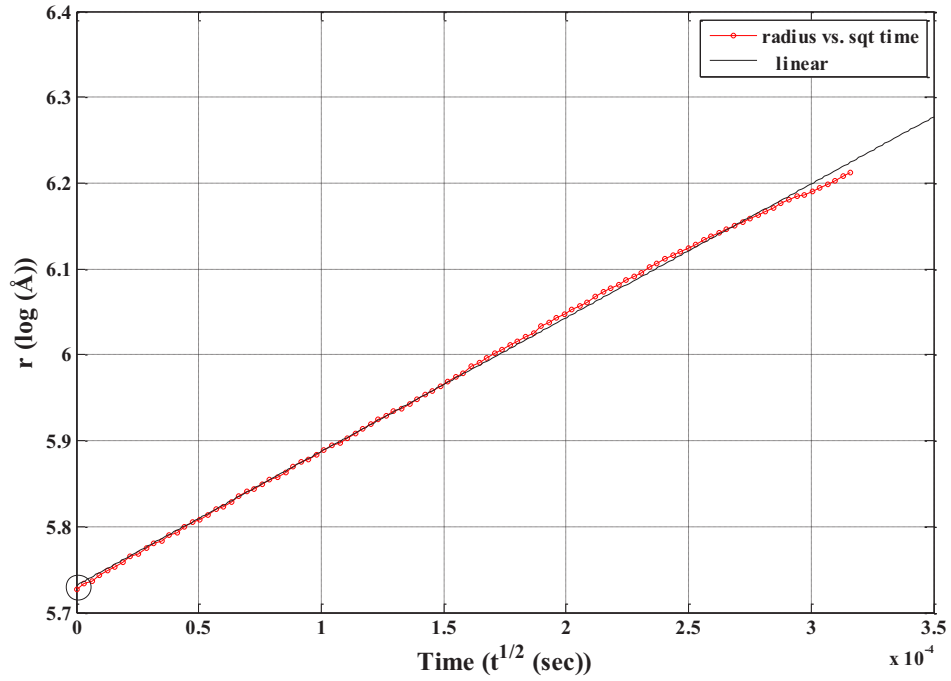

Figure 7-5: Illustration of the power law

Figure 7-5 shows the characteristics solution of the power law ∞ $t^{1/2}$ indicating a diffusion controlled process described by Ficks's law. It shows log of the radius in an increasing proportionality to the square-root of time. Linear fittings were observed which illustrate Fick's law. The circle on the left did not start at zero due equilibrium creating interface at start, i.e. the system initially started as a sharp interface, which is in contrast to a realistic interface in the order of 1 nm based on earlier research on similar systems (Svandal, Kvamme et al. 2006).

An approximation of the integral of the plots shown in Figure 7-1 was found using the trapezoidal method in MatLab (see cd). Since the liquid has the value φ =1 and the hydrate φ = 0, the integral summarized the current amount of liquid CO_2 in the system. To observe the movement of CO_2 and CH_4 from liquid to solid phase verse versa, the velocity on the interface was determined by tracking the φ values.

The velocity on the interface was calculated using equation (7-1) .

From this the velocity (v) can be found by:

$$v = \frac{(I_2 - I_1) \times 1.0\ E^{-10}}{t_2 - t_1 \times 1.0\ E^{-15}} \tag{7-1}$$

where v is the velocity at the interface of the two fluids, I_1 and I_2 are the concentration values ($xc1\ and\ xc0$ for methane and CO_2 concentrations respectively) at times t_1 and t_2. The size of the time steps and the grid size were inserted into the equation to give corresponding units [m/s]. From equation (7-1) the hydrate reformation rate was calculated using equation (7-2) and the data from these calculations were saved in a CD and attached with this thesis, from which Figure 7-6 and Figure 7-11 were generated.

The flux which is a vector is calculated as:

$$\vec{J} = v \times \frac{\rho_{Hyd}}{M_G} \tag{7-2}$$

where,

$\vec{J}$= flux (mol/m^{2}s)

v = velocity (m/s)

ρ_{Hyd} = Density of hydrate (kg/m^3)

M_G = Molar weight of the guest (kg/mol)

The fluxes of CO_2 were integrated at different points and time in the hydrate using trapezoidal method in MatLab; which can be mathematically presented as:

$$\int_0^t \int_{r_0}^{r} \vec{J}(t,r) \times 2\pi r dr(t)\, dt \tag{7-3}$$

where, $\vec{J}$ = flux (moles/m^{2}s), r = radius (m) and t = time (s)

This command computes an approximation of this integral with unit spacing. Input data such as number of data files, density and molecular weight of the component were included to successfully run the calculations. The decomposed and accumulated molecules of methane and CO_2 were calculated.

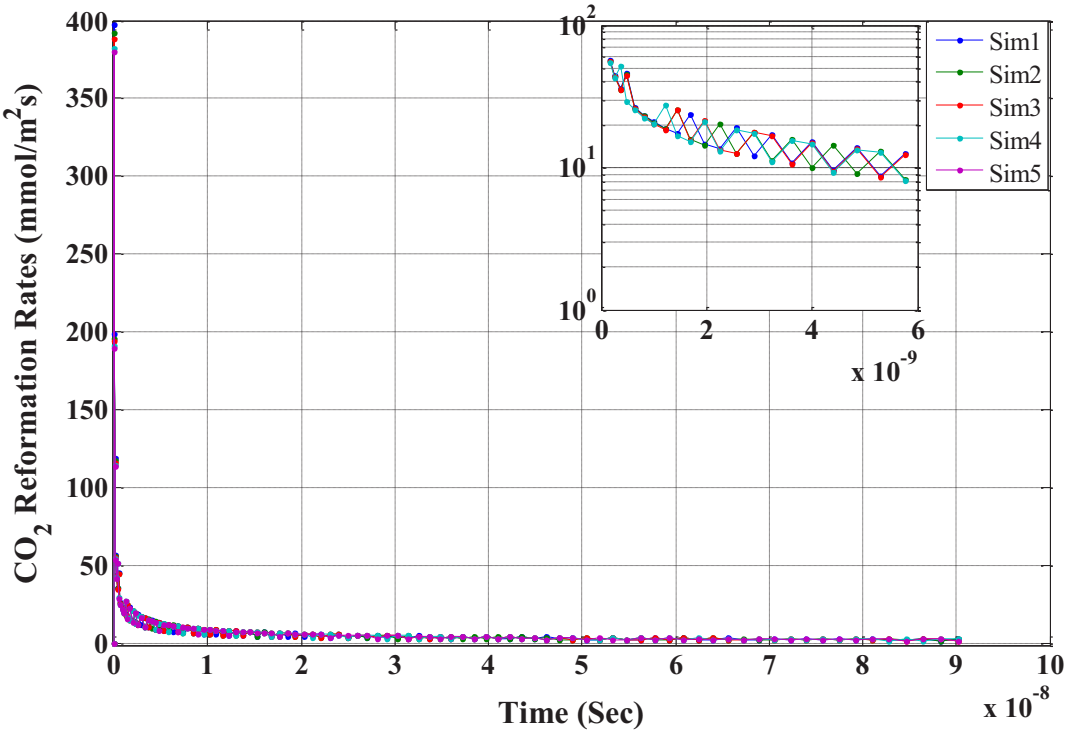

Figure 7-6: CO_2 fluxes as a function of time.

Figure 7-6 shows the reformation rate of CO_2 as a function of time calculated from equation (7-2). The curves looks very identical and hardly to distinguish between the reformation rates of the different simulations. Therefore, these curves were zoomed as shown on the right above to illustrate the clear picture of the reformation rates. The picks shown on the zoomed

diagram indicates the noise effects between the grids. These fluxes were integrated at different points and times near the hydrate interface using the trapezoid command code. The results are shown in Table 7-1.

Table 7-1: Accumulated CO_2 molecules into the hydrate

Simulation	Temperature (K)	Pressure (bars)	CO_2 hydrate density(kg/m^3)	Total CO_2 molecules accumulated into hydrate
1	274.15	100	873.9	1.6253e+006
2	276.92	102.94	861.8	1.6752e+006
3	278.99	105.89	854.5	1.6846e+006
4	282.79	111.28	841.3	1.6727e+006
5	284.17	113.24	836.8	1.6270e+006

Table 7-1 shows the amount of CO_2 molecules converted during the period of each simulation. The hydrate center was seen to be 1250Å (Figure 6-3). The CO_2 molecules converted were traced at one edge of the hydrate about 250Å away from the liquid interface towards the center of the hydrate. Similar traces were done for methane at the same point and time as illustrated in next chapter.

7.2 Extrapolation for CO_2

Figure 7-5 shows that the process of diffusion was much controlled by mass transport, although it was quite clear that my simulations were far from convergence into a stationary kinetic exchange. Therefore, the latest portions of Figure 7-5 was used to estimate Diffusivity in Fick's law and to extrapolate the reformation rate of CO_2 at longer time scales as shown in Figure 7-7. The extrapolation of the simulation was done using power law $\alpha\ t^{1/2}$ which shows all the simulation results following the same trend and change in their rates are so small that cannot be visible in Figure 7-7. The reason may be the fluxes were so closer for the different simulations causing an overlap. The zoomed graph on the right of Figure 7-7 showed some clear behavior of the simulations.

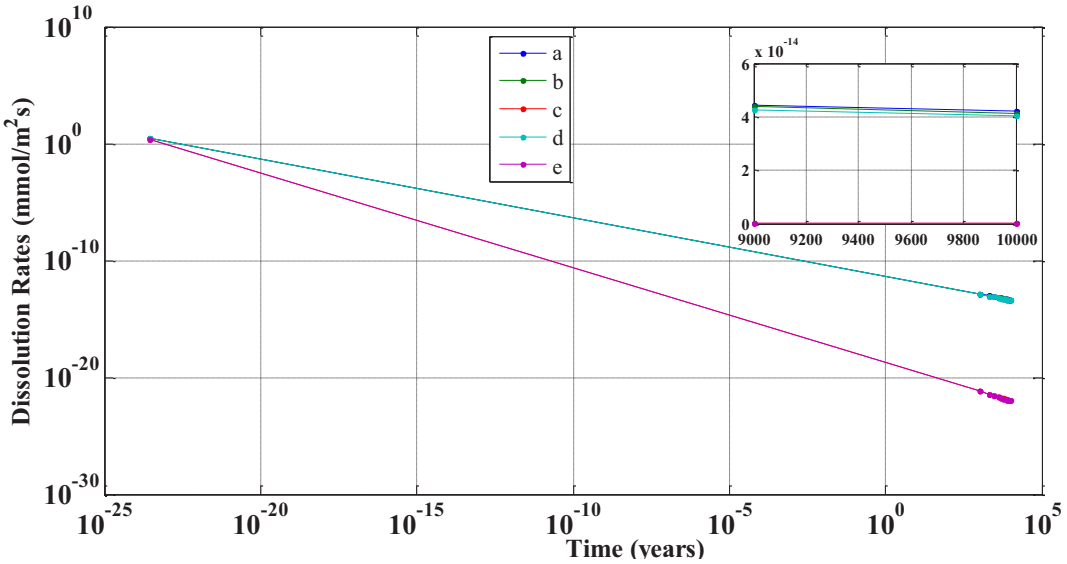

Figure 7-7: Extrapolation of reformation rate of CO_2 up to 10000 years

The extrapolation was done to compare the values with those of CH_4. After 10000 years the reformation rates for simulations Sim4 (d) and Sim5 (e) were 4.045E-6 and 9.863E-23 mmol/m^2s which corresponds to 1.276E-6 and 3.110E-15 mmol/m^2yr respectively.

7.3 Methane concentration in hydrate and liquid phase

Following the final time of the simulation, the size of the methane hydrate was observed to have reduced as methane diffuses into the CO_2 liquid as CO_2 enters into the large cavities of the methane hydrate.

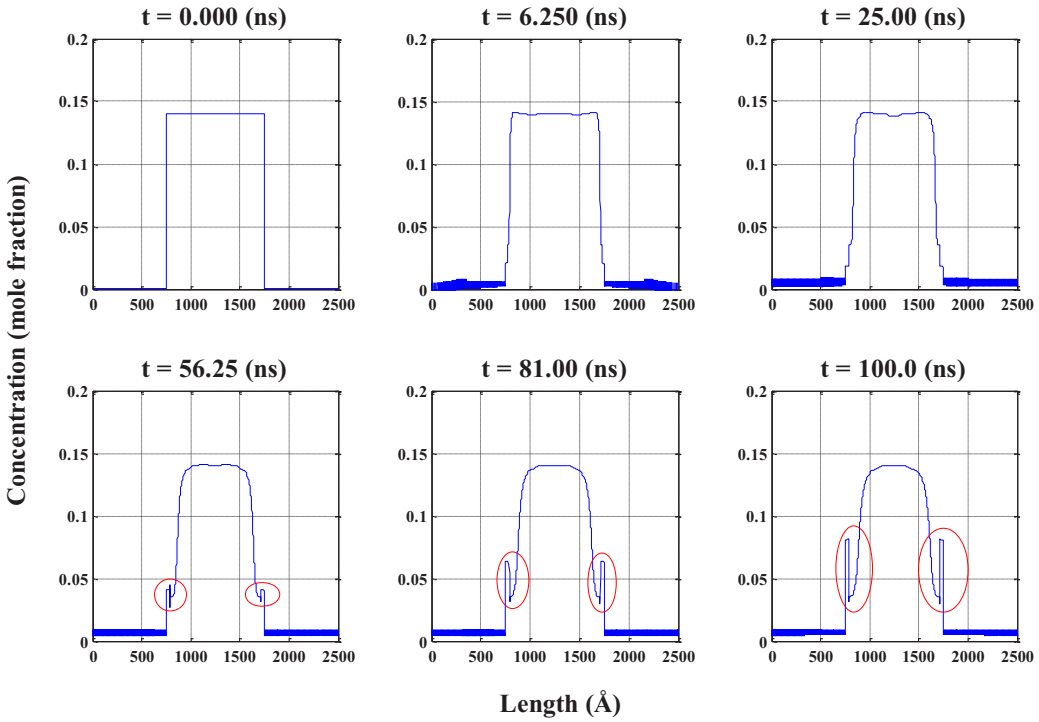

Figure 7-8: Methane concentrations as function of length.

On the pretext of the size behavior, Figure 7-8 illustrates the presence of methane in both liquid and hydrate phases at different time intervals with concentrations as a function of length. Methane concentration in the liquid phase at t = 0.000 ns was almost negligible as observed. No interface was created. The red circle in Figure 7-8 represents interface created during the mass transfer process. The interface increases with increasing time and so also the methane concentration in the CO_2 liquid. At the end of the simulation, more concentration of methane was observed to have diffused into the liquid phase forming a transition zone.

It is simply because some vertices of the water cages in the hydrate phase has dissociated into the liquid phase. Thus, prompting some methane molecules in the hydrate phase to diffuse rapidly into the liquid phase. The methane concentration in the liquid phase then increased sharply from zero to finite value. It clearly indicated the system has developed three phases' namely liquid carbon dioxide, methane gas and methane in hydrate + carbon dioxide in hydrate.

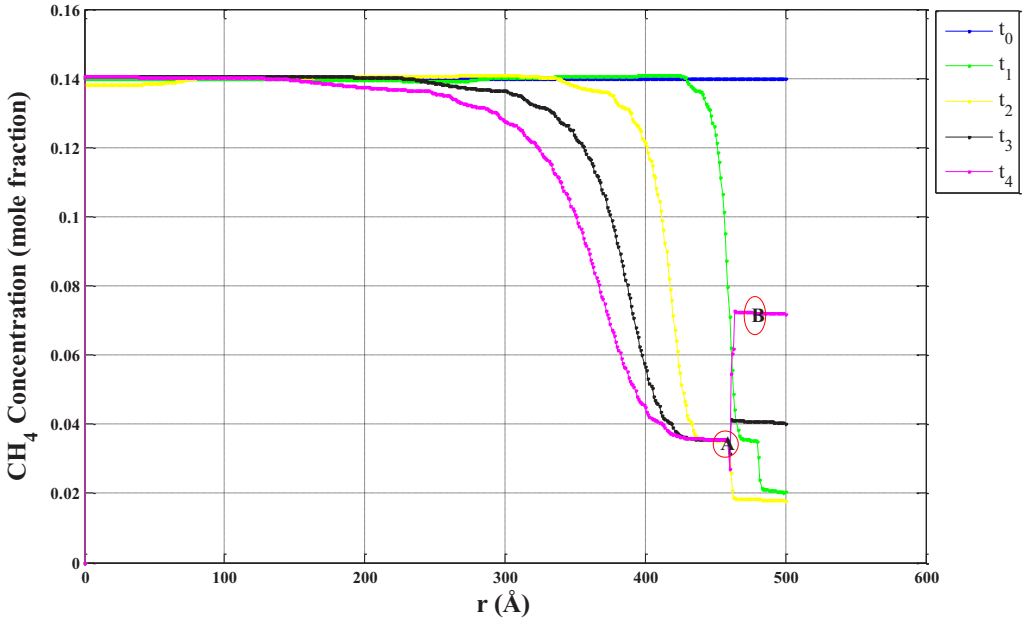

Figure 7-9: Methane concentration inside the hydrate as a function radial distance at different points. t_o, t_1, t_2 , t_3 and t_4 are different times at points 500Å, 480Å, 4600Å, 420Å & 410Å respectively away from the original interface.

Figure 7-9 shows how the hydrate size shrinks as time elapses. The radius of the original hydrate was 500Å, the radius decreases with increasing time. Different interfaces were noted at time t_o, t_1, t_2 , t_3 and t_4 as the radius decreases from 500, 480, 440, 420, and 410 Å respectively away from the solid - liquid interface. Initially at $t_o = 0$, the mole fraction equals the initial values which showed that methane has not yet diffused. To get the clear vision of diffusion inside the hydrate, the concentrations were taken on five points corresponding to values 410Å, 420Å, 440Å, 480Å and 500Å showing distance from the original interface. The interface decreased slowly between t_o , t_1 and t_2 thus, increased slightly at time t_3 and t_4 which represents point A and B in Figure 7-9. The interfaces became approximately stable after t_2 .

Simply this phenomenon can be defined by solubility which is a measure of how much methane (solute) will dissolve into the carbon dioxide (solvent). Not all the methane will dissolve in all the carbon dioxide and it is because polar solvent molecules separate the molecules of other polar substances. The interface thickness between the hydrate and the fluid is a sharp stable interface where there is no thermodynamically equilibrium between the wall of the hydrate and that of the fluid. The measure of how the methane gas has dissolved into the carbon dioxide liquid is represented by Figure 7-10.

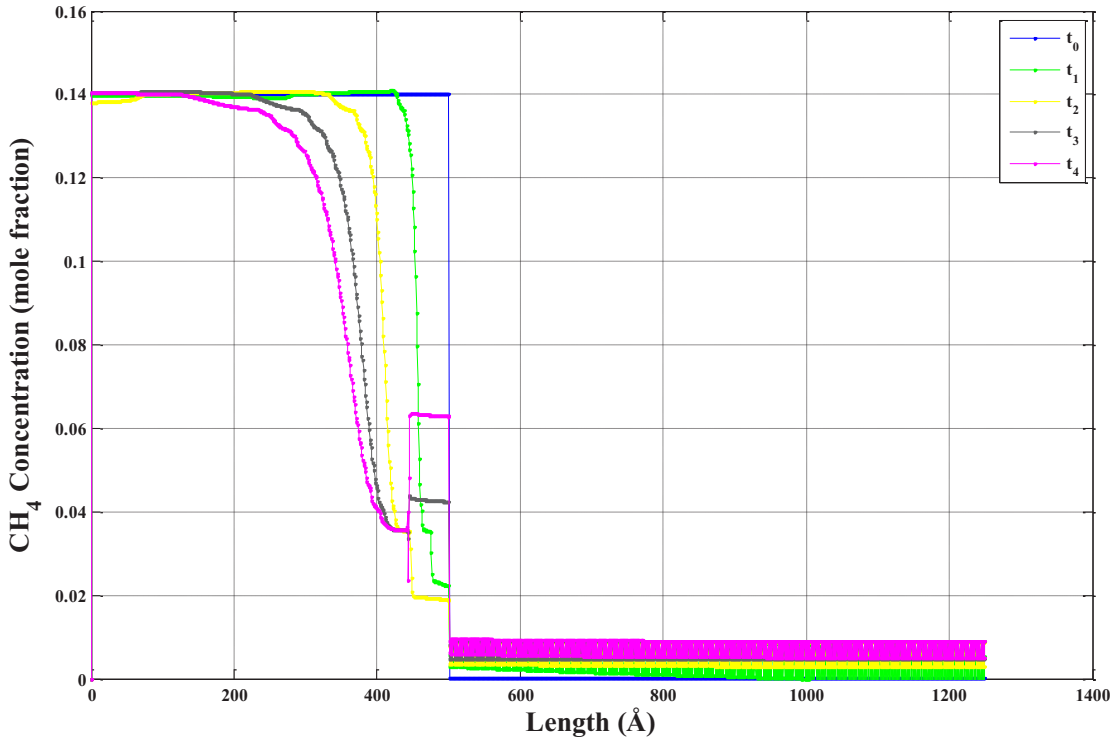

Figure 7-10: Methane concentration as a function of length inside the liquid 750Å away from the original interface. t_o, t_1, t_2 , t_3 and t_4 are different simulation times.

Figure 7-10 indicates concentration of methane in hydrate and liquid phases as a function of length. Rapid increase in concentration was observed inside the liquid phase. Higher methane concentration due to higher thermodynamic driving force from original hydrate phase to bulk liquid phase with increasing time was observed.

Similar procedure as in section 7.1 was used to determine the methane diffusion process from solid phase to liquid by tracking the φ values. In this case, the concentration of methane was traced from the liquid phase (0.0Å) to the hydrate center (1250Å) see Figure 6-3. Equations (7-1) and (7-2) were used to generate Figure 7-11.

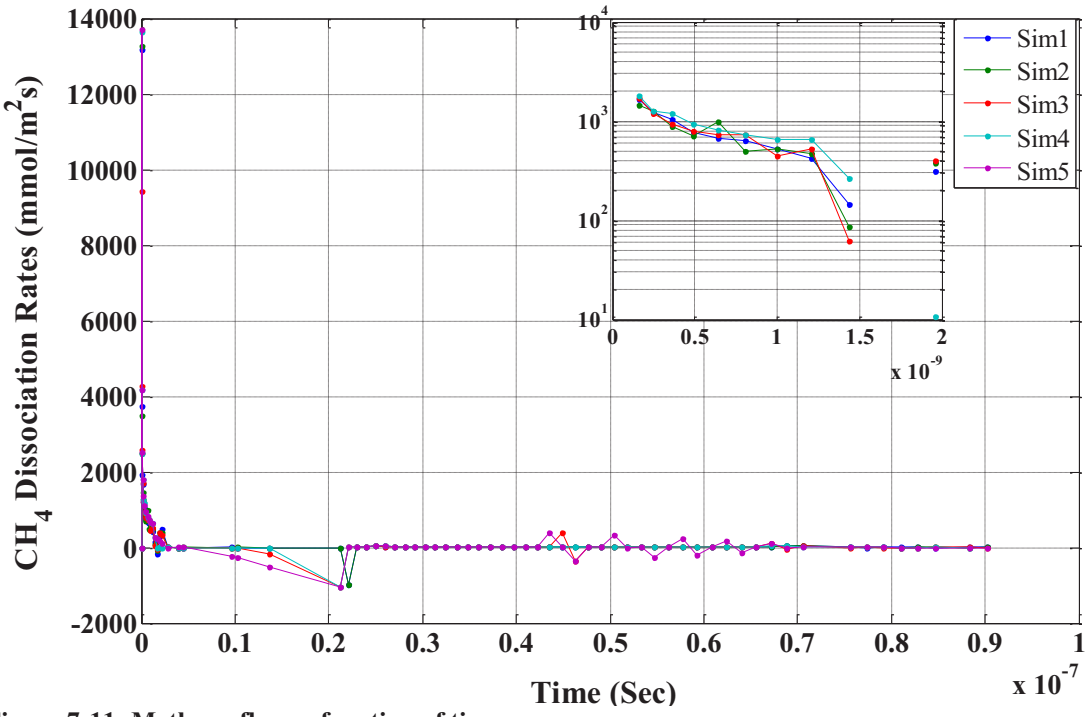

Figure 7-11: Methane flux as function of time.

Figure 7-11 shows methane fluxes as a function of time. The diffusion of methane from its hydrate to liquid CO_2 was observed opposite to section 7.1 and traces of methane from solid to liquid were done at times t_o, t_1, t_2 , t_3 and t_4 and 500, 480, 440, 420, and 410 Å respectively towards the liquid interface. Figure 7-11 on the left shows a high flux value due to initial relaxation of the system. The rate gradually decreased due to the thermodynamic driving force which is proportional to the chemical potential in the surrounding aqueous solution.

The CH_4 hydrate practically stopped dissociation when some CO_2 had already occupied the large cages which imply that the system was close to equilibrium between hydrate and aqueous solution, and the thermodynamic driving forces were practically reduced to zero. Negative flux values were observed during the CH4 – CO2 exchange process between the grid points as shown in Figure 7-6. The trapezoidal command in the attached cd was used to analyze the results. The released molecules of methane are shown in Table 7-2.

Table 7-2: Methane decomposed molecules from its hydrate

Simulation	Temperature (K)	Pressure (bars)	CH_4 hydrate density(kg/m^3)	Total CH_4 molecules decomposed from hydrate
1	274.15	100	448.6	2.9637e+006
2	276.92	102.94	451.8	3.1469e+006
3	278.99	105.89	456.3	3.1405e+006
4	282.79	111.28	464.0	3.1705e+006
5	284.17	113.24	466.6	3.1131e+006

Table 7-2 Indicate methane gas decomposed during the simulations.

7.4 Extrapolation for CH_4

Figure 7-12 shows an extrapolation of the dissociation rate of CH_4 from the different simulations conducted in this thesis. The figure shows the dissociation rate to follow the same trends of all the simulations. It was observed that after 10000 years the dissociation rates for simulation Sim3(c) and Sim5 (e) were 2.574E-28 and 2.423E-28 mmol/m^{2}s which corresponds to 8.117E-21 and 7.641E-21 mmol/m^{2}yr respectively. Although the simulation perfectly follows the power law $\alpha\ t^{1/2}$ showing the diffusion control process, the other simulations namely Sim1 (a), Sim2 (b) and Sim4 (d) were hardly seen due to very closer fluxes.

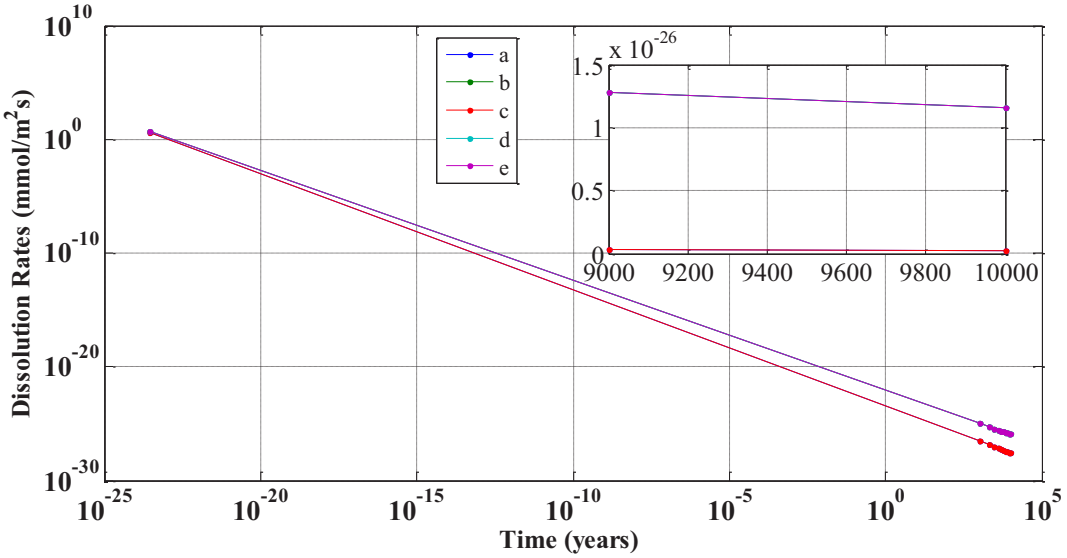

Figure 7-12: Extrapolation of reformation rate of CH_4 up to 10000 years

7.5 Relationship between methane and CO_2 concentrations

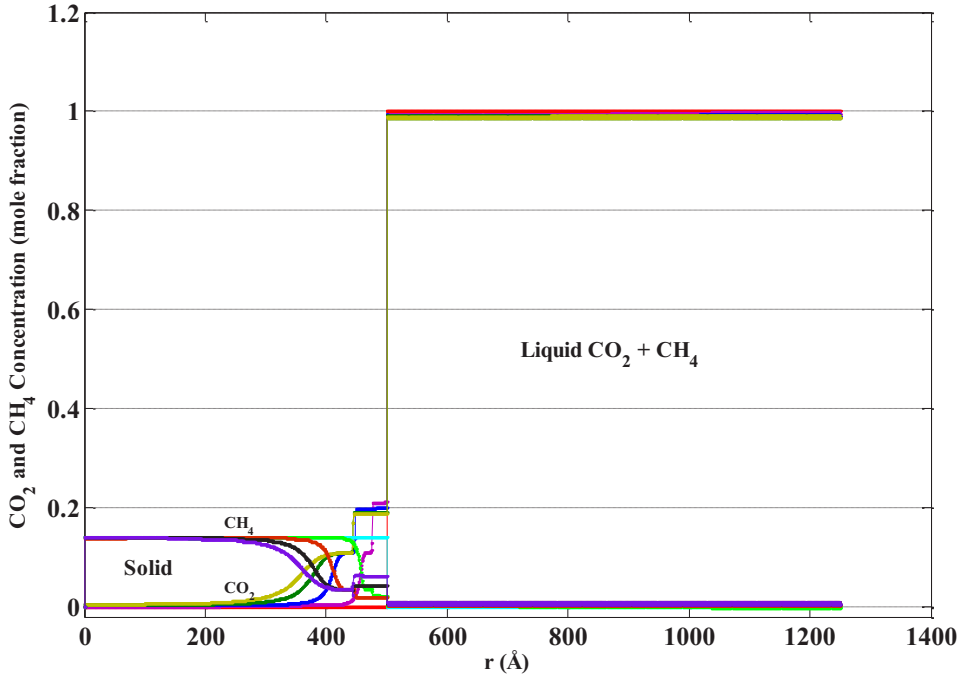

Figure 7-13: Solid and liquid phase of methane and CO_2

In Figure 7-13, both CH_4 and CO_2 were combined to show the different phases achieved during the exchange process. Observed was methane and CO_2 going in opposite directions which is related to CO_2 reforming its hydrate by refilling the large cavities of the methane hydrate.

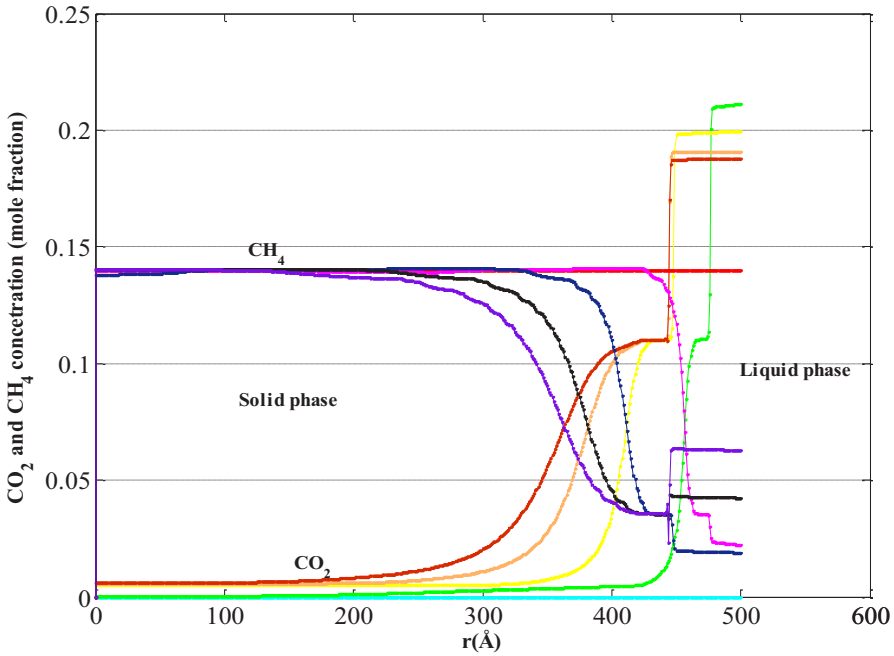

Figure 7-14: Time profile of methane and CO_2 mole fraction in the hydrate

Figure 7-14 shows the time profile of the mole fractions of CH_4 and CO_2 in the hydrate phase. The mole fraction of CH_4 decreased and that of CO_2 increased with time. It should be noted that the amount of the decomposed CH_4 hydrate is about 50% as that of the formed CO_2 hydrate over the periods covered in this study (Table 7-3). This close relation between the CH_4 hydrate decomposition and the CO_2 hydrate reformation implies that the guest molecule was replaced in the hydrate.

Table 7-3: Comparison of decomposed methane and CO_2 reformation

Sim no.	T (K)	P (bars)	CH_4 hydrate density (kg/m^3)	Total CH_4 molecules decomposed from hydrate	CO_2 hydrate density (kg/m^3)	Total CO_2 molecules accumulated into hydrate
1	274.15	100	448.6	2.9637e+006	873.9	1.6253e+006
2	276.92	102.94	451.8	3.1469e+006	861.8	1.6752e+006
3	278.99	105.89	456.3	3.1405e+006	854.5	1.6846e+006
4	282.79	111.28	464.0	3.1705e+006	841.3	1.6727e+006
5	284.17	113.24	466.6	3.1131e+006	836.8	1.6270e+006

Table 7-3 is used to compare the decomposed methane and the CO_2 reformation process.

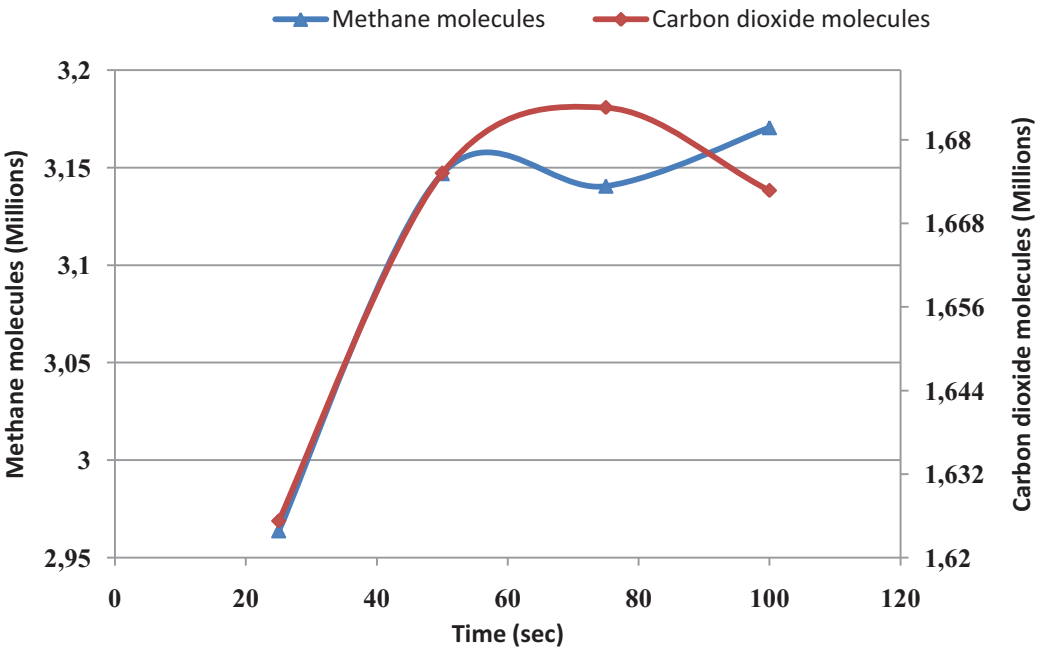

Figure 7-15: Illustration of methane and CO_2 in a trend form

Illustration of the exchange process between methane and CO_2 molecules is illustrated in Figure 7-15.

7.6 Summary

In this work the Phase Field Theory (PFT) was used as a basis for theoretical investigations of the mechanisms and kinetic rates for conversion of hydrate from methane hydrate over to CO_2 hydrate. New simulation data for the conversion of methane hydrate over to carbon dioxide hydrates have been presented. The main purpose of these simulations was to complement the experimental measurements but focus was changed over to investigations of conditions relevant to Nankai Through, which might be the first offshore hydrate field to be produced.

Results from this study showed relative contribution between CH_4-CO_2 exchanges. The comparison of methane dissociation and CO_2 reformation (Table 7-3) resulted in 50-55% of methane exchanged while CO_2 is stored as CO_2 hydrate over the periods of simulations covered in this study. The theoretical maximum of exchange is 75% CO_2 filling, corresponding to the 3/4 large cavities in structure I. It is therefore reasonable that CH_4 occupies the small cavities due to the extra stabilization. Although there are fairly large fluctuations at the end of the simulation, it implies CH_4 dissociation in the large cage, together with the CO_2 hydrate reformation, probably occurred at the early stage of the exchange reaction and needed more simulation time. However, it was assumed there is still some CH_4 remaining due to the CH_4 re-occupation of the small cage. When the CH_4 hydrate contacts the liquid CO_2, the cages of the CH_4 hydrate probably become unstable, and some CH_4 hydrate cages decompose. The CO_2 molecule that has transferred to the decomposition site can penetrate, leading to the guest molecule replacement in the hydrate (Figure 6-2). The CH_4 released from the large and small cages transfers into the liquid CO_2 phase at this moment. However, some portions of the released CH_4 are preferably captured in the small cage to keep the total hydrate structure stable because the CO_2 molecule is too large to occupy the small cage. This phenomenon could account for the CH_4 re-occupation in the small cage, to be caused by the hydrogen bonds (Takeya, Hori et al. 2000).

Based on the work of Park (Park, Choi et al. 2008) yielding high recoveries 65-95% when methane hydrate is exposed to N_2 in mixture with CO_2, a 50-55% recovery was observed in this work with only CO_2 injection alone. It is of course not possible to compare these simulations to the experimental data from a different injected gas mixture and different thermodynamic conditions. The approximated 50-55% hydrate reformation of CO_2 seems reasonable compared to the work of Park et.al (2008).

The simulations are very CPU intensive and simulation progress very slow. Within the time of the project it has not possible to run long enough. Longer simulation times might result in higher conversion, as also found experimentally in Section 5.3. It is also well known from experiments conducted here as well as similar experiments conducted by other groups that the initial conversion may be rapid while subsequent conversion slows down due to the establish CO_2 hydrate which reduces pathways for CO_2.

Although the amount of reported experimental data from measurements of CH_4 - CO_2 exchange in porous media has increased considerably, and the understanding of such systems have increased, a literature review reveals that there are some variations in opinions on the concept. Some of these variations are related to limited thermodynamic analysis, which requires a discussion of both enthalpy and free energy changes. Other variations are related to the fact that the systems are non-equilibrium systems and as such varying results may occur depending on differences in experimental set-ups. And no experimental system will be able to imitate natural hydrate systems which have been able to mature and rearrange for millions of years subject to different rates of fluid fluxes.

7.7 Conclusion

Thermodynamic properties (Kvamme and Tanaka 1995) and interface properties (Kvamme and Kuznetsova 2009) from molecular dynamic simulation samplings have been used in Phase Field Theory for studies of hydrate reformation. The sampled results give a detailed theoretical insight into the thermal decomposition of methane from its hydrate and the subsequent reformation of CO_2 hydrate. The kinetic data achieved are examples of important results which will be useful in the modeling and optimization for combined methane production and CO_2 sequestration. It was found that the mole fraction of CO_2 in the hydrate phase increased, while that of CH_4 decreased with increasing time.

7.8 Future perspectives

The current version of the implemented thermodynamics is limited to an upper pressure of 250 bars and a lower temperature of 273.15 K. The fundamental data derived by Kvamme and Tanaka (1995) do not have these boundaries and it should be fairly straightforward to extend

the thermodynamics of the PFT code to conditions of 180 K and practically unlimited pressures. The lower temperature limit is due to the impact of quantum mechanics for lower temperatures, which were not considered in the molecular simulations by Kvamme & Tanaka (1995).

An additional challenge arises from the fact that there are a number of various research areas that have to be considered when exposing methane hydrate for CO_2 sequestration in geological media:

Hydrodynamics**:** There is a need of hydrodynamics inclusion in the Phase Field code since hydrodynamics is the study of fluids in motions and also part of the picture when phase collide and merge. Practically this means that injected CO_2 at relevant conditions will be a liquid while released methane would have a density in the gas region. As such there is a competition between the rate at which methane forms bubbles and migrates due to gravity and the time needed for dissolution into CO2 phase. Furthermore - separate methane bubbles may merge when colliding. Some new work along these lines is in progress (Qasim, Baig et al. 2009).
However, factors affecting hydrodynamics are the fluid properties such as velocity, pressure, density, and temperature, as functions of space and time. Proper implementation of hydrodynamics should be able to account for dissociation with rapid agglomeration of released methane into bubbles as well as effects of merging bubbles through bubble collisions. Inclusion of hydrodynamics may make it possible to simulate systems up to microscale. This would also require the inclusion of some pore scale effects like the impact of mineral surfaces. These mineral surfaces can exhibit a double side effect. This could serve as sites for concentration of hydrate formers while at the same time lowering the chemical potential of water and as such have similar impact as a hydrate inhibitor. But since the effect of the solid surfaces is limited to 3 - 5 molecular diameters the net effect could be an enhancement of the hydrate formation kinetics close to mineral walls. And the formed hydrate will not be able to stick to the mineral surfaces as there will be a mismatch between the optimum hydrogen bonding on the hydrate surface and optimum interactions between the mineral surfaces and the surrounding water. See also (Kvamme, Kuznetsova et al. 2009) for a discussion of structure and thermodynamics of water at mineral surfaces as an example.

The effect of hydrodynamics is also expected to play a significant role in modeling a rising droplet surrounding by CO_2 hydrate, or the moving ocean water above a CH_4 or CO_2 reservoir. This is of course important for leaking hydrate reservoirs partly exposed to the seafloor and might also be important if there are leakage paths which can bring injected CO_2 to the seafloor.

Sloan et al (2008) calculated hydrate density by the use of equation (3-11) as shown in Appendix C- 6. A measured density by UniSim gives a relative hydrate density. Using these values, methane and CO_2 hydrate densities were calculated to achieve the results shown in Table 7-3. In accordance with hydrate density data, it was assumed the change in hydrate density error with increasing in pressure 100-200 bars should be considered. The error in determining the hydrate density by UniSim is quite acceptable without the use of equation (3-11) which is extremely difficult to determine for complex gas mixtures. Even at high pressures the error can does exceed a few percent comparable with, although slightly lower than; those calculated for both methane and CO_2 hydrate densities by Makogon and Sloan (Makogon 1981; Sloan and Koh 2008). This implies the effect of density should be included in the PFT code which may have resulted in some deviations in this work. This will also be needed in a hydrodynamic extension as also discussed in preliminary reporting on these extensions (Baig 2009).

Porosity could have a significant effect on hydrate simulation in sediments that host gas hydrates. On the basis of the results presented here, pore sizes could affect hydrate stability for any given pressure condition, which could be sufficient to shift the base of hydrate stability. . It is well known experimentally from different groups that nanoscale pores (below 5 nm in diameter) reduces the stability of hydrate. This is in accordance with the above discussion in the sense that mineral surfaces affect the chemical potential of adsorbed water. An additional effect is the mechanical constraint imposed on the hydrate lattice by being closed in between narrow walls. The interface thickness between hydrate and liquid water is in the order of 1 nm and might be larger between adsorbed water and hydrate due to the fairly fixed (limited motion) atoms of the mineral surfaces. And while the minimum thickness of structured liquid like water separating the hydrate from the mineral surfaces are on limited nanoscale reservoir flow and corresponding exchange of fluids might create substantial fluid channels due to dissociation of hydrates towards surrounding aqueous solution which is

undersaturated with respect to hydrate formers. Hydrate can even dissociate towards gas phase undersaturated with water. Individual hydrate reservoir will therefore vary very much depending on local fluids flows and possible hydrate phase transitions. It would therefore be desirable to do pore scale modeling using for instance Navier-Stokes for realistic pore structures. While these pore structures might be evaluated through CT scanning of core samples the information will not be complete enough to predict a unique mathematical model for the pore but nevertheless it can provide information which enable construction of some possible structures. Collaboration with department of geosciences at UoB on this would fruitful.

References

Anderson, F. E. and J. M. Prausnitz (1986). "Inhibition of Gas Hydrates by Methanol." Aiche Journal **32**(8): 1321-1333.

Archie, G. E. (1947). "Electrical Resistivity an Aid in Core-Analysis Interpretation." Aapg Bulletin-American Association of Petroleum Geologists **31**(2): 350-366.

Baig, K. (2009). "Phase Field Theory Modeling of CH4 and CO2 Fluxes from Exposed Natural Gas Hydrate Reserviors."

Ballard, A. L. and E. D. Sloan (2002). "The next generation of hydrate prediction I. Hydrate standard states and incorporation of spectroscopy." Fluid Phase Equilibria **194**: 371-383.

Cahn, J. W. and J. E. Hilliard (1958). "Free Energy of a Nonuniform System .1. Interfacial Free Energy." Journal of Chemical Physics **28**(2): 258-267.

Caldeira, K. and M. E. Wickett (2005). "Ocean model predictions of chemistry changes from carbon dioxide emissions to the atmosphere and ocean." J. Geophys. Res **110**: 12.

Chaplin, M. (2008). "*"Water structure and science"*." http://www.lsbu.ac.uk/water/index2.html.

Englezos, P., N. Kalogerakis, et al. (1987). "Kinetics of Gas Hydrate Formation from Mixtures of Methane and Ethane." Chemical Engineering Science **42**(11): 2659-2666.

Englezos, P. and Y. T. Ngan (1993). "Incipient Equilibrium Data for Propane Hydrate Formation in Aqueous-Solutions of Nacl, Kcl, and Cacl2." Journal of Chemical and Engineering Data **38**(2): 250-253.

Garcia, N. J. (June 30, 2008). "Coalbed Natural Gas Produced-Water Treatment Using Gas Hydrates."

Gibbs, J. W. (1870). Graphical methods in the thermodynamics of fluids. [New Haven,.

Goel, N. (2006). "*"In situ methane hydrate dissociation with carbon dioxide sequestration: Current knowledge and issues"*." Journal of Petroleum Science and Engineering, **51** (3-4): 169-184.(2006).

Gránásy, L., T. Pusztai, et al. (2003). "Phase field theory of crystal nucleation in hard sphere liquid." The Journal of Chemical Physics **119**: 10376.

Greiner, W., L. Neise, et al. (1995). Thermodynamics and statistical mechanics, Springer-Verlag New York Inc.

György Tegze, LászlóGránásy, et al. (2007). "“*Theoretical modeling of the conversion of methane hydrate into carbon dioxide hydrate*”, 2007, PCCP, **9**, 3104 - 3111
".

Hester, K. C. and P. G. Brewer (2009). "Clathrate Hydrates in Nature." Annual Review of Marine Science **1**: 303-327.

Jadhawar, P., A. H. Mohammadi, et al. (2006). "Subsurface carbon dioxide storage through clathrate hydrate formation." Advances in the Geological Storage of Carbon Dioxide: 111-126.

Jeffrey, G. A. (1984). "The Structures of Some Small Molecules - Abinitio Molecular-Orbital Calculations Versus Low-Temperature Neutron-Diffraction Crystal-Structure Analyses." Theochem-Journal of Molecular Structure **17**(1-2): 1-15.

Kurihara, H. (2008). "Effects of CO2-driven ocean acidification on the early developmental stages of invertebrates." Marine Ecology-Progress Series **373**: 275-284.

Kvamme, B. (2000). "*A Unified Nucleation Theory for the Kinetics of Hydrate Formation"*." Annals of the New York Academy of Sciences, **912** 496-501.(2000).

Kvamme, B. (*2002 b*). "*"Kinetics of Hydrate Formation from Nucleation Theory"*." International Journal of Offshore and Polar Engineering, **12** (4): 2002b).
Kvamme, B. (2002a). "*"Initiation and growth of hydrate"*." 4th International Conference on Natural Gas Hydrate, Yokohama, Japan, May 23-26, 2002a.
Kvamme, B. and T. Kuznetsova (2009). "Investigation into stability and interfacial properties of hydrate-aqueous fluid system." Mathematical and Computer Modelling.
Kvamme, B., T. Kuznetsova, et al. (2009). ""*Molecular dynamics studies of water deposition on hematite surfaces",* Proceedings from ICCMSE 2009, Rhodes, Greece, September 28th - October 4, 2009, 4 pages
".
Kvamme, B. and H. Tanaka (1995). "Thermodynamic stability of hydrates for ethane, ethylene, and carbon dioxide." Journal of Physical Chemistry **99**(18): 7114-7119.
Lee, H., Y. Seo, et al. (2003). "Recovering methane from solid methane hydrate with carbon dioxide." Angewandte Chemie-International Edition **42**(41): 5048-5051.
Lee, J. W., M. K. Chun, et al. (2002). "Phase equilibria and kinetic behavior of CO2 hydrate in electrolyte and porous media solutions: Application to ocean sequestration CO2." Korean Journal of Chemical Engineering **19**(4): 673-678.
Lien, J. R. (2004). "Basic reservoir physics (core analysis and logging)."
Long, J. P. (1994). "*"Gas Hydrate Formation Mechanism and Its Kinetic Inhibition"*." ColoradoSchool of Mines, PhD Thesis, 1994.
Long, J. P. S., E. D. (1996). "*Hydrates in the ocean and evidence for the location of hydrate formation*." International Journal of Thermophysics, **17** (1): 1-13.
Makogon, J. F. (1981). Hydrates of natural gas. Tulsa, Okla., PennWell.
Makogon, J. F. (1997). Hydrates of hydrocarbons. Tulsa, Okla., PennWell Books.
Odland, J. (2009). "Illustration of the core holder used in the resistivity measurement ".
Ohgaki, K., K. Takano, et al. (1994). "Exploitation of Ch4 Hydrates under the Nankai Trough in Combination with Co2 Storage." Kagaku Kogaku Ronbunshu **20**(1): 121-123.
Ohgaki, K., K. Takano, et al. (1996). "Methane exploitation by carbon dioxide from gas hydrates - Phase equilibria for CO2-CH4 mixed hydrate system." Journal of Chemical Engineering of Japan **29**(3): 478-483.
openlearn. "Earth's physical resources: petroleum." Retrieved 30/10/2009, from http://openlearn.open.ac.uk/mod/resource/view.php?id=172153.
Ota, M., K. Morohashi, et al. (2005). "Replacement of CH4 in the hydrate by use of liquid CO2." Energy Conversion and Management **46**(11-12): 1680-1691.
Park, Y., Y. N. Choi, et al. (2008). "Thermal expansivity of tetrahydrofuran clathrate hydrate with diatomic guest molecules." Journal of Physical Chemistry B **112**(23): 6897-6899.
Phale, H. A., T. Zhu, et al. (2006). "*Simulation study on injection of CO2-Microemulsion for Methane Recovery From Gas-Hydrate Reservoirs*." SPE Gas Technology Symposium, Calgary, Alberta, Canada, 2006.
Program, T. N. M. H. R. D. "All About Hydrates - Occurences of Natural Methane Hydrate."
Qasim, M., K. Baig, et al. (2009). ""*Phase Field Theory modeling of methane fluxes from exposed natural gas hydrate reservoirs ",* Proceedings from ICCMSE 2009, Rhodes, Greece, September 28th - October 4, 2009, 4 pages."
Saji, A., H. Yoshida, et al. (1992). "Fixation of Carbon-Dioxide by Clathrate-Hydrate." Energy Conversion and Management **33**(5-8): 643-649.
Saner, S., M. N. Cagatay, et al. (1997). "Electrical resistivity behavior of high salinity brine suspensions." Powder Technology **93**(3): 275-282.
Seol, Y., T. J. Kneafsey, et al. (2006). "Preliminary relative permeability estimates of methane hydrate-bearing sand." Lawrence Berkeley National Laboratory: Lawrence Berkeley

National Laboratory. Retrieved from: http://www. escholarship. org/uc/item/50b9n4c0.
Skovborg, P. and P. Rasmussen (1994). "A Mass-Transport Limited Model for the Growth of Methane and Ethane Gas Hydrates." Chemical Engineering Science **49**(8): 1131-1143.
Sloan, E. D. (1990). Clathrate hydrates of natural gases. New York, M. Dekker.
Sloan, E. D. (1998). Clathrate hydrates of natural gases. New York, Marcel Dekker.
Sloan, E. D. (2003). "Clathrate hydrate measurements: microscopic, mesoscopic, and macroscopic." Journal of Chemical Thermodynamics **35**(1): 41-53.
Sloan, E. D. (2005). "A changing hydrate paradigm - from apprehension to avoidance to risk management." Fluid Phase Equilibria **228**: 67-74.
Sloan, E. D. and C. A. Koh (2008). Clathrate hydrates of natural gases. Boca Raton, FL, CRC Press.
Sloan Jr, E. D. "Fundamental principles and applications of natural gas hydrates." Structure **5**(12): 6-8.
Svandal, A., B. Kvamme, et al. (2006). "The phase-field theory applied to CO2 and CH4 hydrate." Journal of Crystal Growth **287**(2): 486-490.
Takahashi, H., T. Yonezawa, et al. (2001). Exploration for Natural Hydrate in Nankai-Trough Wells Offshore Japan.
Takeya, S., A. Hori, et al. (2000). "Freezing-memory effect of water on nucleation of CO2 hydrate crystals." J. Phys. Chem. B **104**(17): 4164-4168.
Tatiana Kuznetsova , B. K., Kathryn Morrissey, (2009). "*An alternative for carbon dioxide emission mitigation: in situ methane hydrate conversion ",* Proceedings from ICCMSE 2009, Rhodes, Greece, September 28th - October 4, 2009, 4 pages
".
Taylor, C. J., K. T. Miller, et al. (2007). "*Macroscopic investigation of hydrate film growth at the hydrocarbon/water interface*."
Tohid, P. B. (2005). "Centre for Gas Hydrate Research Institute of Petroleum Engineering."
Vanderwaals, J. H. and J. C. Platteeuw (1959). "Clathrate Solutions." Advances in Chemical Physics **2**: 1-57.
www.beg.utexas.edu "http://www.beg.utexas.edu/indassoc/fraccity/public/graphics/sanddiagen.gif."
Yamasaki, A., H. Teng, et al. (2000). "CO2 hydrate formation in various hydrodynamic conditions." Gas Hydrates: Challenges for the Future **912**: 235-245.
Yongjun, L., Z. Weidong, et al. (2008). "*Experimental Characterisation and Modelling of Acoustic Velocity and Electrical Resistance in Hydrate Bearing Sediments* Paper presentert på 6th International Conference on Gas Hydrates.".
Yoon, J. H., T. Kawamura, et al. (2004). "Transformation of methane hydrate to carbon dioxide hydrate: In situ Raman spectroscopic observations." Journal of Physical Chemistry A **108**(23): 5057-5059.

Appendix A: Experimental I

Appendix A- 1 Measured and calculated core sample parameters for experiment I

	Core 1	Core 2	Core 3
Core parameters	**1 wt % NaCl**	**3 wt % NaCl**	**5 wt % NaCl**
Pressure (psig)	1200	1200	1200
Temperature (^{o}C)	3	3	3
Weight (g)	532.58	530.46	527.67
Diameter(m)	0.0508	0.0507	0.0508
Length (m)	0.1275	0.1273	0.1271
Porosity (%)	0.222	0.221	0.227
Bulk volume	258.42	257.0	257.61
Grain volume	200.97	200.17	199.12
Pore volume	57.45	56.13	58.49
Water saturation	0.578	0.487	0.499
Area of the core (m^2)	0.00203	0.00204	0.00204
Core volume (m^3)	$2.58*10^{-4}$	$2.57*10^{-4}$	$2.58*10^{-4}$

Appendix A- 2: Resistivity calculations

Resistivity measurement with 1wt% NaCl

Acc. Time (s)	Time (hrs)	Temperature (oC)	Resistivity (ohm*m)
0	0,000	11	40,84
300	0,083	11	40,52
360	0,100	11	40,36
420	0,117	11	40,12
600	0,167	11	39,80
720	0,200	11	39,40
1200	0,333	10	39,32
1500	0,417	9,7	39,32
2100	0,583	9,5	39,24
2400	0,667	8	39,40
2520	0,700	7,8	39,56
2700	0,750	4,6	39,88
3600	1,000	4,4	40,12
4500	1,250	4,3	40,12
6300	1,750	4,2	40,20
12900	3,583	4,1	40,44
16140	4,483	4,1	40,52
64140	17,817	4,1	41,24
72300	20,083	4,1	41,40
77100	21,417	4,1	41,48
78000	21,667	4,1	41,56
85200	23,667	4,1	41,72

Resistivity measurement with 3wt% NaCl

Time (hrs)	Temperature(oC)	Resistivity (ohm*m)	Time (hrs)	Temperature (oC)	Resistivity (ohm*m)
0,000	24,6	38,8	1,092	3,8	37,8
0,083	24,5	38,7	1,125	3,7	37,8
0,092	24,4	38,0	1,308	3,4	37,9
0,100	24,2	37,9	1,375	3,3	37,9
0,108	23,8	38,1	1,425	3,2	38
0,117	23,5	38,0	1,575	3,1	38
0,133	22,3	38,2	1,658	3	38
0,167	19,8	37,9	1,708	3	38,1
0,200	18,3	37,9	2,458	2,9	38,2
0,217	17,5	37,9	2,658	2,9	38,5
0,253	14,7	37,7	3,142	2,9	38,5
0,411	9,7	37,5	3,292	2,9	38,5
0,461	8,7	37,4	3,825	2,9	38,5
0,544	7,2	37,4	3,958	3,2	38,5
0,561	6,9	37,3	4,358	2,9	38,6
0,611	6,4	36,9	4,458	2,9	38,7
0,636	6,3	37	4,558	3	38,8
0,669	6,1	36,8	4,658	2,9	38,8
0,694	5,9	37,1	4,725	3	38,7
0,728	5,6	36,8	4,792	2,9	38,8
0,778	5,2	36,9	5,008	2,9	38,9

0,828	5	36,6	5,075	2,9	39
0,853	4,8	36,6	5,192	2,9	39
0,878	4,7	36,6	5,342	2,9	39
0,894	4,6	36,9	5,442	2,9	39
0,911	4,5	37,1	5,625	2,9	39
0,919	4,5	37,2	5,942	2,9	39
0,928	4,5	37,3	6,158	2,9	39
0,931	4,4	37,4	6,308	2,9	39,1
0,936	4,4	37,5	6,342	2,9	39,2
0,938	4,4	37,6	6,842	2,9	39,2
0,944	4,4	37,7	7,342	2,9	39,3
0,961	4,3	37,8	25,942	2,8	39,3
0,975	4,2	37,8	29,075	2,9	42,1
1,000	4,1	37,8	47,408	2,9	42,8
1,025	4	37,8	49,275	2,9	42,8
1,042	4	37,8	52,302	3	42,8
1,075	3,9	37,8	72,736	2,9	43,2

Resistivity measurement with 5wt% NaCl

Time (hrs)	Temperature (oC)	Resistivity (ohm*m)	Time (hrs)	Temperature(oC)	Resistivity (ohm*m)
0,000	23,1	42,2	0,770	5,10	41,10
0,050	21,7	42,2	0,780	4,90	41,00
0,117	18,6	42,0	0,820	4,90	41,00
0,150	16,7	41,9	0,830	4,70	40,90
0,167	15,8	41,9	0,850	4,60	40,90
0,183	15,4	41,8	0,870	4,40	40,90
0,200	14,7	41,8	0,880	4,40	40,90
0,220	14	41,8	0,900	4,30	40,80
0,230	13,5	41,8	0,920	4,10	40,70
0,250	12,6	41,7	0,930	4,00	40,40
0,270	12,3	41,7	0,950	4,00	39,30
0,280	12,1	41,7	0,970	3,90	39,20
0,300	11,7	41,7	0,980	3,90	38,70
0,320	11,4	41,6	1,000	3,90	38,30
0,330	10,4	41,6	1,020	3,80	37,90
0,350	10,8	41,6	1,030	3,80	37,80
0,370	10,5	41,6	1,070	3,80	37,60
0,380	9,9	41,5	1,080	3,70	37,50
0,400	9,5	41,4	1,100	3,70	37,50
0,420	9,1	41,4	1,120	3,70	37,40
0,433	8,8	41,4	1,130	3,60	37,30
0,450	8,6	41,3	1,150	3,60	37,20
0,460	8,3	41,3	1,170	3,60	37,20
0,480	7,9	41,3	1,180	3,50	37,10
0,500	7,6	41,3	1,200	3,50	37,10
0,520	7,4	41,3	1,220	3,50	37,00
0,530	7,1	41,3	1,230	3,50	37,00
0,550	6,9	41,3	1,270	3,50	36,90
0,570	6,7	41,3	1,280	3,50	36,90
0,580	6,6	41,3	1,300	3,40	37,00
0,600	6,2	41,2	1,320	3,40	37,00
0,650	6,1	41,2	1,330	3,40	37,00
0,670	6	41,2	1,370	3,40	37,10

0,680	5,8	41,2	1,380	3,40	37,10
0,700	5,6	41,2	1,400	3,40	37,10
0,720	5,5	41,1	1,420	3,40	37,20
0,730	5,4	41,1	1,430	3,30	37,20
0,750	5,3	41,1	1,467	3,30	37,20
			1,483	3,30	37,20
			1,500	3,30	37,20
			1,530	3,30	37,20
			1,550	3,30	37,20
			1,580	3,30	37,20
			1,600	3,30	37,20
			1,630	3,30	37,20
			1,667	3,30	37,20
			1,700	3,30	37,20
			1,720	3,30	37,20
			1,730	3,30	37,20
			1,750	3,10	37,20
			1,770	3,10	37,20
			1,800	3,10	37,20
			1,850	3,10	37,20
			1,950	3,10	37,20
			2,020	3,10	37,20
			2,170	3,10	37,30
			2,330	3,10	37,30
			2,400	3,10	37,30
			2,600	3,20	37,30
			2,820	3,10	37,30
			3,120	3,10	37,40
			3,230	3,10	37,40
			3,350	3,10	37,40
			3,430	3,10	37,50
			3,480	3,10	37,50
			3,520	3,10	37,50

Appendix B: Experimental II

Appendix B- 1: Measured and calculated core sample parameters for experiment II

Core parameters	5 wt % NaCl
Core weight (g)	420.70
Core length (m)	0.0981
Core diameter (m)	0.0516
Grain density (g/cm^3)	2.65
Pressure (psig)	1200
Temperature (^{o}C)	20
Volume of methane injected during hydrate formation (mL)	26.52
Bulk volume V_b (mL)	205.14
Volume of matrix/grain volume V_m (mL)	158.75
Pore volume V_p (mL)	46.39
Porosity	0.226
Volume of imbibed water V_w (mL)	16.52
Water saturation S_w	0.356
Volume of expansion (mL)	1.26
Residual volume $Vp_{residual}$ (mL)	25.57

Methane parameters		
Methane molar weight (g/mol)	16.04	
Temperature (^{o}C)	Pressure (psig)	Density (g/mL)
4	1200	0.0718
20	1200	0.0648

Carbon dioxide parameters		
CO_2 molar weight (g/mol)	44.01	
Temperature (^{o}C)	Pressure (psig)	Density (g/mL)
4	1200	0.0955
20	1200	0.0827

Appendix B- 2: Ratio of CH4 and CO2 found from the gas chromatograph

Flush 1

No.	Peakname	Ret.Time	Area	Amount	Type	Height	Rel.Area
Test 1		min	mV*min			mV	%
	CH4	3,268	19,5906	12,8492	BMb*	312,019	30,54
	CO2	4,29	32,0079	4,811	BMB*	210,285	49,9
Ratio				2,670796092			
Test 2							
	CH4	3,279	20,5887	13,5038	BM*	327,422	36,1
	CO2	4,299	33,5135	5,0372	M*	216,043	58,77
Ratio				2,680814738			
Test 3							
	CH4	3,278	18,6496	12,232	BM*	295,168	37,3
	CO2	4,301	29,9011	4,4943	M*	199,091	59,8
Ratio				2,72166967			
Average ratio			(CH4/CO2)	2,6910935			

Flush 2

No.	Peakname	Ret.Time	Area	Amount	Type	Height	Rel.Area
Test 1		min	mV*min			mV	%
	CH4	3,296	4,5336	2,9735	Ru	77,562	3,71
	CO2	4,214	111,6353	16,7794	Mb*	436,667	91,3
Ratio				0,177211342			
Test 2							
	CH4	3,308	4,6437	3,0457	BMb	79,237	3,53
	CO2	4,222	114,7899	17,2535	bM*	436,748	87,34
Ratio				0,176526502			
Test 3							
	CH4	3,297	4,8033	3,1504	BMb	81,185	3,89
	CO2	4,208	117,0001	17,5857	bM*	436,136	94,8
Ratio				0,179145556			
Average ratio			(CH4/CO2)	0,1776278			

Flush 3

No.	Peakname	Ret.Time	Area	Amount	Type	Height	Rel.Area
Test 1		min	mV*min	mV		mV	%
	CH4	3,305	2,8075	1,8414	MB	48,628	2,47
	CO2	4,214	109,4661	16,4533	BMB	422,025	96,26
Ratio							
Test 2				0,111916758			
	CH4	3,305	2,593	1,7007	BMB	43,48	2,22
	CO2	4,223	112,5404	16,9154	BMB	442,769	96,47
Ratio				0,100541518			
Test 3							
	CH4	3,291	2,2725	1,4905	BM	37,837	2,02
	CO2	4,223	99,0645	14,8899	BM	408,293	88,21
Ratio				0,100101411			
Average ratio			(CH4/CO2)	0,104186563			

Flush 4	Channel	# Records			
Area Percent	TCD-channel B		27	CH4	CO2
Date	Time	Sample id		0,606	98,805
06.02.2009	09:56:03	4th_flush_sample4_001		0,038	99,526
06.02.2009	09:58:37	4th_flush_sample4_001		0,028	99,445
06.02.2009	10:01:14	4th_flush_sample4_001		0,025	99,211
06.02.2009	10:03:51	4th_flush_sample4_001		0,032	99,263
06.02.2009	10:06:28	4th_flush_sample4_001		0,035	99,508
06.02.2009	10:09:05	4th_flush_sample4_001		0,662	98,813
06.02.2009	10:28:08	4th_flush_sample4_002		0,035	99,53
				1,461	794,101
Average ratio				(CH4/CO2)	0,001839816

Appendix B- 3: GC-parameters

GC-analysis					
GC #		**1**	**2**	**3**	**4**
Run		**1**	**1**	**1**	**1**
Description		1^{st} CO_2 flush	2^{nd} CO_2 flush	3^{rd} CO_2 flush	4^{th} CO_2 flush
Sample pressure (psig)		1200	1200	1200	1200
Sample Temperature (^oC)		20	20	20	20
Sample volume drawn (mL)		60	60	60	60
Mixture density (g/mL)	UniSim	0.103	0.396	0.591	0.811
Mixture weight (g)		6.18	23.76	35.46	48.66
Mole fractions in mixture	GC analysis	2.6911	0.1776	0.1042	0.00184
Moles in sample		0.0709	0.2725	0.4067	0.5582
Moles of CO_2		0.0192	0.2314	0.3684	0.5571

Appendix C: Simulation

Appendix C- 1: Pressure and Temperature calculation from equations (6-1).

Sr#	P_o (bar)	P_o (Pa)	Z (m)	Z_o (m)	P (Pa)	P (bar)
1	100	100 000	0	0	100000	100,00
2	100	10 000 000	5	0	10049050	100,49
3	100	10 000 000	10	0	10098100	100,98
4	100	10 000 000	15	0	10147150	101,47
5	100	10 000 000	20	0	10196200	101,96
6	100	10 000 000	25	0	10245250	102,45
7	100	10 000 000	30	0	10294300	102,94
8	100	10 000 000	35	0	10343350	103,43
9	100	10 000 000	40	0	10392400	103,92
10	100	10 000 000	45	0	10441450	104,41
11	100	10 000 000	50	0	10490500	104,91
12	100	10 000 000	55	0	10539550	105,40
13	100	10 000 000	60	0	10588600	105,89
14	100	10 000 000	65	0	10637650	106,38
15	100	10 000 000	70	0	10686700	106,87
16	100	10 000 000	75	0	10735750	107,36
17	100	10 000 000	80	0	10784800	107,85
18	100	10 000 000	85	0	10833850	108,34
19	100	10 000 000	90	0	10882900	108,83
20	100	10 000 000	95	0	10931950	109,32
21	100	10 000 000	100	0	10981000	109,81
22	100	10 000 000	105	0	11030050	110,30
23	100	10 000 000	110	0	11079100	110,79
24	100	10 000 000	115	0	11128150	111,28
25	100	10 000 000	120	0	11177200	111,77
26	100	10 000 000	125	0	11226250	112,26
27	100	10 000 000	130	0	11275300	112,75
28	100	10 000 000	135	0	11324350	113,24
29	100	10 000 000	140	0	11373400	113,73
30	100	10 000 000	145	0	11422450	114,22
31	100	10 000 000	150	0	11471500	114,72

Appendix C- 2: Dissociation pressures and temperatures for methane and CO_2

Simulation number	Methane		CO_2
	T (K)	P (bar)	P (bar)
1	274.15	28.95	14.14
2	276.92	37.65	19.30
3	278.99	45.95	24.62
4	282.79	66.99	40.64
5	284.17	77.18	84.12

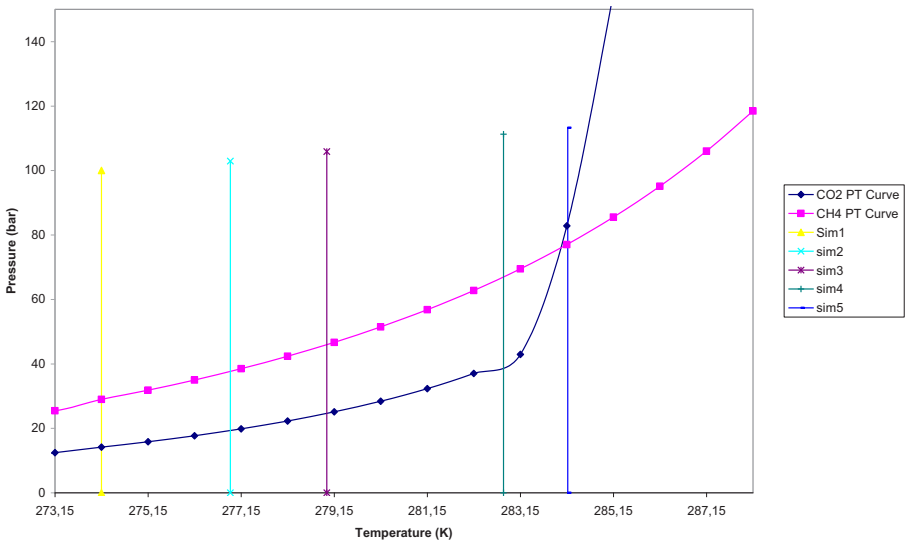

Appendix C- 3: Dissociation pressures and simulation zones CSMHYD (Sloan 1998).

Appendix C- 4: Constants A and B for CH_4 and CO_2 cavities (Makogon 1981)

Constants A and B (structure 1)				
Small cavities			**Large cavities**	
Component	As	Bs	AL	BL
methane	6.9153	0.03155	6.0966	0.02792
CO_2	14.9976	0.05884	15.2076	0.0586

Appendix C- 5: Langmuir constant and density calculation for sI hydrates

			Langmuir Constant								
Temperature	**Eq.Pressure**	**Eq.Pressure**	**A1**	**B1**	**A2**	**B2**	**A2**	**B2**	**CS**	**CL**	**CL**
(K)	**CH4 (bar)**	**CO2 (bar)**	**CH4S**	**CH4S**	**CH4L**	**CH4L**	**CO2L**	**CO2L**	**CH4**	**CH4**	**CO2**
274,15	28,95	14,14	6,92	0,03	6,10	0,03	15,21	0,06	0,47	0,51	0,67
276,92	37,65	19,3	6,92	0,03	6,10	0,03	15,21	0,06	0,45	0,49	0,62
278,99	45,95	24,62	6,92	0,03	6,10	0,03	15,21	0,06	0,44	0,48	0,59
282,79	66,99	40,64	6,92	0,03	6,10	0,03	15,21	0,06	0,42	0,46	0,54
284,17	77,18	84,12	6,92	0,03	6,10	0,03	15,21	0,06	0,41	0,45	0,52

			Density Calculation for sI Hydrates							
Temperature	**Eq.Pressure**	**Eq.pressure**	**θS**	**θL**	**θL**	**ρCH4**		**Pure CO2**	**HN**	**HN**
(K)	**CH4 (bar)**	**CO2 (bar)**	**CH4**	**CH4**	**CO2**	**Kg/m^3**		**Kg/m^3**	**CH4**	**CO2**
274,15	28,95	14,14	0,932	0,936	0,904	910,7		1 025,11	6,148	8,478

276,92	37,65	19,3	0,945	0,949	0,923	912,3	1 029,90	6,067	8,305
278,99	45,95	24,62	0,953	0,957	0,936	913,2	1 033,06	6,017	8,194
282,79	66,99	40,64	0,966	0,968	0,956	914,7	1 038,25	5,942	8,019
284,17	77,18	84,12	0,969	0,972	0,978	915,2	1 043,69	5,919	7,843

Appendix C- 6: Change in concentration and size of hydrate, where Δx is the change in hydrate size (diameter), Δy change in concentration in hydrate, φ = 1 and 0 for liquid and methane hydrate respectively.

Time (ns)	*φ*	*Δx (Å)*	*Δy(mole fraction)*
0.0000	1	1001	0
	0	999	0
6.250	1	999	0
	0	884	0.0138
25.00	1	1001	0.004
	0	689	0.0068
81.00	1	1001	0.0031
	0	568	0.00487
100	1	1001	0.0033
	0	599	0.01684